Turun yliopisto
University of Turku

TOWARDS IMPROVED CHARACTERIZATION OF PROSTATE CANCER USING MAGNETIC RESONANCE IMAGING AND POSITRON EMISSION TOMOGRAPHY

Ivan Jambor

TURUN YLIOPISTON JULKAISUJA – ANNALES UNIVERSITATIS TURKUENSIS
Sarja - ser. D osa - tom. 1296 | Medica - Odontologica | Turku 2017

University of Turku

Faculty of Medicine
Department of Radiology
University of Turku Doctoral Program of Clinical Investigation (CLIDP)
Turku PET Centre
Turku, Finland

Supervised by

Professor Hannu J Aronen, MD, PhD
Department of Diagnostic Radiology
University of Turku
Turku, Finland

Professor Heikki Minn, MD, PhD
Department of Oncology and Radiotherapy
Turku University Hospital
Turku, Finland

Reviewed by

Matthew Davenport, MD
Department of Radiology
University of Michigan,
Ann Arbor, MI, USA

Uulke van der Heide, PhD
Department of Radiotherapy,
The Netherlands Cancer Institute
Antoni van Leeuwenhoek Hospital,
Amsterdam, The Netherlands

Opponent

Amita Shukla Dave, PhD
Department of Medical Physics
Memorial Sloan Kettering Cancer Center,
New York, USA.

The originality of this thesis has been checked in accordance with the University of Turku quality assurance system using the Turnitin OriginalityCheck service.

ISBN 978-951-29-6909-8 (PRINT)
ISBN 978-951-29-6891-6 (PDF)
ISSN 0355-9483 (Print)
ISSN 2343-3213 (Online)
Painosalama Oy - Turku, Finland 2017

To my family

Ivan Jambor
MRI and PET for detection and characterization of prostate cancer

University of Turku, Faculty of Medicine, Department of Radiology, University of Turku Doctoral Programme of Clinical Investigation (CLIDP), Turku PET Centre, Turku, Finland
Annales Universitatis Turkuensis, Turku, Finland 2017

ABSTRACT

Approximately every seventh man will be diagnosed with prostate cancer during his lifetime. Prostate cancer has a wide range of aggressiveness ranging from indolent to lethal disease. Accurate characterization of prostate cancer is of utmost importance to prevent overtreatment while maintaining long survivorship and quality of life.

In this thesis work, the role of two novel positron emission tomography tracers in the detection and characterization of the prostate was evaluated. ^{68}Ga-labeled bombesin antagonist (BAY86-7548) was shown to have a high prostate-binding specificity and significantly higher uptake in prostate cancer compared to benign prostatic hyperplasia and normal prostate tissue. Although anti-1-amino-3-18F-fluorocyclobutane-1-carboxylic acid (^{18}F-FACBC) uptake was significantly higher in tumors with a higher Gleason score, our results indicate that ^{18}F-FACBC positron emission tomography brings limited added value to multiparametric magnetic resonance imaging (MRI).

Various mathematical models and/or functions for diffusion-weighted imaging (DWI) were extensively evaluated using simulations and repeated MRI examinations. The Kurtosis model demonstrated higher information content (fitting quality), similar repeatability, and similar robustness against noise than the most commonly used mono-exponential model.

Spin-lock imaging methods were compared with DWI and evaluated in terms of prostate cancer detection and characterization. The novel spin locking methods such as relaxation along factious field (RAFF) provided added value to DWI and in some instance outperform DWI.

Finally, we have developed and validated a rapid pre-biopsy MRI protocol which substantially improves the selection of men for biopsy and limits unnecessary biopsy procedures. The use of anatomical T2-weighted imaging and DWI was shown to be accurate and sufficient for initial decision management and targeted biopsy in patients with a clinical suspicion of prostate cancer.

The findings of this thesis work have the potential to improve prostate cancer risk stratification and may ultimately improve quality of life and survival.

Keywords: magnetic resonance imaging, positron emission tomography, multiparametric MRI, diffusion weighted imaging

Turun Yliopisto
Annales Universitatis Turkuensis, Turku, Finland 2017

TIIVISTELMÄ

Keskimäärin joka seitsemännellä miehellä todetaan elämän aikana eturauhassyöpä. Eturauhassyövän aggressiivisuus vaihtelee laajalti kivuttomasta tappavaan. Eturauhassyövän karakterisointi on hyvin tärkeää, jotta voidaan välttää ylihoitamista samalla säilyttäen hyvä selviytymistodennäköisyys ja elämänlaatu.

Tässä väitöskirjassa arvioitiin kahden uuden radiolääkeaineen roolia eturauhassyövän havaitsemisessa ja luokittelussa eturauhasen robottileikkaukseen lähetetyillä miehillä positroniemissiotomografialla. ^{68}Ga-leimatun bombesiini-vastavaikuttajan (BAY86-7548) spesifinen sitoutuminen eturauhassyöpään osoitettiin korkeaksi. Lisäksi ^{68}Ga-BAY86-7548:n kertyminen eturauhassyöpään oli merkittävästi korkeampaa kuin hyvänlaatuiseen liikakasvuun tai normaaliin eturauhaskudokseen. Vaikka toisen positronisäteilevän merkkiaineen anti-1-amino-3-18F-fluorosyklobutaani-1-karboksyylihapon (^{18}F-FACBC) kertyminen oli merkittävästi suurempaa korkean Gleason-luokan syövässä, tulokset osoittavat että ^{18}F-FACBC -tutkimus toi vain rajoitetusti lisäarvoa moniparametriseen magneettikuvantamiseen verrattuna.

Väitöskirjassa arvioitiin lisäksi laajalti diffuusiopainotetun kuvantamisen matemaattisia malleja käyttäen simulaatioita ja toistettuja magneettitutkimuksia.

Diffuusiopainotteisin magneettikuvauksen matemaattisia malleja arvioitiin käyttäen simulaatioita ja toistettuja magneettitutkimuksia. Diffuusion kurtoosimallin avulla oli mahdollista saada enemmän hyödyllistä informatiota eturauhassyövän diagnostiikassa kuin yleisimmin käytettyn monoeksponentiaalisen mallin avulla. Spinin lukitus -kuvausmenetelmiä verrattiin diffuusiopainoteiseen kuvantamiseen eturauhassyövän havaitsemissa- ja luokittelussa. Lopuksi kehitimme ja tutkimme ennen biopsiaa tehtävän nopean magneettikuvausprotokollan tarkkuutta eturauhassyövän diagnostiikassa. Menetelmän avulla voidaan valiota paremmin biopsiasta hyötyvät miehet ja vähentää tarpeettomia toimenpiteitä. Anatomisten T2-painotettujen ja diffuusiopainotettujen kuvien yhteiskäytön osoitettiin olevan riittävän tarkkaa alustavalle päätöksenteolle ja kohdistamaan biopsia potilaille, joilla on kliinisesti merkittävän eturauhassyövän oireenkuva.

Tämän väitöskirjan löydösten avulla on mahdollista parantaa eturauhassyövän riskin arviointia ja tutkimuksen tulosten perusteella voidaan parantaa potilaiden elämänlaatua ja selviytymistä.

Avainsanat: magneettikuvaus, positroniemissiotomografia, moniparametrinen MRI, diffuusiopainotetteinen magneettikuvantaminen

TABLE OF CONTENTS

ABBREVIATIONS

^{1}H-MRS	Proton magnetic resonance spectroscopy
ADC	Apparent diffusion coefficient
AIF	Arterial input function
AUC	Area under the curve
BPH	Benign prostatic hyperplasia
bpMRI	Biparametric prostate MRI
CT	Computed tomography
CZ	Central zone of the prostate gland
C_p	Median concentration in plasma
DCE-MRI	Dynamic contrast enhanced MRI
dPSA	PSA density
DTI	Diffusion tensor imaging
DRE	Digital rectal examination
DWI	Diffusion weighted imaging
ERC	Endorectal coil
FDA	US Food and Drug Administration
ERSPC	European Randomised Study of Screening for Prostate Cancer Trial
fPSA	free PSA
GLUT	Glucose transporter expression
Gd	Gadolinium
GRAPPA	Generalized autocalibrating partially parallel acquisitions
HGPIN	High-grade prostatic intraepithelial neoplasia
IVIM	Intravoxel incoherent motion
K^{trans}	Transfer constant (blood vessel permeability)
k_{ep}	Rate constant
MRI	Magnetic resonance imaging
mpMRI	Multiparametric magnetic resonance imaging
M_0	Net magnetization
NCCN	National Comprehensive Cancer Network
NSA	Number of signal averages

OR	Odds ratio
PET	Positron emission tomography
PCa	Prostate cancer
PCPTRC	Prostate Cancer Prevention Trial Risk Calculator 2.0
PCPT	Prostate Cancer Prevention Trial
RF	Radio frequency
PIN	Prostatic intraepithelial neoplasia
ppm	parts per million
PRESS	Point resolved spectroscopy sequence
PLCO	Prostate, Lung, Colorectal, and Ovarian Cancer Screening Trial
PSA	Prostate specific antigen
PZ	Peripheral zone of the prostate gland
se-Ssh EPI	Spin-echo single-shot echo planar imaging
SNR	Signal to noise
SENSE	SENSitivity Encoding
SPACE	3D TSE sequence with variable flip angle
SPAIR	SPectral Attenuated Inversion Recovery
T	Tesla
T2w	T2-weighted imaging
TE	Echo time
TPM biopsy	Template prostate mapping biopsy
TR	Repetition time
TRUS	Transrectal ultrasound
TSE	Turbo spin echo sequence
TZ	Transition zone of the prostate gland
VOI	Volume of interest
v_e	Fractional volumes of the extravascular extracellular space (0-100%)
v_p	Fractional volumes of plasma in tissue (0-100%)

LIST OF ORIGINAL PUBLICATIONS

This thesis is based on the following original publications, referred to in the text by the Roman numerals I-VII.

I Kähkönen E*, **Jambor I***, Kemppainen J, Lehtiö K, Silén J, Kuisma J, Luoto P, Tolvanen T, Alanen K, Grönroos T, Kallajoki M, Roivainen A, Schäfer N, Schibli R, Dragic M, Johayem M, Valencia R, Borkowski S, Minn H: In vivo imaging of prostate cancer using [^{68}Ga]-labeled bombesin analog BAY86-7548. *Clin Cancer Res*. 2013 Oct;19(19):5434–43 * Equal contribution

II **Jambor I**, Kähkönen E, Taimen P, Saunavaara J, Merisaari H, Alanen K, Ositnik B, Minn H, Lehotska V, Aronen HJ: Prebiopsy multiparametric 3T prostate MRI in patients with elevated PSA, normal digital rectal examination, and no previous biopsy. *J Magn Reson Imaging*. 2015 May;41(5):1394–404.

III **Jambor I**, Merisaari H, Taimen P, Boström P, Minn H, Pesola M, Aronen HJ: Evaluation of different mathematical models for diffusion weighted MR imaging of normal prostate and prostate cancer using high b-values: a repeatability study. *Magn Reson Med.* 2015 May;73(5):1988–98**.**

IV **Jambor I**, Pesola M, Taimen P, Merisaari H, Boström P, Minn H, Liimatainen T, Aronen HJ: Rotating frame relaxation imaging of prostate cancer: repeatability, cancer detection and Gleason score prediction. *Magn Reson Med.* 2016 Jan;75(1):337–44.

V **Jambor I**, Pesola M, Merisaari H, Taimen P, Boström P, Liimatainen T, Aronen HJ: Relaxation along fictitious field, diffusion weighted imaging, and T2 mapping of prostate cancer: prediction of cancer aggressiveness. *Magn Reson Med.* 2016 May;75(5):2130–40

VI **Jambor I**, Boström PJ, Taimen T, Syvänen K, Kähkönen K, Kallajoki K, Montoya Perez I, Kauko T, Matomäki J, Ettala O, Merisaari H, Kiviniemi A, Aronen HJ. Rapid biparametric MRI and targeted biopsy in men with a clinical suspicion of prostate cancer (IMPROD trial). *J Magn Reson Imaging*. 2017 doi: 10.1002/jmri.25641.

VII **Jambor I**, Kuisma A, Kemppainen J, Merisaari H, Eskola O, Taimen P, Minn H. Prospective evaluation of ^{18}F-FACBC PET/CT, PET/MRI and multiparametric MRI in patients with intermediate to high risk prostate cancer (FLUCIPRO trial): correlation with prostatectomy findings. Manuscript

1. INTRODUCTION

Prostate cancer continues to be the most common cancer among men and the second most common cause of death (Siegel et al. 2016). Despite this high incidence, optimal methods for detection of prostate cancer and patient-tailored decision planning have yet to be established. Prostate specific antigen (PSA) and digital rectal examination (DRE) are commonly applied as screening methods in asymptomatic men. With the widespread use of PSA there has been a steady increase in the 5-year relative survival rate (De Angelis et al. 2014; Siegel et al. 2016), and the incidence of local lymph node metastasis has dropped to about 10% at the time of diagnosis (Swanson et al. 2006). However, the efficiency of PSA as a screening tool remains questionable due to concerns related to over- and under-treatment of PSA screening-detected prostate cancers (Bill-Axelson et al. 2008; Catalona et al. 2012). Thus, methods for improved risk stratification of men with a clinical suspicion of prostate cancer are needed. Selection of individualized prostate cancer management is essential to prevent overtreatment while improving survival rate and quality of life.

Magnetic resonance imaging (MRI) is a non-invasive imaging method using radiofrequency (RF) pulses in a high static magnetic field. Since the early 1990s, MRI has been applied to the study of prostate cancer (Hricak et al. 1994). Despite a recent surge in the use of MRI in patients with histologically confirmed prostate cancer, optimal MRI methods for men with a clinical suspicion of prostate cancer have yet to be found. Since men with PSA screening-detected prostate cancers are at greatest risk of overtreatment (Rosenkrantz & Taneja2015), non-invasive imaging methods capable of improving risk estimation could result in improved survival while limiting overtreatment.

Position emission tomography (PET) uses short-lived radioactive isotopes (tracers) to evaluate tissue metabolism. Although PET is widely applied in cancer detection and characterization, it has until now shown only a limited role in imaging of prostate cancer. ^{18}F-FDG is by far the most commonly used tracer but has a very limited role in prostate cancer detection and characterization (Salminen et al. 2002). Other tracers such as ^{11}C-acetate (Jambor et al. 2010; Jambor et al. 2012; Mena et al. 2012) and ^{11}C/^{18}F-choline (Umbehr et al. 2013) have demonstrated limited specificity for prostate cancer. Especially in the setting of primary diagnosis, development and validation of novel tracers which would be more cancer specific could provide tools for improved management and image-guided treatment (Seppala et al. 2009).

2. REVIEW OF THE LITERATURE

2.1. Anatomy of the prostate gland

The prostate gland is located in front of the rectum and below the urinary bladder. It is composed of muscular, fibrous, elastic, connective, glandular, nerve, vascular, and lymphatic tissue (Wilson2014). The shape of the prostate resembles a truncated cone with its base facing the bladder and its apex terminating at the membranous urethra. The prostate has four histologic zones: 1. the anterior fibromuscular stroma which does not contain any glandular tissue; 2. the transition zone (TZ) which surrounds the urethra and contains roughly 5–10% of glandular tissue; 3. the central zone (CZ) which contains the ejaculatory ducts and about 15–25% glandular tissue; and 4. the peripheral zone (PZ) containing around 70%–80% glandular tissue.

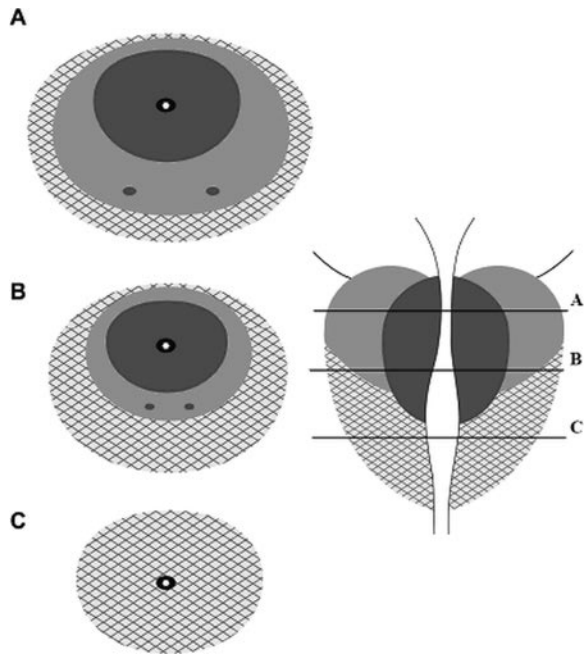

Figure 1. Schematic representation of the prostate zonal anatomy. The transition zone surrounds the urethra (dark gray); the central zone (light gray) contains the ejaculatory ducts (dark gray dots) and the outer peripheral zone (hashed) contains 70%–80% glandular tissue.

2.1. Prostate cancer

2.1.1. Incidence and mortality of prostate cancer

Prostate cancer is the most common cancer among men and the second most common cause of death in developed countries (Siegel et al. 2016). In 2013, 5124 new prostate cancer cases were diagnosed in Finland and the prostate cancer-specific mortality was 854, which represents 13.4% of all cancer-related deaths in men (www.cancerregistry.fi). Prostate cancer is diagnosed mainly after the age of 50 years and, based on autopsy studies, histological evidence of prostate cancer is present in roughly one third of men older than 50 years (Dall'Era et al. 2008). However, the majority of these cancers are likely clinically insignificant (Dall'Era et al. 2008). There has been a steady increase in the 5-year relative survival rate of patients with prostate cancer, from 73.4% in 1999–2001 to 83.4% in 2005–2007 in Europe (De Angelis et al. 2014). It is estimated that the total economic costs of prostate cancer in Europe are in excess of EUR 8.43 billion (Heidenreich et al. 2014).

2.1.2. Histopathology of prostate cancer

Approximately 70%–75% of prostate cancers originate in the PZ and 20%–30% in the TZ. Tumors in the CZ are uncommon and mainly secondary to invasion by a tumor in the PZ

(https://www.acr.org/~/media/ACR/Documents/PDF/QualitySafety/Resources/PIRADS/PIRADS%20V2.pdf). Prostate cancer is multifocal (Figure 2) in up to 85% of patients (Eichelberger & Cheng2004). Small-volume prostate cancers (<0.5 cm^3) in particular tend to be multifocal. However, in a study by Cheng et al., 16% of tumors with volume below 0.5 cm^3 had Gleason grade 4, implying that these tumors might potentially be clinically significant (Cheng et al. 2005).

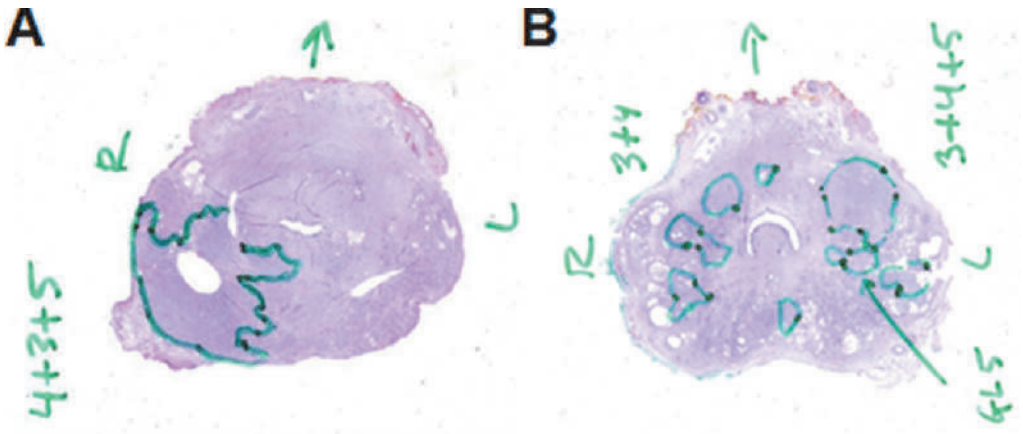

Figure 2. Example of unifocal (A) and multifocal (B) prostate cancer on a whole-mount prostatectomy section

Evaluation of prostate cancer in biopsy or prostatectomy specimens is most commonly done using a Gleason grading system (Epstein et al. 2005). The Gleason grading system was developed by Dr. Donald Gleason in 1966 (Gleason1966) and has undergone several modifications (Epstein et al. 2005). The Gleason grade range is from 1 to 5, but in current clinical practice for prostate cancer it starts at 3. In biopsy samples the Gleason score is a combination of the most common and highest Gleason grades (Epstein et al. 2005), and in prostatectomy samples a combination of the most common and second most common grades. Gleason grade 3 (Figure 3) is defined as discrete, well-formed cancer glands. Ill-defined glands with poorly formed glandular lumens in addition to fused microacinar glands, large cribriform glands and cribriform glands with an irregular border and hypernephromatoid cells are associated with Gleason grade 4 (Shah & Zhou2016). Gleason grade 5 is the most aggressive and can vary in appearance from no differentiation to solid tumor sheets or comedocarcinoma with central necrosis (Shah & Zhou2016).

The Gleason grade is an independent predictor of biochemical recurrence (D'Amico et al. 1998), but inter-observer variation can occur. Moreover, it has been noted that patients with morphologically identical prostate cancers can present with different patterns of progression (Hughes et al. 2005). Nevertheless, the Gleason

grading system remains the most widely used and accepted grading system for prostate cancer aggressiveness.

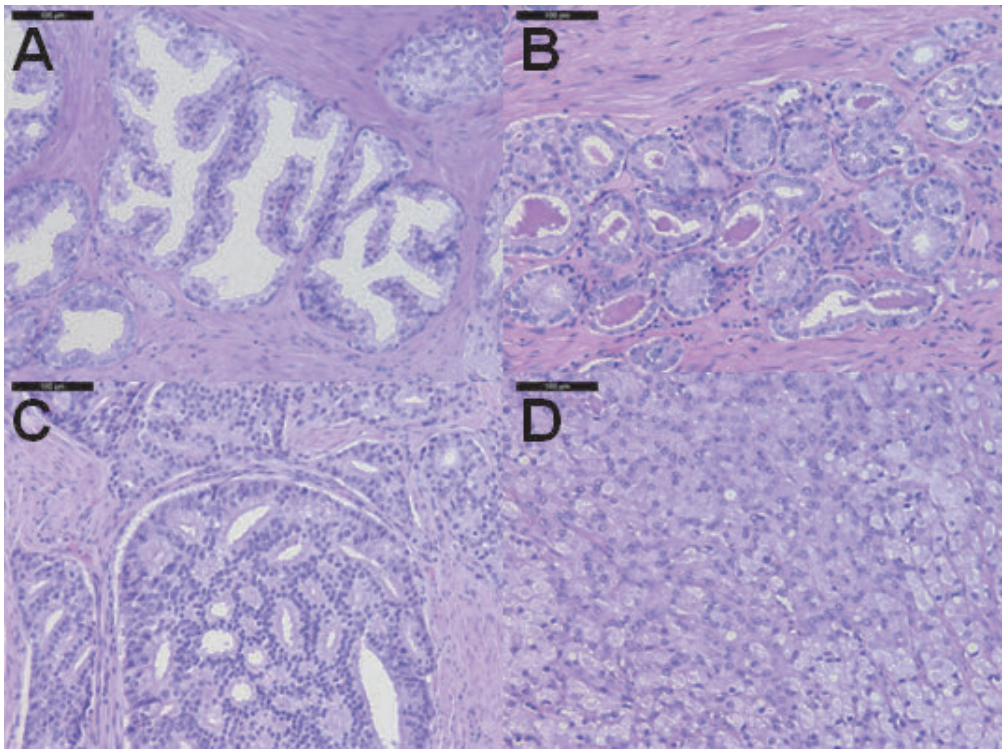

Figure 3. Example of normal prostate ducts (A), Gleason grade 3 (B), Gleason grade 4 cancer (C), Gleason grade 5 cancer (D).

The pathological TNM staging is summarized in Table 1.

Table 1. Pathologic TNM staging of prostate cancer

Pathologic TNM Staging	
Primary tumor (T)	
pT2	Organ confined
pT2a	Unilateral, involving one-half of 1 lobe or less
pT2b	Unilateral, involving more than one-half of 1 lobe but not both lobes
pT2c	Bilateral disease
pT3	Extraprostatic extension
pT3a	Extraprostatic extension or microscopic invasion of the bladder neck
pT3b	Seminal vesicle invasion
pT4	Invasion of the bladder and rectum
Regional lymph nodes (N)	
PNX	Regional nodes not sampled
pN0	No positive regional nodes
pN1	Metastases in regional nodes(s)

2.1.3. Detection and diagnosis of prostate cancer

Prostate cancer is most commonly diagnosed with systematic transrectal ultrasound (TRUS) guided biopsy. Prostate-specific antigen (PSA) and digital rectal examination (DRE) are commonly used screening methods to estimate the risk of prostate cancer (Carroll et al. 2015). The National Comprehensive Cancer Network (NCCN) Prostate Cancer Early Detection, Version 2.2015 (Carroll et al. 2015) guidelines recommend PSA testing for early detection of prostate cancer. PSA is a glycoprotein secreted by prostatic epithetical cells, and it enters the circulation by an unknown mechanism. However, it is not a prostate cancer-specific marker, and elevated levels of PSA can occur in benign conditions such as benign prostatic hyperplasia (BPH) or prostatic intraepithelial neoplasia (PIN). In the Prostate Cancer Prevention Trial (PCPT), which included 18,882 men, a sensitivity of 32% and specificity of 87% were found for a PSA cutoff value of 3.1 ng/mL (Thompson et al. 2005). However, even high Gleason grade cancers can be found in men with PSA levels of 4.0 ng/ml or less (Thompson et al. 2004). According to the NCCN Prostate Cancer Early Detection, Version 2.2015 (Carroll et al. 2015) guidelines for men with PSA >3.0 ng/ml DRE, repeat PSA and workup for benign disease should be done first before proceeding to TRUS-guided biopsy. An elevated PSA and/or abnormal DRE are triggers for systematic TRUS-guided biopsy (Carroll et al. 2015). DRE alone should not be used as a screening tool for early prostate cancer detection. In fact, only 0.4% of men had abnormal DRE and PSA levels below 2.5 ng/ml in a study by Hattangadi et al. (Hattangadi et al. 2012).

In order to increase the specificity of serum PSA while maintaining high sensitivity to prostate cancer, especially for Gleason score ≥3+4, other tests and PSA derivatives are recommended for consideration in patients with PSA >3.0 ng/ml (Carroll et al. 2015). These include free PSA (fPSA), the 4Kscore Test, the Prostate Health Index, and the prostate cancer gene 3 test. Free PSA is the ratio of unbound PSA to total PSA. Using a cut off value of 25% or below, 95% of prostate cancer can be detected in men with a PSA level of 4–10 ng/ml while avoiding 20% of biopsy procedures (Partin et al. 1998). The use of fPSA for early detection of prostate cancer has been approved by the US Food and Drug Administration (FDA). Another PSA parameter is the PSA density (dPSA), which is the ratio between the absolute PSA value and the prostate volume as estimated by TRUS. It has been shown that dPSA provides similar results to fPSA in the algorithms aimed at early detection of prostate cancer (Radwan et al. 2007). The 4Kscore Test is a combination test that measures serum PSA, fPSA, human kallikrein 2 and intact PSA. In addition, it considers age, DRE results and prior biopsy status. The 4Kscore Test had an area under the curve (AUC) of 0.82 for prostate cancer detection in a trial involving 1012 men (Parekh et al. 2015). The Prostate Health Index is a combination of serum PSA, fPSA and proPSA and has been approved by FDA for early detection of prostate cancer in men with serum PSA between 4 and 10 ng/ml. The Prostate Cancer Prevention Trial Risk Calculator 2.0 (PCPTRC) (Kranse et al. 2008; Thompson et al. 2006) is another combined calculator that is based on age, race, DRE findings, serum PSA, and biopsy history, all of which can be applied to estimate the prostate cancer risk. The AUCs of PCPTRC for prostate cancer detection were reported to be in the range 0.562–0.744 (Ankerst et al. 2014; Lundon et al. 2015; Trottier et al. 2011).

The efficiency of PSA as a screening tool remains questionable due to concerns related to over- and under-treatment of PSA screening-detected prostate cancers (Bill-Axelson et al. 2008; Catalona et al. 2012). Moreover, factors such as 5α-reductase inhibitors (D'Amico & Roehrborn2007) and some herbal supplements such as saw palmetto can affect serum levels of PSA. In the European Randomised Study of Screening for Prostate Cancer (ERSPC), around 182,000 men in the age range 50–74 years were randomized either to a group offered PSA screening at an average of once every 4 years or to a control group. The authors (Schröder et al. 2012) reported that PSA-based screening reduced mortality from prostate cancer in an 11-year follow up period by 21%. At a 13-year follow up, 781 men were re-invited for PSA screening, with 27 additional prostate cancers detected and one averted prostate cancer death (Buzzoni et al. 2015). In the Göteborg Randomised Population-Based Prostate-Cancer Screening Trial (Hugosson et al. 2010), a 44% reduction in prostate cancer specific death was observed in the screening group compared with the control group. By contrast, in the Prostate, Lung, Colorectal, and Ovarian Cancer Screening (PLCO) Trial no statistically significant difference was found between the disease-specific mortality rates of the screening and control groups at 13-year follow up (Andriole et al. 2012).

In the recently completed UK National Institute for Health Research-supported Prostate Testing for Cancer and Treatment (ProtecT) trial (Hamdy et al. 2016), no significant differences in prostate cancer specific mortality or all-cause mortality were found among men with prostate cancer detected by PSA screening at a median of 10 years follow-up who were randomly assigned to active surveillance, radical prostatectomy, or radical conformal radiotherapy with neoadjuvant hormonal therapy. However, higher rates of metastases and disease progression were present among men in the active surveillance group compared with men treated with prostatectomy or radiotherapy.

Due to the low specificity of PSA and consequent risk of overtreatment, the United States Preventive Services Task Force has recommended against routine use of PSA for screening for prostate cancer (Moyer2012), and the widespread use of PSA screening as a trigger for systematic TRUS-guided biopsy remains questionable (Djulbegovic et al. 2010). Nevertheless, with the introduction of PSA screening the incidence of local lymph node metastasis at time of diagnosis has dropped to approximately 10%. (Swanson et al. 2006). On April 11, 2017, the United States Preventive Services Task Force made the Draft Evidence Review of PSA prostate cancer screening available for public review. The draft statement also changed the use of PSA in men aged 55–69 years to category C (shared decision planning).

2.1.4. Management of prostate cancer

Due to the wide range of prostate cancer aggressiveness, selection of the appropriate management is essential to prevent the current trend of overtreatment. The clinical TNM staging of prostate cancer is summarized in Table 2.

Table 2. Clinical TNM staging of prostate cancer

Clinical TNM staging	
	Primary tumor (T)
TX	Primary tumor cannot be assessed
T0	No evidence of primary tumor
T1	Clinically inapparent tumor not palpable or visible by imaging
T1a	Tumor incidental histologic finding in ≤5% of tissue resected
T1b	Tumor incidental histologic finding in >5% of tissue resected
T1c	Tumor identified by needle biopsy (due to PSA)
T2	Tumor confined within prostate; tumors found in 1 or both lobes by needle biopsy but not palpable or reliably visible by imaging
T2a	Tumor involves one-half of 1 lobe or less
T2b	Tumor involves more than one-half of 1 lobe but not both lobes
T2c	Tumor involves both lobes
T3	Tumor extends through the prostatic capsule
T3a	Extracapsular extension (unilateral or bilateral)
T3b	Tumor invading seminal vesicle(s)
T4	Tumor fixed or invades adjacent structures other than seminal vesicles
	Regional lymph nodes (N)
NX	Regional nodes not sampled
N0	No positive regional nodes
N1	Metastases in regional node(s)
	Distant lymph nodes (N)
M0	No distant metastasis
M1	Distant metastasis
M1a	Nonregional lymph nodes(s)
M1b	Bone(s)
M1c	Other site(s) with or without bone disease

Prostate cancer clinical risk groups (Mohler et al. 2016) are defined as follows:
Very low:
• T1c
• Gleason score ≤6
• PSA <10 ng/mL
• Fewer than 3 prostate biopsy cores positive, 50% cancer in each core
• PSA density <0.15 ng/mL/g
Low:
• T1-T2a
• Gleason score ≤6
• PSA <10 ng/mL
Intermediate:
• T2b-T2c or
• Gleason score 7 or
• PSA 10–20 ng/mL
High:
• T3a or
• Gleason score 8–10 or
• PSA >20 ng/mL

Very high:
• T3b-T4 or
• Primary Gleason pattern 5 or
• >4 scores with Gleason score 8–10

Serum PSA, DRE, biopsy Gleason score and clinical TNM stage (based on bone scan, CT or MRI) are part of the NCCN guidelines (Mohler et al. 2016) for treatment selection of prostate cancer. Clinical nomograms aimed at improved selection of treatment are continuously being developed (Mohler et al. 2016; Partin et al. 2001). Preoperative PSA, pathological stage (Table 1), margin status and prostatectomy Gleason score were demonstrated to be independent predictors of biochemical recurrence (Graefen et al. 2001). However, clinical stage (Table 2) and Gleason grade based on systematic TRUS-guided biopsy were not independent predictors of organ-confined disease (Graefen et al. 2001), stressing the need for improved pretreatment characterization of prostate cancer.

In patients with non-metastatic prostate cancer, radical prostatectomy, radiotherapy (plus or minus androgen ablation) and active surveillance are the most commonly used treatment modalities, while focal ablative techniques, such as focused ultrasound, are less established methods (Mohler et al. 2016). There is still limited evidence for the clear benefit of one treatment modality over another (Dal Pra & Souhami2016). It appears that in patients with localized prostate cancer (stages T1 and T2), the benefit of radical prostatectomy is limited (Johansson et al. 1997). Thus, it is of utmost clinical importance to differentiate cancers that will progress and need active treatment from those that are best left to active surveillance.

2.2. Magnetic resonance imaging of suspected or primary prostate cancer

2.2.1. Physical basis of MRI

Magnetic resonance imaging uses radio-frequency (RF) energy (pulse) emitted by the RF coil to generate a magnetic field with subsequent excitation and relaxation processes. Hydrogen protons placed in an external static magnetic field are subjected to a turning force (torque), causing them to generate their own small magnetic field, or magnetic moment. “Spin” is a property associated with the magnetic moment. Based on quantum mechanics, protons cannot align exactly with the external static magnetic field, as the torque makes them precess. The precession frequency is given by the Larmor equation:

$$\omega_0 = \gamma B_0 \qquad \text{Eq. 1}$$

where γ is the Gyromagnetic ratio (2.7×10^8 Rad s^{-1} T^{-1}).

The vector sum of all spins is called the net magnetization (M_0). At 37 degrees Celsius and an external static magnetic field of 1.5 Tesla (T), there are roughly 1.000004 times more spins in the spin-up than in the spin-down direction. The RF pulse creates a magnetic field perpendicular to B_0 (static magnetic field) and oscillates

at the Larmor frequency. The RF pulse introduces coherence to all spins, meaning that all spins point in the same direction. Following the rotation of M_0 into the transverse plane, a receiver coil detects the RF field induced by magnetization returning to the B_0 direction. This signal is known as Free Induction Decay (FID). In MRI, the free induction decay signal is not used to generate an image, but echoes are generated that will produce one.

In the gradient echo sequence (Figure 4), a negative gradient lobe is applied immediately after the RF pulse and results in fast dephasing of FID. Subsequently, positive gradient lobes are applied, which reverses the magnetic field gradients. Spins that were dephasing will start to rephase and after some time align to form a gradient echo. Since a positive gradient lobe can only compensate for a negative gradient lobe, it does not refocus dephasing. The resulting signal is described as follows:

$$SE_{GE} = S_0 \exp\left(-\frac{TE}{T_2^*}\right) \qquad \text{Eq. 2}$$

where S_0 is the initial height of FID, T_2^* is the composite relaxation time which includes T_2 relaxation, tissue susceptibility, diffusion of protons, and inhomogeneities in the B_0 field.

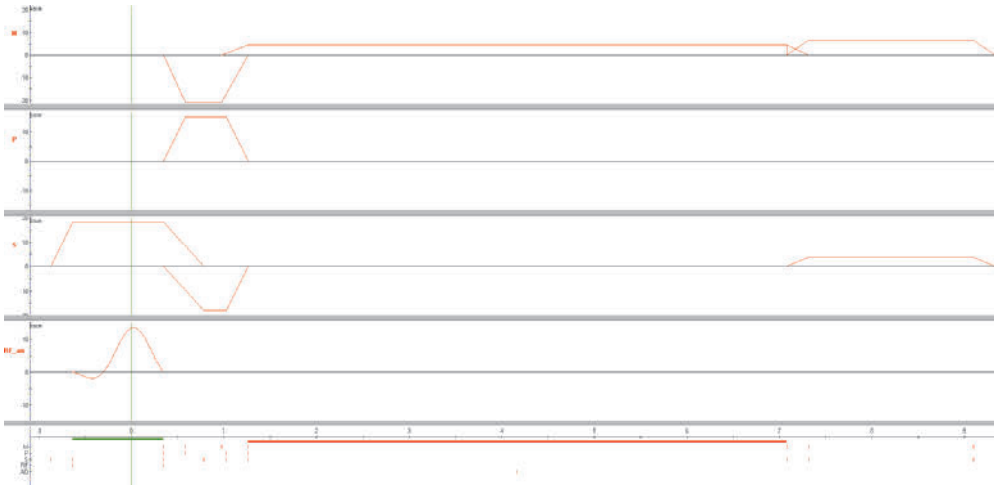

Figure 4 Pulse sequence diagram of a gradient echo sequence as shown in a Philips pulse programming environment.

In a spin echo sequence (Figure 5), spins dephase after a 90^0 pulse for some time, after which a 180^0 pulse is applied which flips all the spins. Although the phase angles of the dephasing are reversed, the precession frequencies are not altered. After time equal to the delay between the 90^0 pulse and 180^0 pulse, all spins will form a spin echo and the resulting signal is described as follows (Eq. 3):

$$SE_{SE} = S_0 \exp\left(-\frac{TE}{T_2} - \frac{2}{3}\gamma^2 \Delta B^2 D\left(\frac{TE}{2}\right)^3\right) \qquad \text{Eq. 3}$$

where S_0 is the initial height of FID, ΔB relates to inhomogeneities in the B_0 field, and D is the apparent diffusion coefficient of the protons.

Since the second term is much smaller than the first, Eq. 3 can be rewritten as:

$$SE_{SE} = S_0 \exp\left(-\frac{TE}{T_2}\right) \qquad \text{Eq. 4}$$

T_2^* is the composite relaxation time which includes T2 relaxation, diffusion of protons and tissue susceptibility. T_2 is longer than the corresponding T_2^*.

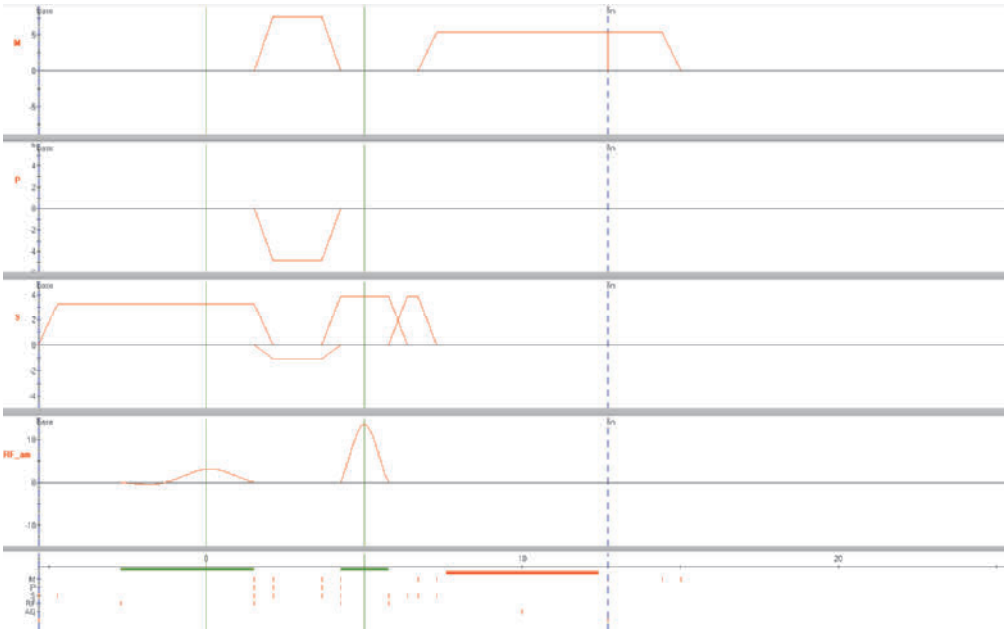

Figure 5 Pulse sequence diagram of a spin echo sequence as shown in a Philips pulse programming environment.

2.2.2. Anatomic magnetic resonance imaging of the prostate

T2-weighted images provide an overview of the prostate zonal anatomy. The normal PZ has homogeneous high signal intensity on T2-weighted images due to its relatively high water content (Figure 6). The central gland, which consists of the CZ and TZ, has a lower signal intensity compared to the PZ and a heterogeneous signal intensity due to its stroma-rich composition. A hypointense "pseudocapsule" separates the central gland from the PZ. The neurovascular bundles are located posterolaterally to the "true" outer prostate capsule at about the 5- and 7-o'clock positions on an axial image. The seminal vesicles are hyperintense tubular structures visible posteriorly to the base of the prostate. No zonal anatomy can be seen on T1-weighted images.

Benign prostatic hyperplasia appears on T2-weighted images as nodules with mixed high and low signal intensity, well-defined margins and a visible capsule (Figure 6).

In the early 1990s, anatomical MRI was shown to have higher accuracy for prostate cancer detection than either TRUS or DRE (Hricak et al. 1994; Mullerad et al.

2005; Presti, Jr. et al. 1996). Prostate cancer in the PZ appears as round or ill-defined, low-signal-intensity foci on T2-weighted images (Figure 7). Tumors in the TZ/CZ appear as homogeneous low-signal-intensity lesions with irregular margins and without a capsule.

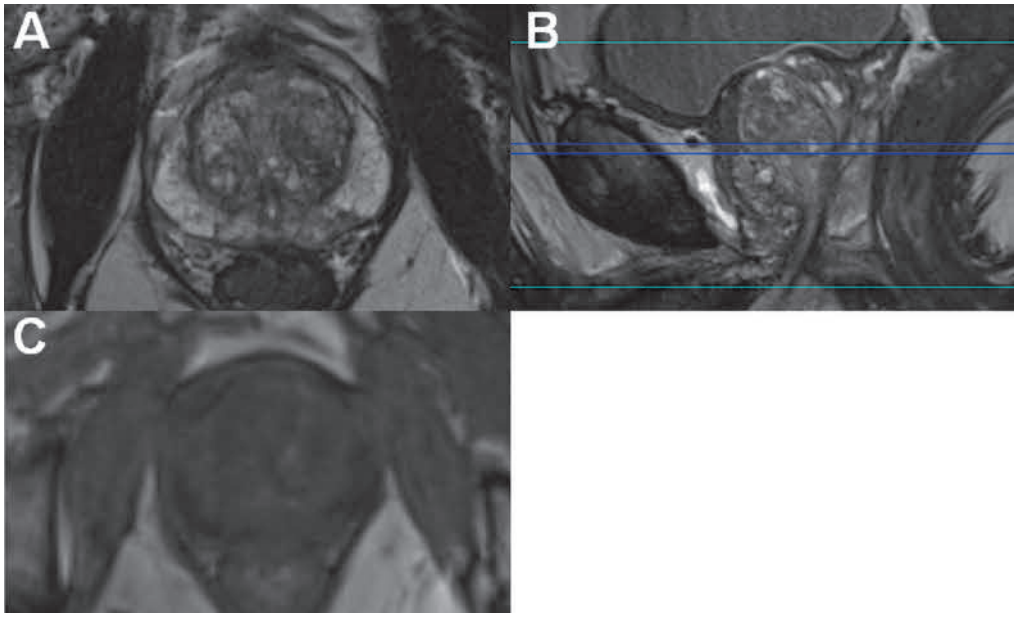

Figure 6. Transversal T2-weighted, sagittal T2-weighted, and transversal T1-weighted images of a 67-year-old man with a PSA value of 4.1 ng/ml. In this cross-section the normal PZ has a high signal intensity and the central gland (CZ and TZ) an intermixed signal intensity with presence of BPH. No zonal anatomy is visible on the T1-weighted image (C).

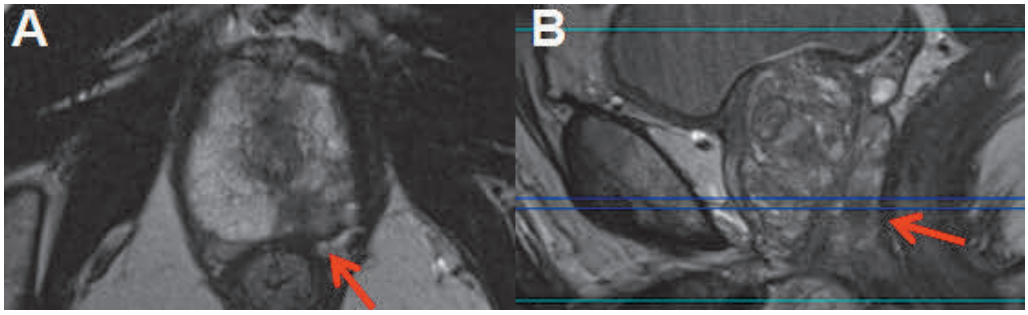

Figure 7. Transversal and sagittal T2-weighted images from the same 67-year-old man as in Figure 6. In this cross-section a low-signal-intensity lesion, indicated by the arrow, is present in the right PZ at the level of the apex. The lesion was confirmed to be Gleason score 3+4 prostate cancer.

2.2.3. Diffusion weighted imaging of the prostate

Diffusion behavior at tissue level can be measured using a Stejskal-Tanner imaging sequence (Stejskal 1965) (Figure 8). Information about proton diffusion is acquired by applying motion-encoding gradients, which cause phase shifts in moving protons. This

phase shift depends on the quantity as well as direction of movement (Bammer2003). The first gradient dephases and the second gradient rephases stationary protons while moving water protons stay dephased, resulting in decreased signal intensity. The signal attenuation depends on the water diffusion coefficient (D [mm^2/s]) and on the direction of the self-diffusion of water. The strength of diffusion weighting is controlled by the b value:

$$b = \gamma^2 G^2 \delta^2 \left(\Delta - \frac{\delta}{3} \right) \qquad \text{Eq. 5}$$

where γ denotes the gyromagnetic ratio, G the diffusion gradient amplitude, δ the diffusion gradient duration and Δ the time between the leading edges of the diffusion gradient pulses. In clinical practice, diffusion-weighted imaging data sets are commonly acquired using a spin echo sequence with echo planar imaging (epi read-out) (Figure 8). Although an epi readout is very time efficient, it is susceptible to B_0 field inhomogeneities (Figure 9).

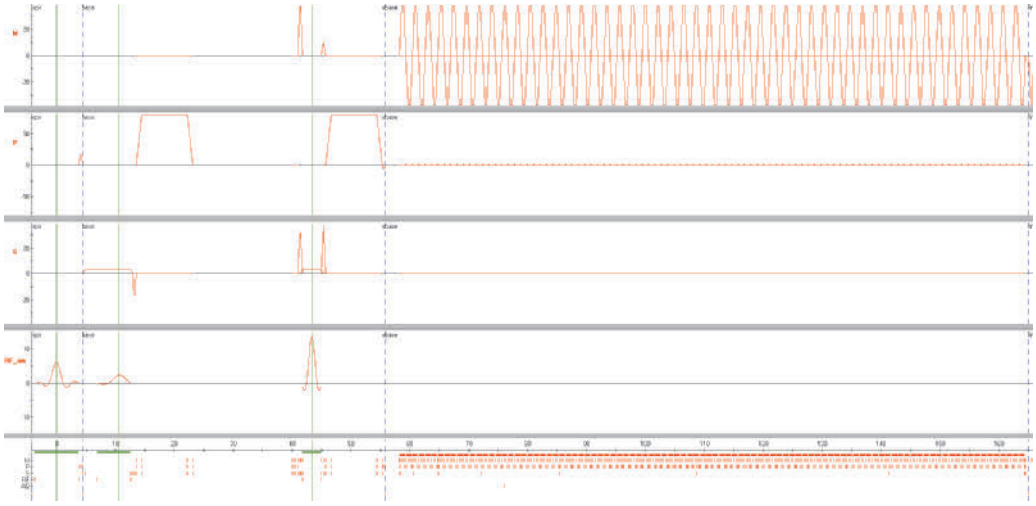

Figure 8. Pulse sequence diagram of a spin echo sequence epi readout and monopolar motion probing gradient as shown in a Philip pulse programming environment. Note the inversion pulse for fat suppression.

Various models, functions, and fitting methods (Merisaari et al. 2016) have already been applied to model DWI signal decay of the normal prostate (Jambor et al. 2014) and prostate cancer (Bourne et al. 2012; Bourne et al. 2014; Chatterjee et al. 2015; Toivonen et al. 2015). In general, a biophysical model has parameters that have clear biophysical meaning and assumptions. One such model is the intravoxel incoherent motion imaging model (IVIM), which models DWI signal decay at low b values (Le et al. 1988).

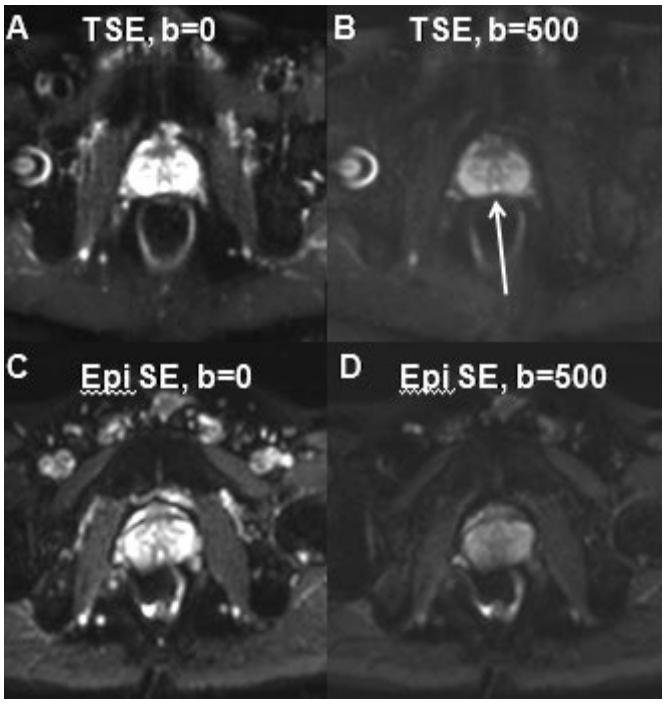

Figure 9. Comparison of prostate DWI done with turbo spin echo readout (TSE) (A, B) versus epi readout. Images acquired using epi readout are severely distorted. The Mullerian duct cyst (B, white arrow) can be seen only on images acquired using TSE readout.

The most commonly used models are the following (Figure 10):

1. Monoexponential function (Cescato et al. 2008) (Figure 11):

$$S(b) = S_0\left(e^{-bADC_m}\right) \quad \text{Eq. 6}$$

where S(b) is the signal intensity at a particular b value, S_0 is the signal intensity at b=0 s/mm^2, and ADC_m is the diffusion coefficient of the monoexponential function.

2. Kurtosis function (Jensen et al. 2005):

$$S(b) = S_0\left(e^{(-bADC_k + \frac{1}{6}b^2 ADC_k^2 K)}\right) \quad \text{Eq. 7}$$

where S(b) is the signal intensity at a particular b value, S_0 is the signal intensity at b=0 s/mm^2, and ADC_k is the diffusion coefficient of the kurtosis function. K is the kurtosis term representing variance of the distribution of diffusivities in a multiexponential situation.

3. Stretched exponential function (Bennett et al. 2003; Hall & Barrick2008)

$$S(b) = S_0\left(e^{-(bADC_s)^{\alpha}}\right) \quad \text{Eq. 8}$$

where S(b) is the signal intensity at a particular b value, S_0 is the signal intensity at b=0 s/mm^2, ADC_s is the characteristic relaxation rate (Johnston et al. 2005) of the stretched exponential function, and α is the "anomalous exponent". The stretched exponential function has a non-physical nature, thus a physical interpretation of its parameters is not straightforward. It should be noted that the function in the range

$0<\alpha<1$ is singular at b=0 s/mm^2 with an infinitely negative slope. Johnston (Johnston et al. 2005) evaluated the stretched exponential function as a continuous sum of pure exponential decays with a particular probability density function. In the same study, the ADC_s parameter was shown not to be related to any average of diffusion coefficients.

4a. Biexponential model for low b values, intravoxel incoherent motion imaging model (IVIM) (Le Bihan et al. 1988):

$$S(b) = S_0\left[fe^{-bDp} + (1-f)e^{-bD_f}\right] \quad \text{Eq. 9}$$

where S(b) is the signal intensity at particular b value, f_p is the "pseudodiffusion" fraction, D_f is the fast diffusion coefficient, and D_p is the "pseudodiffusion" coefficient. The intravoxel incoherent motion imaging model (IVIM) is a biophysical model modeling blood flow in the capillaries that causes a dephasing of the blood magnetization when motion-encoding gradients are applied. This motion of water molecules due to the microcirculation of blood in the randomly oriented capillaries has a similar impact on the resulting MRI signal, as their motion is due to molecular diffusion (intra- and extracellular diffusion). However, the "pseudo-diffusion fraction is not directly proportional to the tissue perfusion (Henkelman1990; Le Bihan & Turner1992).

4b. Biexponential model for high b values (Mulkern et al. 2005):

$$S(b) = S_0\left[fe^{-bDf} + (1-f)e^{-bD_s}\right] \quad \text{Eq. 10}$$

where S(b) is the signal intensity at a particular b value, f_f is the fraction of fast diffusion, D_f is the fast diffusion coefficient, and D_s is the slow diffusion coefficient.

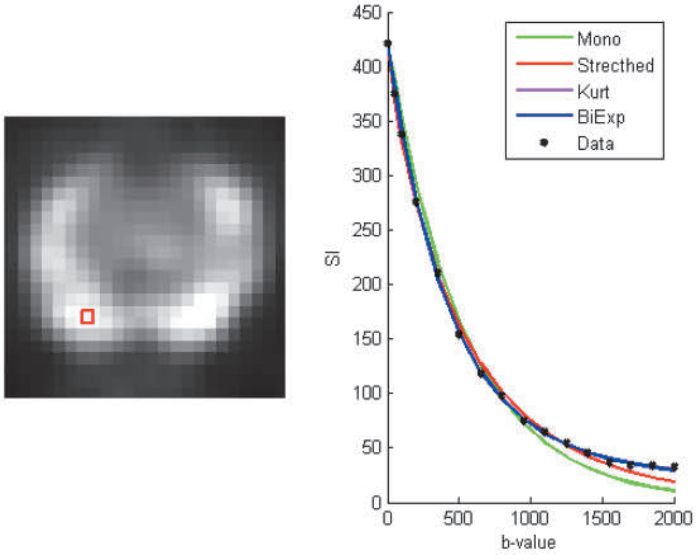

Figure 10. Diffusion-weighted imaging signal decay of the normal prostate fitted using four different mathematical models/functions. Mono=monoexponential, Stretched=stretched exponential, Kurt=kurtosis, BiExp=Biexponential.

Due to restricted diffusion, prostate cancer has lower diffusion coefficients (using a monoexponential fit) than normal tissue (Figure 10).

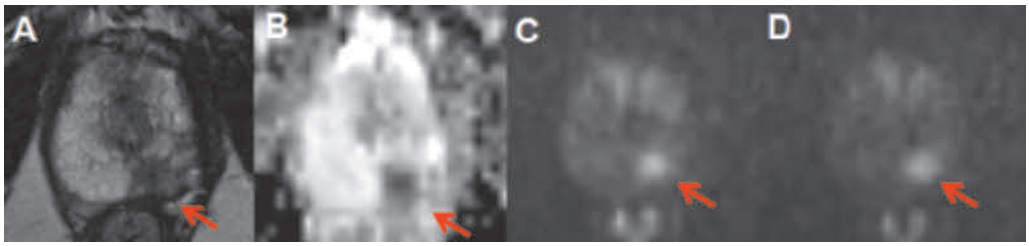

Figure 11. Transversal T2-weighted (A), transversal apparent diffusion coefficient map (b values 0, 100, 200, 350, 500 s/mm^2) (B), transversal trace b=1500 s/mm^2 (C), and transversal trace b=2000 s/mm^2 (D) images from the same 67-year-old man as in Figures 6 and 7. The red arrow indicates the lesion. Targeted biopsy revealed Gleason score 3+4 prostate cancer. The histologically confirmed prostate cancer demonstrates lower ADC values (B) and a higher signal on trace images (C, D) compared with normal tissue.

2.2.4. Proton magnetic resonance spectroscopy (^{1}H-MRS) of prostate

Proton magnetic resonance spectroscopy (^{1}H-MRS) is a non-invasive imaging technique that enables measurement of tissue metabolite concentrations using an MR scanner.

The most widely used acquisition sequences for prostate ^{1}H-MRS is the point-resolved spectroscopy (PRESS) sequence. A slice-selective excitation is combined with two slice-selective refocusing pulses of 180 degrees, resulting in two spin echos. The first spin echo contains a signal from the intersection between the first 180 refocusing degree pulse and slices selected by the 90-degree pulse. The second echo contains a signal from the intersection of the three planes selected by all three pulses (90-degree pulse, two 180-degree pulses). A small tissue metabolite signal can be contaminated by a fat signal from the tissue surrounding the prostate. Radio frequency pulses selectively inverting and dephasing water and lipid signals have been developed (Scheenen et al. 2004; Star-Lack et al. 1997) to limit contamination of the tissue metabolite signal by a fat signal. Moreover, weighted elliptical sampling of the k-space and averaging was shown to reduce lipid signals, intervoxel contamination and measurement time of prostate ^{1}H-MRS (Scheenen et al. 2004).

The shape of prostate tissue spectra is predominantly affected by echo time (TE). The observed dominant peaks originate from protons in citrate (approximately 2.72 parts per million((ppm)), green arrow in Figure 12), creatine (3.1 ppm, yellow arrow) and choline (approximately 3.20 ppm, red arrow). Depending on the acquisition sequence parameters and signal-to-noise, polyamine (Shukla-Dave et al. 2007) signals may also be observed at approximately 3.15 ppm. In normal epithelial prostate cells the citrate-oxidizing enzyme is inhibited by an abundance of zinc, resulting in accumulation of citrate (Costello et al. 2005). Citrate levels are higher in the PZ than in the central gland (CZ/TZ) and its proton spectrum arises from two CH_2 moieties. Citrate is a strongly coupled system due to the presence of two magnetically

inequivalent protons in each of the CH_2 moieties. The appearance of the resulting four citrate resonances is affected by magnetic field strength, echo time, timing parameters of sequence and radio frequency (RF) pulses (Scheenen et al. 2005).

Compared to normal prostate tissue, prostate cancer cells have lower zinc levels resulting in increased activity of aconitase, unopposed oxidation and ultimately lower citrate levels. The increased choline levels in prostate cancer cells are attributed to increased membrane synthesis cell turnover (Ramirez de et al. 2002).

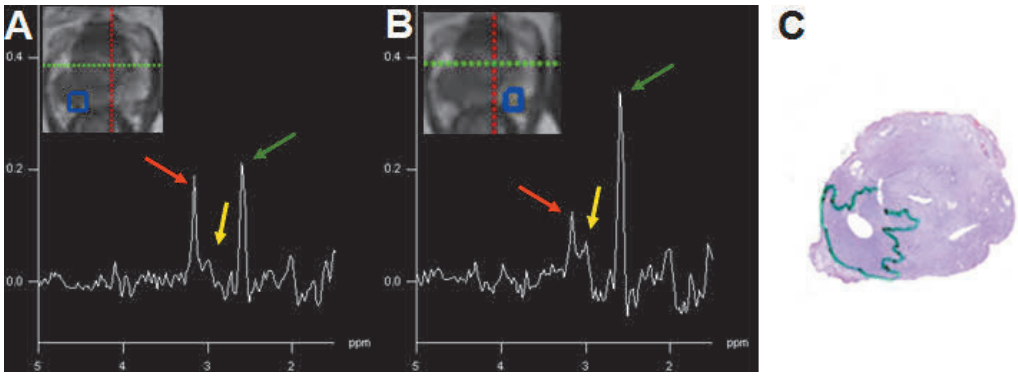

Figure 12. Spectrum from histologically confirmed prostate cancer (A) showing lower citrate peaks (green arrow) and higher choline (red arrow) plus creatine (yellow) peaks compared with a spectrum from the normal PZ (B) at 3T, (TR/TE: 750/140, number of acquisitions (NA) 8, Delta frequency 1.80 ppm, Hamming filter acquisition time 12:36 min). The prostate cancer area is outlined in green on the corresponding whole-mount prostatectomy sample (C) and the voxel location is shown in the upper left hand corner (A, B).

2.2.5. Dynamic contrast enhanced magnetic resonance imaging of prostate

Dynamic contrast-enhanced magnetic resonance imaging (DCE-MRI) uses intravenously injected contrast agents, most commonly low-molecular weight gadolinium (Gd) chelators, to alter relaxation times in tissue based on the concentration of the agent.

T_1 relaxation times are reduced in the presence of Gd:

$$\frac{1}{T_1} = \frac{1}{T_1} + r_1 C \qquad \text{Eq. 11}$$

where r_1 is the tissue relativity (typical in-vitro value of 4.5 s^{-1} mM^{-1}).

A series of sequentially acquired T_1-weighted images is acquired following rapid injection of a contrast agent to evaluate the effect of the agent on relaxation values. An optimal temporal resolution for prostate DCE-MRI is still under discussion, but already in 1996 Jager et al. (Jager et al. 1997) suggested 2 seconds. In general, temporal resolution is a trade-off between SNR and resolution. The development of new sequences, such as golden-angle radial k-space sampling methods (Rosenkrantz et al. 2015), enabled the acquisition of high-resolution scans with temporal resolution close to 2 seconds. In general, 3D sequences are preferred over slice-selective (2D) sequences due to better flip angle accuracy. Furthermore, B_1 non-

uniformity can result in variation of the flip angle across the imaging volume. Gradient echo sequences performed using a low flip angle (~5 degrees) have a higher signal at low contrast agent concentration but a limited signal intensity range as a function of contrast agent concentration. By contrast, the use of higher flip angles (~15 degrees) results in a wider signal intensity range as a function of contrast agent concentration, and is demonstrated to be necessary for estimation of arterial input function (AIF) (Parker et al. 2006).

Interpretation of DCE-MRI can be done qualitatively (visual evaluation of T_1-weighted images), semi-quantitatively (time-to-peak, integral AUC, ...) or in a quantitative manner performing modeling. Several models have been proposed to quantitatively model the DCE-MRI signal (Larsson et al. 1996; St Lawrence & Lee1998; Tofts et al. 1999). The Tofts model covers the following parameters: contrast medium in the plasma (C_p) (derived from the arterial input function (AIF)), fractional volumes of the extravascular extracellular space (v_e), the extracellular space of plasma in tissue (v_p), and blood vessel permeability (K^{trans}). The rate constant (k_{ep}) is defined by $k_{ep}= K^{trans}/v_e$. The "basic" Tofts model includes v_e and K^{trans}, and the "extended" Tofts model contains v_p (plasma contribution) as well. The "extended" model can be expressed as:

$$C_t(t) = K^{trans} \int_0^t C_p(\tau) e^{-k_{epo}(t-\tau)} d\tau + v_p C_p(t) \quad \text{Eq. 12}$$

where C_t is the tissue concentration. The intravascular component (v_p) in tissue is usually small (<10%) (Tofts1997).

The initial slope of the DCE-MRI is dependent on K^{trans} but is independent of v_e. However, the maximum enhancement is predominantly affected by v_e. K^{trans} values are sensitive to T_{10} (pre-contrast T_1 relaxation values), whereas k_{ep} are more robust. Prior knowledge of the contrast agent concentration in the plasma (C_p) is required for pharmacokinetic modeling, and this can be derived using AIF calculated from the blood signal. AIF can be measured for each subject or taken as a population average. Individual AIF can vary between subjects (Fedorov et al. 2014); it is either measured directly by inserting a catheter into an artery and sampling blood at given time intervals during DCE-MRI data acquisition, or estimated from an artery in the image field of view. The former is invasive and the latter requires the DCE-MRI data to be acquired at a high temporal resolution. Thus several population-based AIF methods have been proposed. The original biexponential Weinmann plasma curve is described analytically (Tofts & Kermode1991), and Parker's AIF was obtained using high temporal resolution MRI data (Parker et al. 2006). In addition, methods relying on population-averaged pharmacokinetic parameter values for a reference tissue (such as skeletal muscle) have been developed (Yankeelov et al. 2005).

Prostate cancer tissue typically enhances rapidly, followed by early washout (Figure 13).

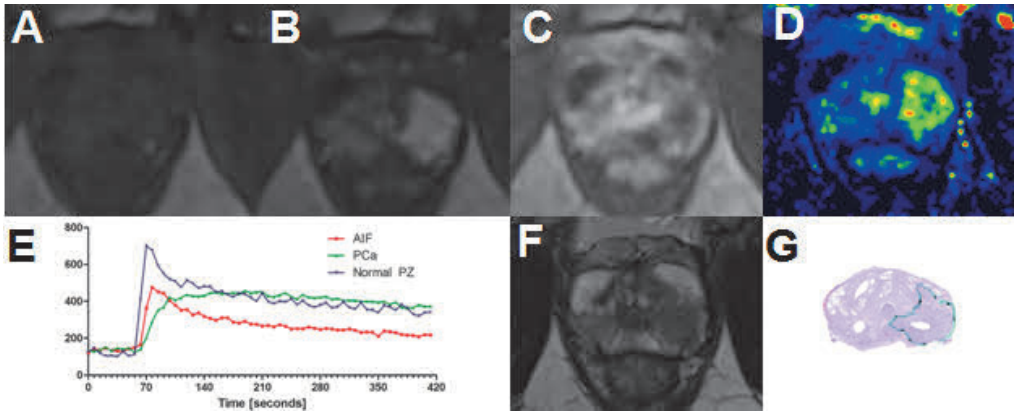

Figure 13. DCE-MRI of a 65-year-old patient (14.7 ng/ml, pTNM T2aN0). T_1-weighted image before injection of the contrast agent, showing a homogeneous signal intensity in the prostate (A). 77 seconds from the start of DCE-MRI acquisition (frame 11), the prostate cancer in the left lobe enhances rapidly compared to the normal PZ in the right lobe (B). Following peak enhancement, early washout occurs in the area of the prostate cancer (413 seconds from the start of DCE-MRI acquisition, frame 60) (C). K^{trans} values are increased in the left lobe (D) . On the T2-weighted image, the prostate cancer appears as an area of low signal intensity in the left lobe (F). The corresponding whole-mount prostatectomy section (tumor outline in green) demonstrates prostate cancer with a Gleason score of 4+3 (G). AIF = arterial input function, PCa = prostate cancer, Normal PZ = normal peripheral zone.

2.2.5. Spin-lock imaging

Spin-lock imaging, or rotating frame relaxometry, is based on relaxation in the presence of RF irradiation. The process of the longitudinal component of the magnetization vector approaching equilibrium in the presence of RF irradiation is called spin-lattice (longitudinal) relaxation in the rotating frame of reference ($T_{1\rho}$). If the pulse is in the zero or 180-degree spin-locking phase, the process of relaxation is transverse relaxation in the rotating frame of reference ($T_{2\rho}$). In contrast to diffusion or flow MRI-based measurements, spin-lock imaging has the potential to explore processes at low interaction frequencies of the order of kHz (Gilani & Sepponen2016). Various spin-locking pulses can be applied. If the RF pulse is applied off-resonance to the water peak, the method is termed rotating frame off-resonance imaging and is associated with a lower specific absorption rate (SAR) values than the on-resonance rotating frame.

Although several studies have demonstrated encouraging results for $T_{1\rho}$ and $T_{2\rho}$ measurement in musculoskeletal- (Borthakur et al. 2006), neuro- (Aronen et al. 1999; Michaeli et al. 2007; Ramadan et al. 1998), and preclinical imaging (Hakumaki et al. 2002; Kettunen et al. 2007; Liimatainen et al. 2012), these methods have not been applied to in-vivo prostate imaging. One of the major limitations at higher field is SAR. Most commonly $T_{1\rho}$ studies are preformed utilizing a "block pulse"/"hard pulse", "continuous wave" (cw) RF pulse ($T_{1\rho cw}$) (Figure 14) with a constant irradiation radiofrequency (ω_{RF}). Recently, a novel method called **r**elaxation **a**long a **f**ictitious **f**ield (RAFF) has been developed (Liimatainen et al. 2010). The RAFF

(Figure 15) method (T_{RAFF}) is based on measurements done in sub-adiabatic conditions with ~40% less SAR than $T_{1\rho}$ with the same peak power and block pulse duration.

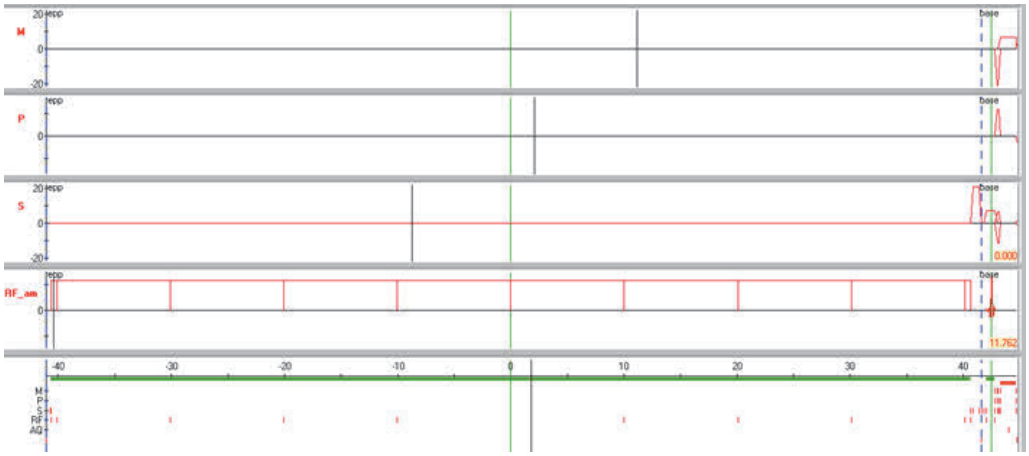

Figure 14. Pulse sequence diagram of a continuous wave pulse of 80 ms duration and 500 Hz peak pulse amplitude as shown in a Philip pulse programming environment.

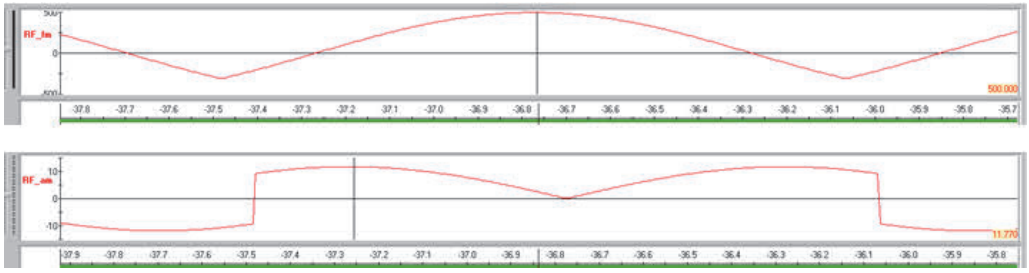

Figure 15. Pulse diagram of a RAFF pulse with peak amplitude of 500 Hz as shown in a Philip pulse programming environment.

2.2.6. Multiparametric magnetic resonance imaging in men with a clinical suspicion of prostate cancer

The National Cancer Institute of the United States conducted a single institution trial (clinicaltrials.gov Identifier: NCT00102544) between August 2007 and February 2014 to evaluate targeted MRI-TRUS fusion prostate biopsy in men with a clinical suspicion of prostate cancer (Siddiqui et al. 2015). Only men with at least one multiparametric magnetic resonance imaging (mpMRI) target were enrolled. The imaging was performed using an endorectal coil at 3T and consisted of T2w, DWI (5 evenly-spaced b values between 0 and 750 s/mm^2, no b values above 1500 s/mm^2) ^{1}H-MRS and DCE-MRI. In total, 1003 men were included, of whom 196 (20%, 196/1003) were biopsy naïve (no history of previous biopsy). Clinically significant prostate cancer was defined as a biopsy Gleason score of 3+4 with ≥50% of any core containing, and/or ≥4 systematic TRUS-guided biopsy core positive for, prostate cancer. In prostatectomy specimens, clinically significant prostate cancer was defined as Gleason score 3+4 and PCa of ≥20% of the whole prostate volume. Prostate cancer

detection rates between MRI-TRUS fusion and TRUS-guided biopsy were similar (461 vs 469). However, MRI-TRUS fusion detected 30% more tumors with Gleason score ≥4+3 (173 vs 122, p<0.001) and 17% fewer clinically non-significant tumors (213 vs 258, P<0.002) compared with TRUS-guided biopsy. Since only men with at least one mpMRI target were enrolled, a negative predictive value of mpMRI in patients with a clinical suspicion of prostate was not evaluated.

In a single institution randomized trial (ClinicalTrials.gov identifier: NCT01357512), 130 biopsy-naïve men with elevated PSA (PSA <20 ng/ml or free-to-total PSA ratio ≤0.15 and PSA <10 ng/ml) were randomized to the mpMRI group or to the control group. Men in the mpMRI group with mpMRI-detected lesion(s) had 10- to 12-core TRUS-guided biopsy and cognitively targeted TRUS-guided biopsy of the lesion(s). The enrolment period was April 2011 to December 2014. The mpMRI was performed using surface array coils at 3T and consisted of T2w, DWI (3 b values of 50, 300, and 800 s/mm^2) and DCE-MRI. The authors defined clinically significant prostate cancer as Gleason score >3+3, more than two positive cores, or maximum cancer core length >3 mm (Puech et al. 2009). The differences in the prostate cancer and clinically significant prostate cancer detection rates between the groups were similar: 64% vs 57% and 55% vs 45%, respectively, and not statistically significant. Thus, mpMRI followed by cognitively targeted TRUS-guided biopsy did not improve the prostate cancer detection rate over routine TRUS-guided biopsy.

In-bore MRI-guided prostate biopsy was compared with systematic TRUS-guided biopsy in a prospective randomized trial (ClinicalTrials.gov Identifier: NCT02220517), which enrolled 267 patients (Arsov et al. 2015) between November 2011 and July 2014. mpMRI was performed at 3T using surface array coils and consisted of T1w, T2w, DWI (5 evenly-spaced b values between 0 and 750 s/mm^2, no b values above 1500 s/mm^2), and DCE-MRI. A maximum of three lesions per patient were scored on a 5-point Likert scale for each MRI sequence (T2WI, DWI, DCE-MRI) and the individual scores were summed up to a score of 3–15 points. At a later stage of the trial (after April 2012), the PI-RADs version 1 reporting system was used with single scores and sum scores (Schimmöller et al. 2014). Men were randomized following mpMRI to in-bore MRI-guided biopsy (arm A) or MRI-TRUS fusion-guided biopsy and systematic TRUS-guided biopsy (arm B). The primary endpoint of the trial was powered at 80% to demonstrate an overall prostate cancer detection rate of ≥60% in arm B compared to 40% in arm A. The trial was interrupted prematurely, since at the interim analysis the authors found that the trial would not meet the primary endpoint. The authors concluded that a prospective comparison between MRI-targeted biopsy alone and systematic TRUS-guided biopsy is justified.

A study by Filson et al. (Filson et al. 2016) included 1042 men with a clinical suspicion of prostate cancer, of whom 328 (32%, 328/1042) had no history of biopsy. The patients were enrolled between September 2009 and February 2015. mpMRI was performed using surface array coils at 3T and consisted of T2w, DWI (b values not defined) and DCE-MRI. No mpMRI target was present in 38 men with no history of biopsy (n=328) and 47 men with a previous negative biopsy (n=324). Of these men, seven (18%, 7/38) and five (11%, 5/47) were diagnosed with Gleason score ≥3+4. In men with prior positive TRUS-guided biopsy, 21 (48%, 21/43) were diagnosed with Gleason score ≥3+4 and did not have any mpMRI target (n=43). The authors concluded that mpMRI cannot be used to rule out biopsy in patients with no mpMRI

target. Targeted MRI-TRUS fusion biopsy did not outperform systematic TRUS-guided biopsy, but the combination of targeted MRI-TRUS fusion and systematic TRUS-guided biopsy detected more Gleason score ≥3+4 than either modality alone.

In the PROMIS (Ahmed et al. 2017) trial (multicenter, paired-cohort), 576 (785, 576/740) men underwent 1.5 Tesla mpMRI followed by both TRUS-guided biopsy and transperineal template prostate mapping (TPM) biopsy. The authors reported mpMRI to be more sensitive (93%) than TRUS-guided biopsy (48%, $p<0.0001$), but less specific (41% for mpMRI vs 96% for TRUS-guided biopsy) when using TPM biopsy as a "gold standard". Based on these results the authors concluded that using mpMRI to risk-stratify men might allow 27% of patients to avoid a primary biopsy.

In a study by Pokorny et al. (Pokorny et al. 2014) of 223 biopsy-naïve men with elevated PSA (the authors did not report the specific enrolment PSA value), those with PI-RADs 1 or 2 (n=81) underwent mpMRI followed by 12-core TRUS-guided prostate biopsy, and those with PI-RADs 3 to 5 underwent MR-guided in-bore biopsy of suspicious lesion(s) (n=142) followed immediately by 12-core systematic TRUS-guided prostate biopsy. The enrollment period was July 2012 to January 2013. mpMRI was performed using surface array coils at 3T and consisted of T2w, DWI (b values not specified) and DCE-MRI. The authors defined clinically significant prostate cancer as: a) more than 6 mm and Gleason score 3+3; b) more than 4 mm and Gleason score 3+4; c) Gleason score 3+3 in more than two cores upon MR-guided biopsy or one core regardless of prostate cancer length upon systematic TRUS-guided biopsy; d) Gleason score 3+4 in more than one core regardless of prostate cancer length upon MR-guided biopsy and systematic TRUS-guided biopsy; and e) Gleason score 4+3 regardless of prostate cancer length. In 142 men with PI-RADs 3 to 5, 99 (69.7%) men were diagnosed with prostate cancer in cores of the MR-guided biopsy and 93 of those cancers were clinically significant. The authors reported that MR-guided biopsy in men with PI-RADs 3 to 5 led to a 51% reduction of biopsy need, an 89.4% decrease in the diagnosis of low-risk prostate cancer, and a 17.7% increase in the detection of clinically significant prostate cancer compared with TRUS-guided prostate biopsy in men with PI-RADs 1 or 2. However, of 81 men with PI-RADs 1 or 2, five (6%, 5/81) presented with clinically significant prostate cancer. Based on these results the authors concluded that mpMRI and in-bore MR-guided biopsy may limit overdiagnosis in the screening of prostate cancer using PSA.

Kuru et al. (Kuru et al. 2013) evaluated mpMRI-targeted, TRUS-guided transperineal fusion biopsy in 347 men, 49% with previous negative systematic TRUS-guided biopsies. If mpMRI lesion(s) were detected, targeted biopsy was performed followed by systematic sector-based biopsies of the whole gland performed under general anesthesia in an outpatient setting. The median number of biopsy cores per patient was 24 (range 12 to 36). The enrolment period was between June 2010 and December 2011. mpMRI was performed at 3T using surface array coils and consisted of T2w, DWI (7 b values of 0, 50, 100, 150, 200, 250, 800 s/mm^2), ^{1}H-MRS and DCE-MRI. Clinically significant prostate cancer was defined as Gleason score ≥3+4 or PSA ≥10 ng/ml. In 104 men with intermediate to highly suspicious mpMRI findings, 86 (83%, 86/104) and 62 (60%, 62/104) were diagnosed with prostate cancer and clinically significant prostate cancer, respectively. By contrast, in 149 and 94 men with questionable and non-suspicious (as defined by the authors) mpMRI findings,

respectively, 100 (67%, 100/149) and 80 (85%, 80/94) respectively were diagnosed with prostate cancer. In this study, mpMRI demonstrated a limited negative predictive value for the detection of prostate cancer, since a large proportion of men with questionable and non-suspicious mpMRI findings were diagnosed with prostate cancer upon transperineal biopsy.

Targeted MRI-TRUS fusion improved detection of prostate cancer and clinically significant prostate cancer (Gleason ≥3+4 or Gleason 6 with maximal cancer core length ≥4 mm) in patients with previous negative biopsy in a study by Sonn et al. (Sonn et al. 2014). The mpMRI degree of suspicion was the most powerful predictor of significant cancer on multivariate analysis. The study enrolled 105 men between March 2010 and August 2012; mpMRI was performed at 3T using surface array coils and consisted of T2w, DWI (3 b values of 400/800/1000 s/mm^2) and DCE-MRI.

Efforts to decrease the overall duration of prostate MRI while maintaining high diagnostic accuracy have resulted in studies using biparametric prostate MRI (bpMRI) (Fascelli et al. 2015; Radtke et al. 2015; Rais-Bahrami et al. 2015) consisting of T2w and DWI. A prediction model incorporating bpMRI findings with PSA and dPSA (Rais-Bahrami et al. 2015) was developed, giving AUCs for prostate cancer detection of 0.83–0.87. In a separate cohort of patients, the overall accuracy of bpMRI and serum PSA was 81.4% and that of bpMRI and dPSA 78.0% (Fascelli et al. 2015). The corresponding values for detection of Gleason score ≥3+4 were 74.6% and 78.0%.

2.3. Positron emission tomography of prostate cancer

Positron emission tomography (PET) is an imaging method that uses radiolabeled molecules (tracers) to study metabolism. It is widely used to study various cancer types. ^{18}F-labeled glucose (^{18}F-FDG) is the most widely used PET tracer. Increased glucose retention in tumors with upregulated glucose transporter expression (GLUT) and hexokinase activity form the basis for use of ^{18}F-FDG in tumor imaging. Unfortunately, ^{18}F-FDG has low sensitivity for prostate cancer detection (Liu et al. 2001). ^{11}C-Acetate is a tracer related to fatty acid metabolism and has been shown to be more sensitive than ^{18}F-FDG in the detection of prostate cancer (Oyama et al. 2002). Numerous studies have demonstrated rather limited specificity of ^{11}C-acetate for prostate cancer (Jambor et al. 2010; Mena et al. 2012) due to its uptake in benign conditions such as BPH and PIN. The use of anatomical MRI (T2w) allows partial improvement of specificity by identifying uptake originating from BPH (Jambor et al. 2012). Nevertheless, ^{11}C-acetate is not recommended for imaging of primary prostate cancer. ^{11}C/^{18}F-Choline accumulates in tumors due to upregulated choline kinase. Similarly to ^{11}C-acetate, ^{11}C/^{18}F-Choline has demonstrated low specificity for prostate cancer (Breeuwsma et al. 2005; de Jong et al. 2002; Umbehr et al. 2013). Thus, there is a need to develop and validate novel PET tracers which would have high sensitivity and specificity for prostate cancer.

Several tumors, including prostate cancer, have upregulated amino acid transport and synthesis (Huang & McConathy2013). Thus, amino acid-based PET tracer analogues present an attractive method for tumor detection and characterization. In general, peptides as PET tracers provide excellent characteristics because they can be easily synthesized, have fast and specific targeting features and are rapidly cleared

from the body, mainly via the renal pathway. L-^{11}C-methionine was studied in 20 patients with elevated PSA levels and negative prostate biopsies and demonstrated sensitivity of 100% but low specificity of 38% (Toth et al. 2005).

The potential of ^{68}Ga-labeled peptides to target tumor receptors has already been demonstrated in cases of somatostatin receptor imaging. ^{68}Ga-DOTATOC, ^{68}Ga-DOTANOC and ^{68}Ga-DOTATATE are available for diagnosis of neuroendocrine tumors in Europe (Ambrosini et al. 2010; Kumar et al. 2011). Aside from PET tracers targeting somatostatin receptors, peptides targeting G-protein coupled receptors have been found to be effective in accumulating in tumors in vivo. The GRP receptor (GRPr), also named bombesin receptor subtype 2, is a G-protein coupled seven-transmembrane receptor (Jensen et al. 2008). GRPr proteins have been shown to be highly overexpressed in several human tumors, including prostate cancer (Reubi et al. 2002). Futhermore, bombesin receptor antagonists have been shown to be preferable to agonists for tumor imaging, since they show high tumor uptake and long tumor washout (Cescato et al. 2008) as well as reduced physiologic activity. Despite the variety of bombesin compounds synthesized and evaluated, none have been systematically evaluated in patients with prostate cancer.

Anti-1-amino-3-^{18}F-fluorocyclobutane-1-carboxylic acid (^{18}F-FACBC) is a synthetic non-metabolized amino acid PET radiotracer which has been shown to accumulate in PCa (Schuster et al. 2007). In a study including 21 patients with histologically confirmed prostate cancer (Turkbey et al. 2013), ^{18}F-FACBC was shown to have standardized update values (SUV) of prostate tumors that did not differ significantly from SUV of BPH. Schuster et al. (Schuster et al. 2013) demonstrated a statistically significant correlation of SUV with the Gleason score. Unfortunately, only 11 patients were included in the study (Schuster et al. 2013). Thus, larger prospective clinical trials are still needed to evaluate the role of ^{18}F-FACBC PET/CT in prostate cancer detection and characterization.

3. AIMS OF THE STUDY

The general aims of this thesis were a) to develop and validate a novel MRI protocol for men with a clinical suspicion of prostate cancer, and b) to evaluate the applicability of novel PET tracers for imaging of primary prostate cancer. The specific aims of the sub-studies were as follows:

1. To evaluate ^{68}Ga-labeled bombesin analog (BAY86-7548) in patients with histologically confirmed prostate cancer

2. To develop and validate a novel MRI protocol suitable for men with a clinical suspicion of prostate cancer and no previous biopsy

3. To evaluate different mathematical models for DWI of prostate cancer in terms of fitting quality and repeatability

4. To evaluate a spin-lock imaging method for the detection and characterization of primary prostate cancer

5. To evaluate a spin-lock imaging and DWI post-processing method for the detection and characterization of primary prostate cancer

6. To evaluate biparametric MRI and targeted biopsy in men with a clinical suspicion of prostate cancer

7. To evaluate the potential of ^{18}F-FACBC PET/CT, PET/MRI and multiparametric MRI in the detection and characterization of primary prostate cancer.

4. MATERIAL AND METHODS

4.1. Study population

Patients with histologically confirmed prostate cancer, diagnosed through systematic TRUS-guided biopsies, were enrolled in studies I, III, IV, VI and VII. Studies II and VI included men with a clinical suspicion of prostate cancer based on elevated PSA (studies II and VI) and/or abnormal DRE (study IV)

Patients with histologically confirmed prostate cancer were prospectively enrolled in studies I, III, IV, VI and VII. The exclusion criteria were as follows: i) history of serious cardiovascular, liver or kidney disease; ii) uncontrolled serious infection; iii) contraindications for MRI (e.g. cardiac pacemaker, intracranial clips etc.); and iv) patient preference for active surveillance as a method of prostate cancer management. None of the patients who underwent imaging in Turku, Finland, in studies I, III and V received any hormonal or radiation therapy before PET/CT or MRI, except for one patient in study III who started gonadotropin releasing hormone antagonist (Degarelix, Ferring Pharmaceuticals, Parsippany, New Jersey, USA) treatment 10 days before the MRI examination. One patient with biochemical recurrence included in study I, imaged at the University Hospital of Zurich, was in androgen-resistant phase after pelvic radiotherapy, several local palliative radiotherapies and antiandrogenic therapy.

The inclusion criteria for study II were as follows: i) elevated PSA (>4.0 ng/ml) on two consecutive measurements in the last 6 months, and ii) normal DRE. The exclusion criteria were: (i) abnormal DRE; (ii) previous prostate biopsy; (iii) diagnosis of prostate cancer; (iv) previous prostate surgery (e.g. transurethral resection of the prostate); (v) active or chronic prostatitis; and (vi) contraindication for MRI examination (e.g. pacemaker, intracranial clips etc.).

Men with a clinical suspicion of prostate cancer (two repeated measurements of PSA in the range 2.5–20.0 ng/ml and/or abnormal DRE) were prospectively enrolled as part of study VI. The exclusion criteria were similar to those of study II, except for normal DRE and history of previous prostate biopsy.

In studies II, IV, V, VI and VII, all enrolled patients/men received a stool softener (Laxoberon ®) the day before and on the day of the PET/CT or MRI examination. If rectal gas was detected at the start of the MRI examination, the patient was sent to the toilet, after which the examination was restarted from scratch.

The clinical trial registration numbers for studies VI and VII are NCT01864135 and NCT02002455, respectively.

4.2. Synthesis of BAY86-7548

The precursor DOTA-4-amino-1-carboxymethylpiperidine-D-Phe-Gln-Trp-Ala-Val-Gly-His-Sta-Leu-NH2 (BAY86-7547) was obtained from Bayer HealthCare Pharmaceuticals (Berlin, Germany). All other reagents were purchased from commercial suppliers and were either synthetic or analytical grade.

Radiosynthesis was performed with a fully automated synthesis device (Modular Lab, Eckert & Ziegler Eurotope GmbH, Berlin, Germany) for 13 patients who had PET imaging performed at the Turku PET center, Turku, Finland. ^{68}Ga was obtained from a

$^{68}Ge/^{68}Ga$ generator (IGG-100, 50 mCi (1850 MBq), Eckert & Ziegler Isotope Products, Valencia, CA, USA) by eluting the generator with 7 mL of 0.1 M HCl. The radioactive fraction of the ^{68}Ga eluate (1.6 mL) was collected and HEPES-buffered BAY86-7547 (28 µg, 17 nmol) was added. The reaction mixture was incubated at 100−120°C for 12.5 min followed by SepPak purification and sterile filtration. The product was formulated with a sterile phosphate-buffered saline (PBS). The identity and radiochemical purity of the product (BAY86-7548) were evaluated by radio-HPLC. The identity was confirmed by comparing the retention times of the peaks obtained from BAY86-7548 and BAY86-7547. The in-vitro stability of BAY86-7548 was tested in formulation solution (PBS) by incubating for 2 h at room temperature followed by radio-HPLC analysis.

The radiosynthesis for one patient with biochemical recurrence images from Zurich was comparable to that in Turku, except for the ^{68}Ga eluate, which in Zurich was trapped onto a cation-exchange cartridge (Strata X C, Phenomenex). Then, 0.4 mL of 98% acetone/0.02 M HCl was used to elute ^{68}Ga from the cartridge. The peptide BAY86-7547 (28 µg, 17 nmol) and uric acid were dissolved in 2 mL 0.2 M sodium acetate buffer and prefilled into the reaction vessel. This was followed by incubation of the reaction mixture at 95°C for 6 min 40 s and formulation and in-vitro stability testing in saline instead of PBS.

4.3. Synthesis of ^{18}F-FACBC

The synthesis of ^{18}F-FACBC was performed using a FASTlab™ Synthesizer (GE Healthcare) as the production module and FASTlab cassettes and synthesis sequence designed for 18F-FACBC production. The cassettes and other raw materials were supplied by GE Healthcare.

4.4. PET/CT

PET was performed in studies I and VII. The patients were imaged in the supine position using a Discovery VCT PET/CT scanner (General Electric Medical Systems, Milwaukee, WI, USA) in study I, or a Discovery 690 PET/CT scanner (General Electric Medical Systems, Milwaukee, US) in study VII. One patient with biochemical recurrence included in study I who underwent PET/CT at the University Hospital of Zurich was imaged using a ST16 PET/CT Scanner (General Electric Medical Systems, Milwaukee, WI, USA). A low-dose CT protocol was performed and used for attenuation correction as well.

The measured PET data were corrected for dead time, decay and photon attenuation and reconstructed into a 256×256 matrix (study I) or a 128×128 matrix with voxel size 5.47×5.47×3.27 mm^3 (study VII). Image reconstruction followed a fully 3D VUE Point GE algorithm incorporating all quantitative corrections for detector dead time, radioactivity decay, photon, random and scatter attenuation. The reconstructed images were filtered using a 6 mm Gaussian post-filter.

In study I, a urethral catheter was used in nine (82%, 9/11) patients to limit accumulation of BAY86-7548 in the urinary bladder. A median dose of 147 MBq (range, 108−161 MBq) of BAY86-7548 was injected as a bolus into the antecubital vein. The patients' vital signs, including a 12-lead electrocardiogram, were monitored during imaging, and blood and urine chemistry was done before and after PET/CT acquisition. Dynamic PET acquisition was performed immediately following tracer

injection over the pelvic area for 60 min in 10 patients. Following this, a static whole-body emission scan (seven bed positions, 420 s per bed position) covering the whole torso in the caudal-to-cephalic direction was acquired 69±3 min after tracer injection in 10 patients. Six of these 10 patients also had a second static PET of the pelvic area (one bed position of 420 s duration) 102±7 min after tracer injection. Patients with biochemical recurrence—two at Turku University Hospital and three at the University Hospital of Zurich—received a whole-body PET scan starting 58–60 min from injection.

In study V, patients received an intravenous injection of 369±10 MBq (mean±standard deviation) of ^{18}F-FACBC diluted in 3–5 ml of saline as a 30-s bolus which was promptly flushed with saline. Emission imaging was started immediately after intravenous bolus injection. Following 20 min of dynamic data collection using a list-mode acquisition, additional table positions covering the whole pelvis and abdomen were imaged with a 4-min duration for each position. The dynamic data were reconstructed to 5 frames with a frame time of 4 min.

4.5. PET/MRI

The Ingenuity TF PET/MRI scanner (Phillips Medical Systems, Cleveland, Ohio, US) was used in studies III, IV, V, and VII. Only in study VII PET acquisition was done using the PET/MRI scanner. MR-based attenuation correction (MRAC) was performed using a vendor-provided method (Schulz et al. 2011).

The anatomical MR acquisition (atMR) for MRAC obtained using TR/TE 4.0/2.3 ms was converted into attenuation correction maps containing air and lung soft tissue. In PET image reconstruction, detector dead time, radioactivity decay, random scatter and photon attenuation corrections were applied and PET images were reconstructed in a 144×144 matrix with an isotropic voxel size of 4.0 mm. Image reconstruction followed a fully 3-D maximum-likelihood ordered subsets expectation maximum (LM-OSEM) algorithm with 3 iterations and 33 subsets using TOF technology.

RF excitation was performed using a two-channel volume whole-body RF coil with a manufacturer's 32-channel cardiac coil as the receiver coil. During protocol development, the 32-channel cardiac coil was compared with the TorsoXL coil (Figure 16) and found to give better signal-to-noise ratios.

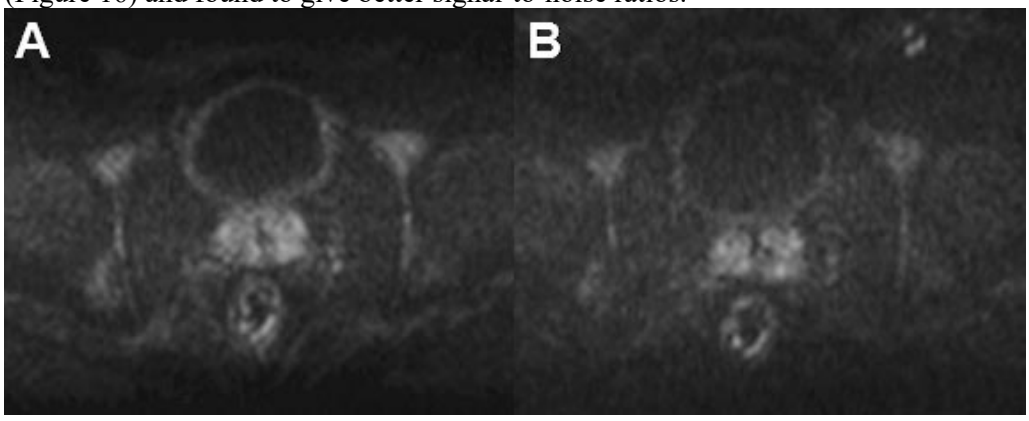

Figure 16. The trace DWI b=2000 s/mm^2 image acquired with a 32-channel cardiac coil (A) demonstrated higher signal-to-noise ratios than the TorsoXL coil (B).

T2-weighted images were obtained using a single-shot Turbo Spin Echo (TSE) sequence with repetition time/echo time (TR/TE) 4668/130 ms, field of view (FOV) 250×320 mm^2, acquisition matrix size 250×320, reconstruction matrix size 512×672, slice thickness 2.5 mm, no intersection gaps, SENSitivity Encoding (SENSE) factor 2 (Pruessmann et al. 1999), partial Fourier factor 0.6, and acquisition time 1 min 10 s. A single-shot spin-echo based sequence with monopolar diffusion gradient scheme (Figure 8) and echo-planar readout was used for DWI data acquisition in two separate acquisitions: 14 (low b value set) and 12 (high b value set) b values. The low b value set was acquired using the following parameters: TR/TE 1394/44 ms, FOV 250×250 mm^2, acquisition matrix size 124×124, reconstruction matrix size 256×256, slice thickness 5.0 mm, no intersection gaps, SENSE factor 2 (Pruessmann et al. 1999), partial-Fourier acquisition 0.69, diffusion gradient timing (Δ) 21.204 ms, diffusion gradient duration (δ) 6.6 ms, diffusion gradients applied in three directions (gradient overplus option on), SPectral Attenuated Inversion Recovery (SPAIR) fat suppression, number of signal averages for each b value 2, b values 0, 2, 4, 6, 9, 12, 14, 18, 23, 28, 50, 100, 300 and 500 s/mm^2, and acquisition time 3 min 45 s. The high b value set was acquired using the following parameters: TR/TE 3141/51 ms, FOV 250×250 mm^2, acquisition matrix size 100×99, reconstruction matrix size 224×224, slice thickness 5.0 mm, 0.5 mm intersection gaps, SENSE factor 2 (Pruessmann et al. 1999), partial-Fourier acquisition 0.69, diffusion gradient timing (Δ) 24.5 ms, diffusion gradient duration (δ) 12.6 ms, diffusion gradients applied in three directions (gradient overplus option on), SPAIR fat suppression, b values (number of signal averages) 0 (2), 100 (2), 300 (2), 500 (2) (2), 700 (2), 900 (2), 1100 (2), 1300 (2), 1500 (2), 1700 (3), 1900 (4) and 2000 (4) s/mm^2, and acquisition time 8 min 48 s. In addition to DWI, second-order rotating frame (RAFF) imaging (Liimatainen et al. 2010) was used with pulse train durations of 0, 45 and 90 ms and 500 Hz ($\gamma B_1/2\pi$) RF peak amplitude, which corresponds to 11.74 μT (B_1). As a readout, a 3D T1-FFE sequence was used with the following parameters: repetition TR/TE 4.0/2.3 ms, FOV 250×250 mm^2, acquisition matrix size 168×144, reconstruction matrix size 384×384, slice thickness 5.0 mm, no intersection gaps, number of slices six, flip angle 20 degrees, TFE factor 10, partial Fourier factor 0.625, SENSE (28) factor 2, centric k-space coding and RAFF pulse interval 3000 ms. The acquisition time for RAFF was 5 min 51 s. Thus, the readout consisted of 20 low flip angle excitations with TR 4.1 ms, centric coding, and repetition time for the RAFF pulse (the weighting pulse) of 3000 ms. T_2 relaxation values were measured using a GraSE sequence with TR/TEs of 686/20, 40, 60, 80 and 100 ms, FOV 230×183 mm^2, acquisition matrix size 256×163, reconstruction matrix size 512×400, slice thickness 5.0 mm, no intersection gaps, and acquisition time 1 min 35 s. Finally, single-shot T2w imaging and DWI (performed using b values of 0 and 800 s/mm^2) covering the whole pelvis were obtained.

In study III (patients with histologically confirmed prostate cancer), DWI data acquired using a high b value set were used.

4.5. Spin locking

To evaluate short-term repeatability, patients underwent two repeated MR examinations. After the first, a patient was taken out of the MR bore and asked to rest

for 10–15 minutes. After re-positioning of the patient on the MR table, the second MR examination was performed consisting of RAFF and cw $T_{1\rho}$ imaging. T_2 mapping and T2wi were not performed at the second examination. In study IV, spin-locking methods (T_{RAFF} and $T_{1\rho cw}$) were performed using a 3D T_1-FFE sequence with the following parameters: TR/TE 3.2/1.5 ms, FOV 375×375 mm^2, acquisition matrix size 152×122, reconstruction matrix size 320×320, slice thickness 5.0 mm, centric k-space coding, partial Fourier factor of 0.625, SENSE (Pruessmann et al. 1999) factor 2 and pulse interval 3000 ms. The pulse train duration for RAFF was 0, 45, and 90 ms and a cw RF pulse of 0, 20 and 80 ms duration was applied for $T_{1\rho cw}$. The same 500 Hz RF peak amplitude of weighting pulses was used for RAFF and $T_{1\rho cw}$. Specifically, a second-order rotating frame (RAFF2) was used in the current study (Liimatainen et al. 2014). The acquisition time for each of the different weighting pulse durations was 1 min 33 s.

In study V, RAFF was used (Liimatainen et al. 2010) with pulse train durations of 0, 45 and 90 ms and 500 Hz ($\gamma B_1/2\pi$) RF peak amplitude, which corresponds to 11.74 μT (B_1). The readout was done using a 3D T_1-FFE sequence with the following parameters: TR/TE 4.0/2.3 ms, FOV 250×250 mm^2, acquisition matrix size 168×144, reconstruction matrix size 384×384, slice thickness 5.0 mm, number of slices six, flip angle 20 degrees, TFE factor 10, centric k-space coding, partial Fourier factor 0.625, SENSE (Pruessmann et al. 1999) factor 2 and RAFF pulse interval 3000 ms. The RAFF acquisition time was 5 min 51 s.

4.6. Multiparametric and biparametric MRI

The MRI examinations in studies II, III (healthy volunteers), VI, and VII (mpMRI acquisition) were performed using a 3 T Verio (Siemens Healthcare, Erlangen, Germany) MR scanner and surface array. No endorectal coil was used.

In study III, DWI of healthy volunteers (study III) was performed using a spin-echo based double refocused echo-planar imaging sequence with bipolar gradient mode and the following parameters: TR/TE 7000/87 ms, FOV 260×260 mm^2, acquisition matrix size 128×128, reconstruction matrix size 128×128, slice thickness 5 mm, generalized autocalibrating partially parallel acquisitions (GRAPPA) (Griswold et al. 2002) factor 2, diffusion gradients applied in three optimized directions (3-Scan trace option on), number of signal averages (NSA) 2, 16 b values of 0, 50, 100, 200, 350, 500, 650, 800, 950, 1100, 1250, 1400, 1550, 1700, 1850 and 2000 s/mm^2, acquisition time 11 min 6 s. In addition to DWI, transversal T2-weighted images with a turbo spin-echo sequence were obtained with the following parameters: TR/TE 7430/104 ms, FOV 200×200 mm^2, acquisition and reconstruction matrix size 256×256, slice thickness 3 mm.

In study II, an identical MR protocol was used at two institutions (Turku, Finland and Bratislava, Slovakia) and consisted of triplanar T2-weighted imaging, single acquisition for DWI, ^{1}H-MRS and DCE-MRI. Before MRI examination, 1.0 mg of glucagon (GlucaGen, Novo Nordisk, Bagsværd, Denmark) was given subcutaneously to suppress bowel peristalsis. Anatomical triplanar T2-weighted imaging was performed using a TSE sequence with TR/TE 6400-8640/101 ms, FOV 200×200 mm^2, matrix size 320×320, slice thickness 3 mm, NSA 2 and acquisition

times 2 min 16 s (transverse images), 2 min 30 s (sagittal images) and 2 min 47 s (coronal images). A single-shot spin-echo based double refocused sequence with bipolar gradients was used for DWI data acquisition with TR/TE 5543/80 ms, FOV 260×260 mm^2, matrix size 128×128, slice thickness 3 mm, NSA 4, bandwidth 1184Hz/pixel acquiring 6/8 (75%) of k-space in the phase-encoding direction, b values 0, 100, 200 350 and 500 s/mm^2, GRAPPA (Griswold et al. 2002) factor 2 and 32 reference lines, acquisition time 5 min 10 s. In study V, additional DWI "multi b value high DWI data sets" were collected as follows: TR/TE 7000/87 ms, FOV 260×260 mm^2, matrix size 128×128, slice thickness 5 mm, no intersection gaps, bandwidth 1628 Hz/pixel acquiring 6/8 (75%) of the k-space in the phase-encoding direction (partial-Fourier acquisition), b values 0, 50, 100, 200, 350, 500, 650, 800, 950, 1100, 1250, 1400, 1550, 1700, 1850 and 2000 s/mm^2, two signal averages, GRAPPA factor 2 and 24 reference lines for auto-calibration, acquisition time 11 min 6 s.

The three-dimensional ^{1}H-MRS covering the whole prostate was performed using a PRESS sequence. Automatic and manual shimming of the whole prostate volume was performed (to optimize the main magnetic field homogeneity) in every patient. Weighted averaging with NSA 6 of elliptically sampled k-space, Hanning filtering of the signal and zero-filling to a 16×16 matrix was performed before Fourier transformation (Scheenen et al. 2004). The TR and TE were optimized for the shape of citrate resonance (Scheenen et al. 2005; Scheenen et al. 2007). Additional water and lipid signal from adjacent tissues was suppressed with seven outer volume saturation slabs. The following additional imaging parameters were used: acquisition bandwidth 1300 Hz, 512 spectra data points, FOV 96×96×96 mm^2 and matrix size 12×12×12 resulting in a nominal voxel size of 8×8×8 mm^3. A real voxel size could best be approximated as a sphere with a volume of 1.51 cm^3 and diameter of 14.24 mm after apodization (Scheenen et al. 2004) due to use of weighted averaging and Hanning filtering. The acquisition time was about 15–20 minutes including manual shimming. Axial dynamic contrast enhanced images were acquired before, during and after injection of the contrast agent. The contrast agent (0.1 mmol/kg Dotarem, Guerbet, France) was injected 30 s after the start of the sequence through a peripheral vein at a rate of 2 ml/s via a mechanical injector (Spectris, Medrad, Indianola, USA). In total, 60 time points at a temporal resolution of 6.9 s were acquired using a three-dimensional VIBE sequence (Rofsky et al. 1999) with the following parameters: TR/TE 5.43/1.87 s, 15 degree flip angle, FOV 240×240 mm^2, matrix size 192×192, slice thickness 3 mm, bandwidth 260Hz/pixel acquiring 6/8 (75%) of k-space in the phase-encoding direction, GRAPPA (Griswold et al. 2002) factor 2 with 24 reference lines, acquisition time 6.9 s per frame. Before the contrast-enhanced MR imaging, images with five different flip angles of 2, 5, 8, 10, and 15 degrees were obtained for calculation of the pre-contrast longitudinal relaxation time (T_{10}) (Wang et al. 1987).

In study VI, identical transversal T2-weighted images and DWI with b values of 0, 100, 200 350 and 500 s/mm^2 were acquired. Furthermore, two separated DWI data sets were collected using b values of 0–1500 mm^2 and 0–2000 mm^2 with the following parameters: TR/TE 5000/87 ms, FOV 260×260 mm^2, matrix size 128×128, slice thickness 5 mm, no intersection gaps, bandwidth 1628 Hz/pixel acquiring 6/8 (75%) of the k-space in the phase-encoding direction (partial-Fourier acquisition) and two signal averages, GRAPPA factor 2 and 24 reference lines for auto-calibration, acquisition time 1 min 37 s for each b value set.

The total duration of the MRI examination (including shimming and calibration) performed using the 3 T Verio MR scanner (Siemens Healthcare, Erlangen, Germany) in studies II, III, VI, and VII was about 60, 20, 15, and 90 minutes, respectively (Table 3).

Table 3. Summary of MRI data acquired using a 3 T Verio (Siemens Healthcare, Erlangen, Germany) MR scanner in studies II, III, VI, VII

	Study II	**Study III**	**Study VI**	**Study VII**
T2w - transversal	Yes	Yes	Yes	Yes
T2w - sagittal	Yes	Yes	Yes	Yes
T2w - coronal	Yes	No	No	No
DWI - 5b, 0-500 s/mm^2	Yes	No	Yes	Yes
DWI - 2b, 0-1500 s/mm^2	No	No	Yes	Yes
DWI - 2b, 0-2000 s/mm^2	No	No	Yes	Yes
DWI - 16b, 0-2000 s/mm^2	No	Yes	No	Yes
DCE-MRI	Yes	No	No	Yes
^{1}H-MRS	Yes	No	No	Yes
Overall duration [min]	60	20	15	90

4.7. Visual and quantitative evaluation of PET/CT (studies I, VII)

In studies I and V, PET/CT images in Turku were interpreted either by the consensus of two readers (JK, IJ, study I) or by one reader (JK, study V). In both studies, the readers were only aware that patients were diagnosed with prostate cancer or had a suspicion of cancer recurrence, and the readers were unaware of clinical and histopathological findings.

To evaluate the accuracy of PET/CT in the detection of prostate cancer, a region-based analysis was used (Figure 17). The prostate gland was divided on the superior-inferior axis into three parts, each of which was further divided into four areas/quadrants (anterior, posterior, left, right). The presence of prostate cancer on PET/CT images was defined as any mono- or multifocal uptake greater than the adjacent background within the CT-defined prostate gland and detectable in more than one slice (Jambor et al. 2012). Moreover, in study I a lesion-based analysis was performed in which each abnormal focus was correlated with prostatectomy findings to define its histopathological nature. Finally, regions of interest (ROIs) were placed on visually identified abnormal foci as well as areas defined as BPH and normal prostate tissue based on histopathological findings from whole-mount prostatectomy samples. The maximum standardized uptake value (SUV_{max}) was determined in all ROIs. Only tumors with the largest diameter of more than 0.5 cm, including all dominant tumors, were analyzed.

In study V, Logan plots (Logan 2000) using a reference ROI in the iliac/femoral artery were used to estimate the distribution volume, V_T, assuming that transport of ^{18}F-FACBC into cells is similar to receptor binding kinetics (Turkbey et al. 2013). Logan plots without plasma sampling, using a reference tissue, can be expressed as:

$$\frac{\int_0^T C_t(t)dt}{C_t(T)} = V_T \frac{\int_0^T C_R(t)dt}{C_t(T)} + Int' \qquad \text{Eq. 13}$$

where C_R is the reference tissue activity curve (ROI in iliac/femoral artery) and C_t is the target tissue activity curve. Thus, the slope of the linear phase equals DVR.

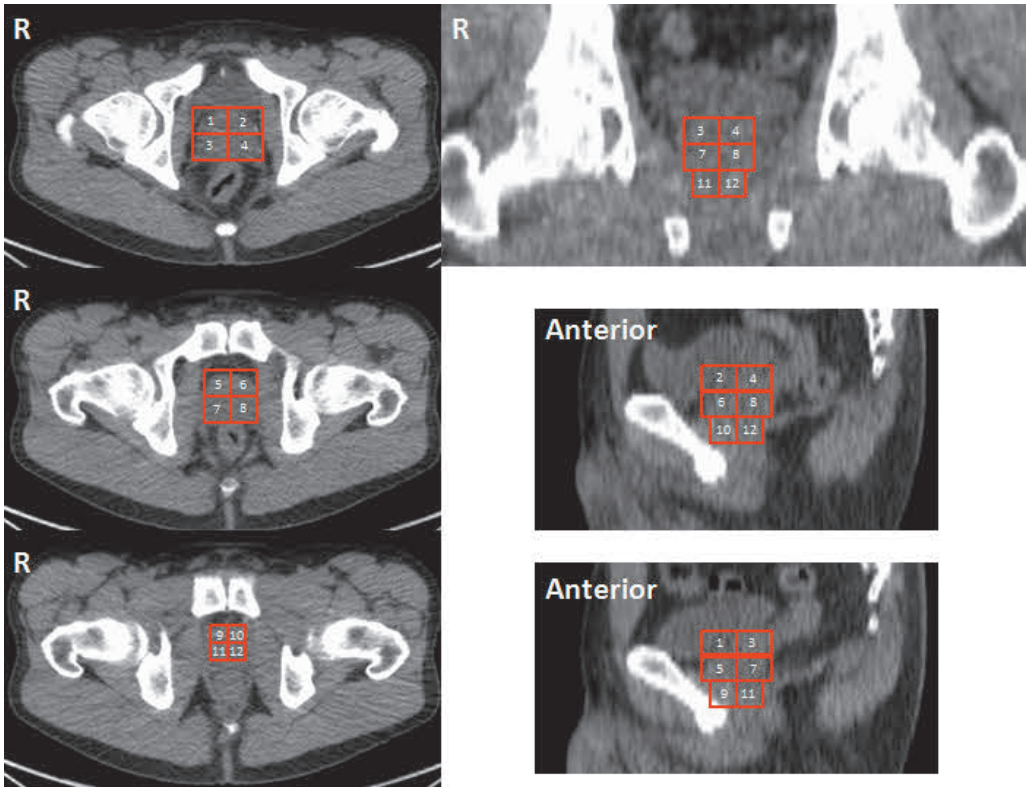

Figure 17. Location of regions of interest in studies I and V.

4.8. Evaluation of mpMRI (study II)

All imaging data sets were reported prospectively using a dedicated reporting system developed before the start of the study. Anatomical T2-weighted images and DCE-MRI, a raw dynamic contrast-enhanced T1-weighted and parametric map of the volume transfer constant (K^{trans}), were evaluated visually and a quantitative approach was used for DWI and ^{1}H-MRS. Multiple circular ROIs of size 21 mm^2 were drawn on ADC maps. The findings of each imaging sequence were interpreted using a standardized five-grade scoring system (Tables 4, 5, 6, 7), which was dichotomized with prostate cancer representing grade 4 and/or 5. If a lesion was considered grade 4/5 on at least two imaging sequences, it was considered to represent prostate cancer and was targeted for biopsy.

Table 4. Study I reporting system for T2-weighted images

T2w - Peripheral zone
1. Homogeneous high SI
2. Linear area perpendicular to the prostate capsule
3. Area of lower SI, not well demarcated
4. Discrete homogeneous low SI nodular lesion
5. Discrete homogeneous low SI nodular lesion with mass effect
T2w - Central/transitional zone
1. Spherical lesion with well-defined margins and heterogeneous signal intensity
2. Spherical or non-spherical lesion with well-defined margins, heterogeneous SI
3. Spherical lesion with well-defined margins, homogeneous low SI
4. Lenticular or ill-defined lesion with low SI
5. Lenticular or ill-defined lesion with low SI and mass effect

Table 5. Study I reporting system for DWI

DWI - Peripheral zone
1. Above 1450 mm^2/s
2. 1450 – 1350 mm^2/s
3. 1350 – 1250 mm^2/s
4. 1250 – 1150 mm^2/s
5. Below 1150 mm^2/s
DWI - Central/transitional zone
1. Above 1300 mm^2/s
2. 1300 – 1200 mm^2/s
3. 1200 – 1100 mm^2/s
4. 1100 – 1000 mm^2/s
5. Below 1000 mm^2/s

Table 6. Study I reporting system for ^{1}H-MRS

^{1}H-MRS - Peripheral zone
1. Cho+Cr/Cit below 0.22
2. Cho+Cr/Cit 0.22 – 0.34
3. Cho+Cr/Cit 0.34 – 0.46
4. Cho+Cr/Cit 0.46 – 0.58
5. Cho+Cr/Cit above 0.58
DWI - Central/transitional zone
1. Cho+Cr/Cit below 0.34
2. Cho+Cr/Cit 0.34 – 0.48
3. Cho+Cr/Cit 0.48 – 0.62
4. Cho+Cr/Cit 0.62 – 0.76
5. Cho+Cr/Cit above 0.76

Table 7. Study I reporting system for DCE-MRI

DCE-MRI - Peripheral zone
1. No enhancement, area with type 1 curve
2. Homogeneous area with type 2 curve
3. Discrete lesion with type 2 curve
4. Nodular lesion with type 3 curve
5. Nodular, mass-like lesion with type 3 curve
DCE-MRI - Central/transitional zone
1. No enhancement, area with type 1 curve
2. Spherical or non-spherical lesion with type 2 curve
3. Spherical lesion with well-defined margins and type 2 or 3 curve
4. Lenticular or non-spherical lesion with type 3 curve
4. Lenticular or non-spherical lesion with type 3 curve
5. Lenticular or non-spherical lesion with mass effect and type 3 curve

DCE-MRI = dynamic contrast-enhanced MRI, type 1 DCE-MRI curve: persistent enhancement; type 2 DCE-MRI curve: early fast enhancement followed by a plateau phase, signal intensity remains constant with less than 10% change from peak enhancement; type 3 DCE-MRI curve: early fast enhancement followed by washout, signal intensity decreases by more than 10% from peak enhancement.

For evaluation of diagnostic performance sensitivity, specificity, accuracy, and AUC, the presence of prostate cancer was estimated in six ROIs, or sextants (Figure 18). The results of systematic biopsy, MRI targeted biopsy and TRUS-lesion targeted biopsy were used as ground truth.

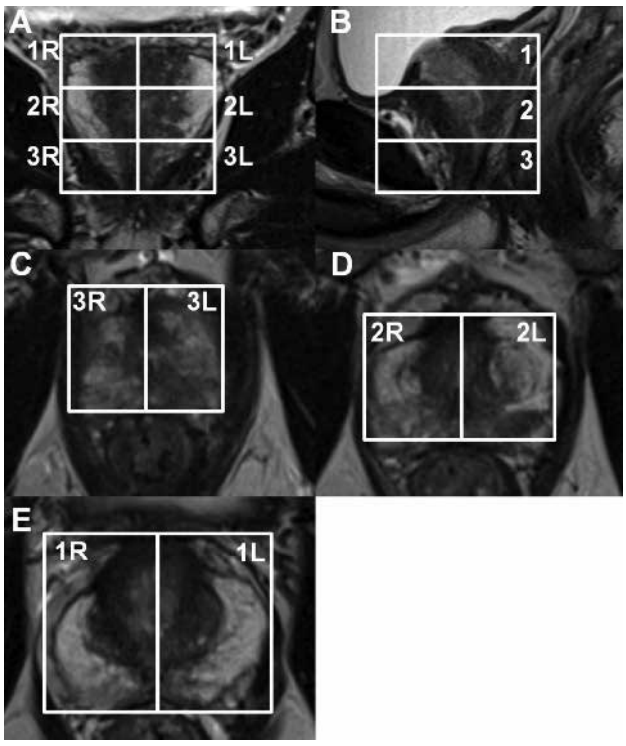

Figure 18. ROI reporting scheme use in study II. Coronal (A), sagittal (B) and axial (C, D, E) T2-weighted images demonstrate the presence of a low signal intensity (mass-like) lesion in the peripheral zone in sextants 3L (C) and 2L (D).

4.9. DWI data analysis (studies III, V, VII)

4.9.1. DWI modeling

ROIs were drawn on trace diffusion images of b=0 s/mm^2 following the use of an averaging filter with a kernel size of 3×3 as applied in study III. No filtering of trace diffusion images was applied in study V. In healthy volunteers (study III), two ROIs (square of 6.0×6.0×5.0mm^3, 9 voxels) were placed in the PZ, and two ROIs of the same size in the central gland on two consecutive slices, resulting in four ROIs in the PZ and four in the CZ. In addition, the PZ and CZ were manually segmented in each of the two consecutive slices, resulting in one ROI covering the whole PZ and another covering the whole CZ on each slice. The T2-weighted images were used as reference. In total, six and six ROIs contained PZ and CZ tissue, respectively. In patients with histologically confirmed prostate cancer (studies III, V), one square-shaped ROI (5.6×5.6×5.0mm^3, 25 voxels) was placed in the center of the prostate cancer area, and a same sized ROI on the contralateral side not containing prostate cancer, using whole-mount prostatectomy sections and T2-weighted images as the reference standard. The mean signal intensity (SI) of each ROI was fitted using four mathematical models (Eq. 6, 7, 8, 10). The fitting procedure was performed using the lsqnonlin MATLAB algorithm (Mathworks Inc., Natick, MA, USA) with multiple initialization (values in parentheses):

1. Mono-exponential model: ADC_m from 1.0 (0.1) μm^2/ms to 3.0 (3.0) μm^2/ms with step size 0.005 (0.01) μm^2/ms.
2. Stretched exponential model: ADC_s from 1.0 (0.1) μm^2/ms to 3.0 (3.0) μm^2/ms with step size 0.01 (0.02) μm^2/ms; α from 0.1 (0.1) to 1.0 (1.0) with step size 0.05 (0.05).
3. Kurtosis model: ADC_k from 1.0 (0.1) μm^2/ms to 3.0 (3.0) μm^2/ms with step size 0.01 (0.02) μm^2/ms; K from 0.0 (0.0) to 2.0 (2.0) with step size 0.1 (0.1).
4. Biexponential model for high b values (0–2000 s/mm^2): D_f from 1.0 (1.0) μm^2/ms to 7.0 (9.0) μm^2/ms with step size 0.1 (0.2) μm^2/ms; D_s from 0.0 (0.0) μm^2/ms to 2.0 (4.0) μm^2/ms with step size 0.01 (0.02) μm^2/ms; and f from 0.2 (0.2) to 1.0 (1.0) with step size 0.1 (0.1).

In study V, the IVIM model was fitted in two steps. In the first step, the monoexponential equation was used to derive the D_f parameter, which in the second step was inserted into the biexponential equation and the remaining three parameters (S_0, D_p, f) fitted (Kim et al. 2012; Luciani et al. 2008). The following multiple initialization values were used to limit the possible effect of local minima in the fitting procedure: D_p from 0.1 μm^2/ms to 25.0 μm^2/ms with step size 1.0 μm^2/ms; D_f 0.01 μm^2/ms to 3.5 μm^2/ms with step size 0.1 μm^2/ms; and f from 0.001 to 0.25 with step size 10% of the previous value.

4.9.2. Statistical evaluation of the models

Mathematical models for clinical data need to be evaluated in several respects: 1. How well does the model fit the data? 2. What is the repeatability of the fitted parameters? 3. How robust are the fitted parameters against measurement noise? 4. How much clinically useful information do the parameters provide?

How well the model fits the data can be evaluated using the sum of squares (residuals of the optimization fitting function). However, a polynomial function with

n-1 parameters can give a perfect fit to n data points. Thus, the use of sum of squares as the only measure of fitting quality is inappropriate, and the model complexity (number of free parameters) should be considered in model selection.

The Akaike Information Criterium (AIC) is a commonly used method for model comparison, but it is not a null hypothesis test (Burnham and Anderson, 2004):

$$AIC = N\ln\left(\frac{SS}{n}\right) + 2k \qquad \text{Eq. 14.}$$

where N is the number of data points (b values in DWI data sets), SS is the sum of squares of the vertical distance of the points from the fitted curve, and k is the number of free fitted parameters.

Derivation of the AIC formula is based on information theory (Burnham and Anderson, 1998).

The value of the AIC is on a relative scale, thus it is essential to compute and present the AIC differences:

$$\Delta AIC = N\ln\left(\frac{SS_B}{SS_A}\right) + 2(P_B - P_A) \qquad \text{Eq. 15}$$

where N is the number of data points (b values), P is the number of parameters, SS is the sum of squares of the vertical distance of the points from the fitted curve, and the A and B subscripts represent the simpler and more complex models, respectively. ΔAIC provides numerical information on the amount of information provided by the models in comparison to each other.

To compensate for the number of data points, N (b values in the DWI data set), when the number of parameters, P, is comparable to the number of data points, the corrected AIC difference (ΔAIC_c) is calculated according to the following equation:

$$\Delta AIC_c = N\left(\ln(\frac{SS_B}{N}) - \ln\left(\frac{SS_A}{N}\right)\right) + 2(P_B - P_A) + 2\left(\frac{P_B(P_B+1)}{N-P_B-1} - \frac{P_A(P_A+1)}{N-P_A-1}\right) \qquad \text{Eq. 16}$$

where N is the sample size, P is the number of parameters, SS is the sum of squares of the vertical distance of the points from the fitted curve, and the A and B subscripts represent the simpler and more complex models, respectively.

Another method for comparing the information content of the model is the F ratio (F):

$$F = \frac{(SS_A - SS_B)/SS_B}{(DF_A - DF_B)/DF_B} \qquad \text{Eq. 17}$$

where SS is the sum of squares of the vertical distance of the points from the fitted curve, DF (number of data points – number of parameters) is the degree of freedom, and the A and B subscripts represent the simpler and more complex models, respectively.

Only the AIC is suited both for nested and non-nested models. The F test tends to choose a more complex or simpler model compared with AIC, depending on the selected statistical significance value. Moreover, AIC was recommended to be used over the Bayesian information criterion (BIC) by Burnham and Anderson (Burnham and Anderson, 2004).

4.9.3. Simulation studies

Simulation studies were performed to further test the dependence of the model selection (ΔAIC, ΔAIC_c, F ratio) and fitted parameters on the signal-to-noise ratio (SNR). Signal decay curves were generated using the biexponential model, and the parameter values of f, D_f and D_s were 0.76, 2.65 and 0.55 $\mu m^2/ms$, respectively. Rician noise, consisting of two components of Gaussian noise with the same standard deviation (SD), was added to the simulated signal intensity curves:

$$r(b) = \sqrt{\left[SI(b) + n_1(b)\right]^2 + n_2(b)^2} \qquad \text{Eq. 18}$$

where r is the total signal intensity value, SI(b) is the simulated signal at a particular b value, b is the b value, and n_1 and n_2 are the two noise components. Signal intensity values were simulated 100 times. The coefficient of variation was calculated as the standard deviation of the fitted parameters divided by the mean.

4.9.4. Evaluation of reliability and repeatability

Several methods to evaluate reliability and repeatability have been proposed. The intraclass correlation coefficient (ICC) is a unitless statistical measure (Shrout & Fleiss1979). Shrout and Fleiss (Shrout & Fleiss1979) introduced several different ICC methods which address different statistical problems. In study III, ICC(3,1) was used, which evaluates the reliability and repeatability of individual measurement, in contrast to ICC(3,k) (Jambor et al. 2014), which evaluates the overall reliability and repeatability of all repeated measurements. In general, ICC(3,1) values are lower compared with ICC(3,k):

$$ICC(3,1) = \frac{BMS - EMS}{BMS + (k-1)EMS} \qquad \text{Eq. 19}$$

where BMS is the between-subjects mean square, EMS is the residual mean square, and k is measurement (four different measurements).

Thus, differences between repeated measurements were compared to the differences between patients. Higher ICC(3,1) values imply better reliability and repeatability, while values below zero mean that the random error as a source of variation is greater than the actual investigated target variable. Ninety-five percent confidence intervals for ICC(3,1) and CR were calculated using 100 000 bootstrap samples.

4.10. Evaluation of biparametric MRI (study VI)

A system for reporting bpMRI was developed before initiation of the trial. Suspicious lesions on bpMRI were reported using a Likert scoring system as follows: 1 - significant cancer is highly unlikely to be present; 2 - significant cancer is unlikely to be present; 3 - significant cancer is equivocal; 4 - significant cancer is likely to be present; 5 - significant cancer is highly likely to be present. The Likert score was based on the combined evaluation of T2w, apparent diffusion coefficient (ADC) maps, trace DWI images acquired using a b value of 1500 s/mm^2, and trace DWI images acquired using a b value of 2000 s/mm^2. The final Likert score was not based on an arithmetical combination of ratings for each method (T2w, DWI), but on the overall

probability of a lesion being malignant or not. A restricted signal on trace DWI images acquired using b values of 1500 s/mm^2 and/or 2000 s/mm^2 was carefully distinguished from susceptibility artifacts caused by an inhomogeneous B_0 field (e.g. rectal gas). BPH can have a high signal intensity on trace b values of 1500 s/mm^2 and/or 2000 s/mm^2 and low ADC values. However, BPH typically has well-defined margins with a fibrotic capsule having a low signal and heterogeneous signal intensity on T2w. The Likert score is an "overall impression score" of a lesion being a significant cancer or not. All equivocal-to-suspicious (Likert score 3–5) lesions were reported with a clear indication of the dominant lesion based on the highest Likert score followed by the largest lesion diameter and lowest ADC values. After defining the dominant lesion, the prediction of its Gleason score was classified into three categories (non-probable, probable and highly probable) based on the measurement of the lowest mean ADC value of the lesion. Prediction of a lesion's Gleason score was based on the ADC map and trace DWI images acquired using b values of 1500 s/mm^2 and 2000 s/mm^2. ADC maps calculated using five b values in the range 0–500 s/mm^2 were used in the dominant Gleason grade 4 prediction:

1. Probable:
- high signal intensity is present on trace DWI images acquired using b values of 1500 s/mm^2 and 2000 s/mm^2 and ADC values are below 850×10^{-6} mm^2/s

2. Highly probable:
- high signal intensity is present on trace DWI images acquired using b values of 1500 s/mm^2 and 2000 s/mm^2 and ADC values are 750×10^{-6} mm^2/s.

Regardless of the number of possible lesions, only the dominant lesion was targeted with two cores.

4.10.1. Biparametric MRI in men with clinical suspicion of prostate cancer – study endpoints

The primary endpoint of study VI was diagnostic accuracy of the combination of bpMRI with clinical variables for the detection of prostate cancer and clinically significant prostate cancer. The models and available variables are as follows: 1) Basic model: PSA, age, use of 5-alpha-reductase inhibitors (≥3 months and within 6 months from accrual); 2) Visit model: PSA, age, use of 5-alpha-reductase inhibitors, DRE; 3) TRUS model: PSA, age, use of 5-alpha-reductase inhibitors, DRE, TRUS findings, prostate volume (as measured by TRUS), dPSA; 4) MRI model: PSA, age, use of 5-alpha-reductase inhibitors, DRE, TRUS findings, prostate volume, dPSA, bpMRI Likert score (See Appendix: MRI reporting system); 5) MRI model including diffusion-weighted imaging (DWI): PSA, age, use of 5-alpha-reductase inhibitors, DRE, TRUS findings, prostate volume (as defined by TRUS), dPSA, bpMRI Likert score, DWI score (See Appendix: MRI reporting system).

The DWI score (categorical variables: non-probable, probable, highly probable) for Gleason score prediction is based on DWI data sets collected using 5 b values in the range 0–500 s/mm^2. In addition, all the models were estimated with and without free PSA as well. DRE and TRUS were analyzed as binary variables—either suspicious or normal.

The secondary endpoints were: 1) Detection rates of prostate cancer, clinically significant prostate cancer, and clinically insignificant prostate cancer in the Likert

score groups; 2) Detection rates of prostate cancer, clinically significant prostate cancer, and clinically insignificant prostate cancer using targeted and systematic biopsy.

4.11. Biopsy procedures (studies II and VI)

TRUS-guided biopsies in studies II and VI were performed with a standard clinically available TRUS system. In study II, the mpMRI report was reviewed after systematic TRUS-guided biopsy. Thus, the performing urologist was not aware of the mpMRI target(s) at the time of biopsy. Suspicious lesions noted on TRUS (abnormal echogenicity) and not in the region sampled by systematic biopsy were targeted and sampled (two patients). In both studies, cognitive targeting was used without MRI-TRUS fusion. In study II, a maximum of two cores per target were taken. Small discrete lesions (largest diameter 7–9 mm on mpMRI) were targeted with one core per lesion. In study VI, only the dominant lesion with a Likert score of 3–5 was targeted with two biopsy cores followed by systematic TRUS-guided biopsy. Finally, two biopsy cores for biomarker research were taken as part of study IV. Systematic TRUS-guided biopsy consisted of 12 cores, one medial and one lateral core taken from each third of each prostate lobe (Taneja2006). Depending on the biopsy findings, prostate cancer treatment options (active surveillance, radiotherapy, and radical prostatectomy) were discussed with each patient as appropriate.

4.12. Histopathologic analysis

Histological slides were analyzed by at least one experienced pathologist. Whole-mount prostatectomy sections were prepared as follows: the prostate glands were fixed in 10% buffered formalin for 24−48 hours. After fixation the surfaces of the prostate gland, left, right and anterior, were inked with different colors to preserve the orientation of the prostate gland. Whole-mount axial macro-sections were obtained at 6–8 mm intervals transversely in a plane perpendicular to the long axis of the prostate gland in the superior-inferior direction. The most apical macro-section was sectioned in the coronal orientation for easier evaluation of the capsular status of the inferior region. The first transversal section at the base was further sectioned in the sagittal orientation for easier evaluation of the margin and seminal vesicles. 4 μm whole-mount sections from each macro-section were stained with hematoxylin and eosin. The presence and location of cancer foci, high-grade prostate intraepithelial neoplasm, prostatitis, BPH, capsular status and seminal vesicle invasion were determined. The Gleason score was assigned as a combination of primary, secondary, and tertiary Gleason grade according to the 2005 International Society of Urological Pathology Modified Gleason Grading System (Epstein et al. 2005). A tertiary Gleason grade was assigned in the presence of Gleason grade patter higher than the primary and secondary, where the tertiary component was estimated visually to account for less than 5% of the tumor (Epstein2010).

4.13. Clinically significant prostate cancer

Since no widely-accepted definition of cancer risk groups and clinically significant prostate cancer exists, analyses in this thesis work were performed using various definitions of clinically significant prostate cancer. In study II, clinically significant prostate cancer was defined as 3 mm or greater core prostate cancer length of Gleason score 3+3 or any Gleason grade 4 or 5 (Puech et al. 2013). Clinically significant prostate cancer in the prostatectomy specimen was defined as a Gleason grade 4 or 5 component, stage pT3 or tumor volume greater than 0.5 cm^3 (Hambrock et al. 2010).

Three definitions of clinically significant prostate cancer were used in study IV as follows: Definition 1 – Low risk (Filson et al. 2016): biopsy Gleason score 3+3, Intermediate risk: biopsy Gleason score 3+4, High risk: biopsy Gleason score 4+3 or higher; Definition 2 – Low risk (Siddiqui et al. 2015): biopsy Gleason score 3+3 and/or 3+4 with <50% of any core containing cancer and/or <4 systemic biopsy cores positive for cancer, Intermediate risk: Gleason score 3+4 with ≥50% of any core containing and/or ≥4 systemic biopsy cores positive for cancer, High risk: Gleason score 4+3 or higher; Definition 3 – Low risk (Ploussard et al. 2015): biopsy Gleason score 3+3 and/or 3+4, Intermediate risk: biopsy Gleason score 4+3, High risk: biopsy Gleason score 4+4 or higher. In the sub-analyses including only men undergoing radical prostatectomy, Definitions 1 and 3 used Gleason scores obtained from radical prostatectomy specimens instead of prostate biopsies. Definition 2, Intermediate risk, was modified as follows: Gleason score 3+4 and prostate cancer ≥20% of the whole prostate volume (Siddiqui et al. 2015). Clinically significant prostate cancer was defined as intermediate and high risk prostate cancer according to the definitions above.

4.14. Statistical methods

Continuous variables are described as means and standard deviations or medians and interquartile ranges, where appropriate. The Kolmogorov-Smirnov test was used to check the normality. Categorical variables are presented as frequencies and proportions.

In study II, at least two ratings of prostate cancer (grade 4/5 on the scoring system, see Tables 4–7) were need to assign the final rating of that combination of imaging sequences as indicative of prostate cancer. In addition, the AUC values were calculated using the added ratings of each individual sequence using a trapezoidal rule. AUC_{added} means AUC values calculated using the added ratings of each individual sequence; $AUC_{combined}$ represents values calculated using a combination of sequences (raters) with at least two positive ratings indicating prostate cancer. Sensitivity and specificity values of patient- and sextant-based analyses were compared using the McNemar test (Trajman & Luiz2008) and two-sided p-values were calculated.

In studies II and V, receiver operating characteristic curve (ROC) analysis was performed for patient- and sextant/region-based analyses using 60 000 to 100 000 bootstrap samples (Rutter2000) to account for within-patient correlations. AUC values of the operating characteristic curve (ROC) analysis were calculated using the trapezoid rule, compared using a method originally described by Hanley and McNeil

(Hanley & McNeil1983) and two-sided p-values were calculated. Bootstrap samples for ROC analysis were constructed by stratifying patients based on overall cancer level (prostate cancer present or not) and drawing patients as the independent units with replacement from these groups (prostate cancer present or not) in study II. Proportions of biopsy cores containing prostate cancer from systematic and targeted biopsy were compared using the Chi-Square test.

In studies I, III and V, the Kruskal-Wallis test was also used to compare the fitted parameter values of normal prostate and prostate cancer. P-values below 0.05 were considered statistically significant.

In study IV, the performance of 10 models for the prediction of prostate cancer and clinically significant prostate cancer was evaluated using logistic regression models. The AUC values were estimated using the logistic regression models and systematic, targeted biopsy as a “gold standard” (follow-up targeted biopsy findings in three men, Nos. 64, 95 and 119). These AUC values were used to evaluate the ability of the models to predict prostate cancer and clinically significant prostate cancer. Likert scores 1–2 were combined in the model predictions resulting in 3 degrees of freedom (Likert scores 1–2, 3, 4, 5). The DeLong test was used to determine if the differences between AUC values were statistically significant. The Chi-Square test was used to compare the proportion of low-, intermediate- and high-risk men among those upgraded based on targeted biopsy compared with systematic biopsy or vice versa. Correlation between the Likert score (4 degrees of freedom) and DWI score (2 degrees of freedom) was explored using the Spearman correlation coefficient. P-values less than 0.05 were considered statistically significant.

Statistical analyses were performed using in-house written MATLAB code (Mathworks Inc., Natick, MA, USA) and/or GraphPad Prism, version 5.00 (GraphPad Software, San Diego, USA) and/or R version 3.2.0 software (R Foundation for Statistical Computing, Vienna, Austria).

5. RESULTS

5.1. Population

In total, 11, 16, 55 and 163 men were included in the final analyses of studies I, II, III, IV and V, respectively (Table 8).

Table 8. Patient characteristics

	Study enrolment time	No. of patients	Age mean+SD / median (IQR)	PSA mean+SD / median (IQR)
I	12/2010 – 06/2011	11[#]	64 (62-66)	17.6±11.1
II	03/2013 – 02/2015	55*	65±6	7.4 (6.0–9.0)
III	11/2013 – 11/2013	16[$]	67 (62-68)	9.8 (9.2–14.5)
IV	03/2013 – 01/2014	36	63±6	11.6±7.5
V	04/2013 – 11/2014	50	64±6	11.1±7.3
VI	03/2013 – 02/2015	163*	65±6	7.7±2.3
VII	01/2014 – 07/2015	27	64±6	8.6 (66–16.0)

[#]Study I included five patients with biochemical recurrence.
[$]Study III included eight healthy volunteers of median age 54 years, ranging from 46 to 65 years.
*Studies II and VI included men with a clinical suspicion of prostate cancer.

No drug-related adverse events were associated with injections of BAY86-7548 and ^{18}F-FACBC. All patients tolerated the imaging procedure well.

In study I, the mean±standard deviation PSA level of patients with primary prostate cancer was 17.6±11.1 ng/mL (range 6.2–45.0), while the three patients with biochemical recurrence of prostate cancer had PSA levels of 0.36, 4.7 and 282 ng/mL, respectively. Based on histopathological analysis of whole-mount prostatectomy samples, 26 tumor foci were identified in 11 patients, with 19 (73%) of these foci larger than 0.5 cm.

In study II, 55 men were enrolled and included in the final analyses. Of these, 41 underwent mpMRI and biopsy at Turku University Hospital, Finland, and the other 14 patients at the St. Elisabeth Oncology Institute, Bratislava, Slovakia. All enrolled men underwent targeted and systematic biopsy and none of them withdrew from the study. In four men, ^{1}H-MRS was non-diagnostic due to the poor quality of spectra. In the remaining patients, the global shim-line full width at half maximum of the water peak was between 20 and 25 Hz over the complete 3D PRESS-selected volume of interest. In one man, DWI was non-diagnostic due to large susceptibility artifacts caused by rectal gas (poor B_0 field). The mpMRI reports for two men were not available before biopsy due to technical problems.

In study III, of 18 prostate cancer patients enrolled, two were excluded from the final analysis due to susceptibility artifacts related to rectal air (poor B_0 field).

In study IV, all enrolled patients were included in the final data.

In study V, 10 patients were excluded from the final data set due to gross movement during MR imaging and/or severe susceptibility artifacts due to rectal air.

In study VI, 175 men were prospectively enrolled and 14 were excluded, resulting in 161/175 (92%) being included in the final analyses. Free-to-total PSA (fPSA) values were not measured in 31/161 (19%) men whose total PSA values were

above 10.00 ng/ml (as per institutional laboratory policy). A total of 17 men with Likert scores of 3–5 and no prostate cancer found at systemic or targeted biopsy underwent follow-up bpMRI examinations. One of these men (No. 156) underwent two follow-up bpMRI examinations.

Study VII was halted in July 2015, since the interim analysis indicated that ^{18}F-FACBC was providing limited value to MRI/mpMRI. In total 32 patients were enrolled between December 2013 and July 2015, six of whom withdrew from the trial before imaging. The remaining 26 patients underwent ^{18}F-FACBC PET/CT followed by PET/MRI on the same day and mpMRI within a week. The time from tracer injection to mid-frame of the PET/MRI was 54 (median) and 50–69 (IQR) minutes.

5.2. Diagnostic accuracy of BAY86-7548 PET/CT (study I)

5.2.1. BAY86-7548 PET/CT in patients with primary prostate cancer

In the region-based analysis (Figure 13), 57 (43%) regions were identified as having a presence of prostate cancer based on whole-mount prostatectomy sections. Based on visual analysis of BAY86-7548 PET/CT findings, the sensitivity, specificity, and accuracy values for detection of prostate cancer were 89%, 81% and 83%, respectively. In lesion-based analysis a sensitivity of 79% was achieved. All dominant lesions were detected, except for one patient in whom a smaller peripheral zone tumor was found, but the larger anterior lesion could not be identified with certainty. Both lesions had the same Gleason score of 3+4.

In three patients (3/11, 27%) who underwent prostatectomy, metastatic lymph nodes were discovered. In total in 11 patients, 135 lymph nodes were removed and histopathologically analyzed with 10 showing the presence of metastatic prostate cancer. On a per-patient basis, the sensitivity of BAY86-7548 PET/CT was 67%. The size of the three BAY86-7548 PET/CT negative lymph node metastases was 6 mm (left iliac node), 5 mm and 5 mm (two right iliac lymph nodes), respectively.

The average±standard deviation SUV_{max} (60–70 min from injection time) for prostate cancer lesion was 6.6±4.7, and the values differed significantly ($p<0.05$) from the SUV_{max} of BPH (2.4±1.5) and normal tissue of the peripheral zone (1.3±1.0).

Prostate cancer was present in 15 (68%) autoradiography sections. In these sections, all prostate cancer lesions demonstrated positive binding. Furthermore, in two tissue sections BPH nodules and in one section a high-grade prostatic intraepithelial neoplasia (HGPIN) lesion had positive binding (Figure 19). An example of positive autoradiography binding for prostate cancer and HGPIN is shown in Figure 19.

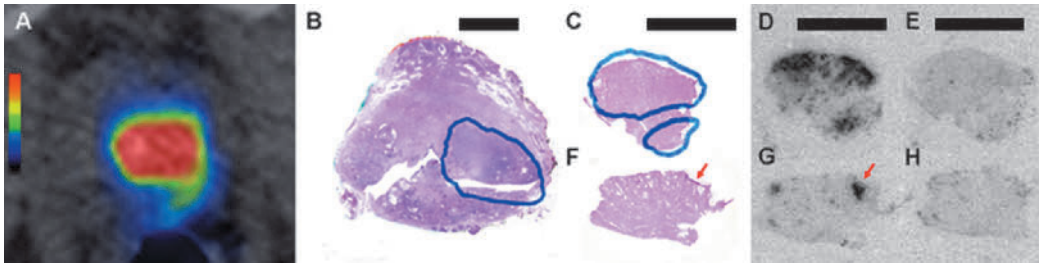

Figure 19. BAY86-7548 PET/CT (A) showing uptake in the left lobe of the prostate, in the area corresponding to prostate cancer based on a whole-mount prostatectomy sample (B, tumor outlined in blue). Autoradiography showed the presence of GRP receptors in the section taken from the left lobe (C) in the area of prostate cancer (D, tumor outlined in blue), while only small areas of HGPIN in the section taken from the right lobe had positive activity (E, F, red arrow indicates HGPIN area). Copyright ® AACR, reproduced with permission.

5.2.2. BAY86-7548 PET/CT in patients with biochemical recurrence

In the first hormone-naïve patients with biochemical recurrence who were scanned in Turku, BAY86-7548 PET/CT successfully detected the recurrence of prostate cancer. The findings of BAY86-7548 PET/CT were in concordance with ^{11}C-acetate PET/CT and 3T MRI in the prostate bed. In one patient, both ^{11}C-acetate PET/CT and DWI suggested the presence of metastatic parailiac lymph node involvement, while BAY86-7548 PET/CT did not show any pathological uptake in this region. The patient subsequently received external beam radiotherapy to the PET- and MRI-positive prostatic bed and parailiac nodes bilaterally. In a follow-up ^{11}C-acetate PET/CT scan performed 3 months after radiotherapy, the PSA value had fallen to 0.068 and the prostate bed no longer had measurable ^{11}C-acetate uptake, while that in the parailiac lymph node was still present. Based on CT images, this lymph node measured 6 mm and remained unchanged before and after radiotherapy despite the rapid drop in serum PSA.

In patient 13, the BAY86-7548 result was positive in one iliac and one mediastinal lymph node, both of which were similarly positive on ^{11}C-acetate. In addition, ^{11}C-acetate showed several positive lymph nodes in unconventional locations such as axillary, parasternal and inguinal regions. The patient imaged at the University Hospital of Zurich (No. 14) had multiple ^{18}F-fluorocholine-positive bone metastases but had no suspicious BAY86-7548 PET/CT findings.

5.3. mpMRI in men with a clinical suspicion of prostate cancer (study II)

5.3.1. Diagnostic accuracy of mpMRI in men with a clinical suspicion of prostate cancer

Prostate cancer was diagnosed in the cores of systematic or targeted biopsy in 37 (67%, 37/55) men, 33 (60%, 33/55) of whom had clinically significant prostate cancer. The detection sensitivity, specificity, accuracy and AUC values at the patient level for T2w, DWI, ^{1}H-MRS and DCE-MRI (score of 3–5 for at least two imaging sequences) for clinically significant prostate cancer were 90%, 52%, 75% and 0.71, respectively.

The corresponding values for T2wi and DWI, both indicative of prostate cancer, were 81%, 73%, 78% and 0.77, respectively (Tables 9 and 10).

Prostate cancer was diagnosed in 107 (32%, 107/330) sextants, with clinically significant prostate cancer present in 88 (27%, 88/330) of them. DWI had the highest accuracy (84%) and AUC (0.78) values for the detection of prostate cancer. Similarly to the patient level analysis, the use of T2w+DWI was more specific and less sensitive than the use of T2w+DWI+^{1}H-MRS+DCE-MRI. ^{1}H-MRS and its combinations with other demonstrated the highest specificity with low sensitivity as shown in Figure 20.

Table 9. Diagnostic accuracy at the patient level for a combination of imaged sequences (study II).

	Sensitivity	**Specificity**	**Accuracy**	**$AUC_{combined}$**	**AUC_{added}**
1 rater:					
T2w	90 (*)	40 (p<0.01)	70	0.66 (p=0.12)	0.66 (p=0.12)
DWI	84 (p=0.31)	72 (p=0.10)	79	0.79 (*)	0.79 (*)
DCE	81 (p=0.05)	45 (p<0.01)	67	0.64 (p=0.08)	0.64 (p=0.08)
MRS	33 (p<0.01)	95 (*)	59	0.64 (p=0.06)	0.64 (p=0.06)
2 raters:					
T2w+DWI	81 (p=0.99)	73 (p=0.02)	78	0.77 (p=0.79)	0.77 (p=0.73)
T2w+DCE	82 (*)	59 (p<0.01)	73	0.71 (p=0.29)	0.69 (p=0.18)
T2w+MRS	33 (p<0.01)	100 (*)	61	0.67 (p=0.07)	0.70 (p=0.24)
DWI+DCE	71 (p=0.08)	86 (p=0.08)	78	0.79 (*)	0.76 (p=0.67)
DWI+MRS	33 (p=0.01)	100 (NA)	61	0.67 (p=0.07)	0.79 (*)
DCE+MRS	30 (p<0.01)	100 (NA)	58	0.65 (p=0.04)	0.68 (p=0.15)
3 raters:					
T2w+DWI+ DCE	90 (*)	50 (p<0.01)	74	0.70 (p=0.26)	0.77 (p=0.61)
T2w+DWI+ MRS	80 (p=0.08)	76 (p=0.15)	78	0.78 (p=0.86)	0.82 (*)
T2w+DCE+ MRS	83 (p=0.15)	57 (p=0.01)	73	0.70 (p=0.27)	0.74 (p=0.30)
DWI+DCE+MRS	73 (p=0.03)	86 (*)	78	0.79 (*)	0.81 (p=0.91)
4 raters:					
T2wi+DWI+DCE+MRS	90	52	75	0.71	0.79

Sensitivity, specificity and accuracy values are displayed in %. In each group, two-sided p-values are displayed for the combination marked (*). $AUC_{combined}$ = at least two positive ratings indicative of prostate cancer (at least grade 4–5 of the five-grade scoring system) must be present in the same location to have a positive rating for prostate cancer as the final statement of a particular combination; AUC_{added} = AUC calculated using added ratings of sequences; T2w = anatomical T2-weighted imaging, DCE = dynamic contrast enhanced MRI, DWI = diffusion-weighted imaging, MRS = proton magnetic resonance spectroscopy, NA = not applicable

Table 10. Diagnostic accuracy at the sextant level (study II).

	sensitivity	specificity	accuracy	$AUC_{combined}$	AUC_{added}
1 rater:					
T2w	70 (*)	80 (p<0.01)	78	0.75 (p=0.18)	0.75 (p=0.18)
DWI	68 (p=0.78)	95 (p=0.05)	88	0.82 (*)	0.82 (*)
DCE	67 (p=0.40)	86 (p<0.01)	81	0.77 (p=0.21)	0.77 (p=0.21)
MRS	29 (p<0.01)	98 (*)	80	0.64 (p<0.01)	0.64 (p<0.01)
2 raters:					
T2w+DWI	61 (*)	96 (p<0.01)	87	0.79 (*)	0.83 (p=0.90)
T2w+DCE	61 (p=0.76)	92 (p<0.01)	84	0.77 (p=0.54)	0.80 (p=0.44)
T2w+MRS	27 (p<0.01)	99 (*)	81	0.64 (p<0.01)	0.78 (p=0.27)
DWI+DCE	58 (p=0.31)	97 (p<0.01)	86	0.77 (p=0.68)	0.83 (*)
DWI+MRS	29 (p<0.01)	99 (NA)	81	0.64 (p<0.01)	0.82 (p=0.68)
DCE+MRS	26 (p<0.01)	99 (NA)	81	0.63 (p<0.01)	0.79 (p=0.23)
3 raters:					
T2w+DWI+DCE	70 (*)	89 (p<0.01)	85	0.80 (*)	0.84 (p=0.92)
T2w+DWI+MRS	63 (p<0.01)	96 (p=0.06)	88	0.79 (p=0.86)	0.83 (p=0.94)
T2w+DCE+MRS	65 (p<0.01)	91 (p<0.01)	84	0.78 (p=0.49)	0.81 (p=0.74)
DWI+DCE+MRS	60 (p<0.01)	97 (*)	87	0.78 (p=0.61)	0.84 (*)
4 raters:					
T2w+DWI+DCE+MRS	72	89	85	0.81	0.84

Sensitivity, specificity and accuracy values are displayed in %. In each group, two-sided p-values are displayed for the combination marked (*). $AUC_{combined}$ = at least two positive ratings indicative of prostate cancer (at least grade 4–5 of the five-grade scoring system) must be present in the same location to have a positive rating for prostate cancer as the final statement of a particular combination; AUC_{added} = AUC calculated using added ratings of sequences; T2w = anatomical T2-weighted imaging, DCE = dynamic contrast-enhanced MRI, DWI = diffusion-weighted imaging, MRS = proton magnetic resonance spectroscopy, NA = not applicable

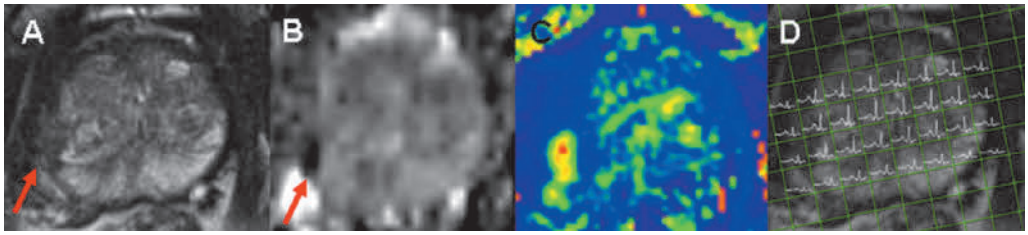

Figure 20. Imaging findings in a man with a PSA value of 14 ng/ml. An asymmetric, mass-like lesion was present on the T2-weighted images in the right-side peripheral zone (A: the red arrow indicates the lesion) with an ADC value (calculated from DWI data sets acquired using 5 b values in the range 0–500 s/mm^2) of 930 mm^2/s (B: the red arrow indicates the lesion) and increased K^{trans} values (C), all suggestive of prostate cancer. However, ^{1}H-MRS (D: metabolite map) was not suggestive of the presence of prostate cancer. Three cores of systematic biopsy (two cores with 5 mm Gleason score 3+4 and one core with 4 mm Gleason score 3+3) from the area of the MRI target were positive for prostate cancer, as were two targeted cores (5 and 2 mm prostate cancer with a Gleason score of 3+4). No remaining cores of systematic TRUS-guided biopsy were positive for prostate cancer. Copyright ® JMRI, reproduced with permission.

5.3.2. mpMRI targeted biopsy for detection of prostate cancer and clinically significant prostate cancer

Prostate cancer detection rates per patient for targeted biopsy and systematic biopsy in 53 patients were 63% (22/35) and 91% (32/35), respectively. The corresponding values for clinically significant prostate cancer were 68% (21/31) and 84% (26/31), respectively. No mpMRI target was present in three patients with clinically significant prostate cancer, and in one patient targeted biopsy revealed clinically insignificant prostate cancer (same Gleason score of 3+3 as for systemic biopsy), while prostate cancer in one systematic biopsy core contained 5 mm prostate cancer. Eleven men (20%, 18/53) could have been spared un unnecessary biopsy procedure, while missing only three men with clinically significant prostate cancer (Figure 21). The negative predictive value for clinically significant prostate cancer at the patient level was 79% (11/14).

The overall presence of prostate cancer in targeted biopsy cores (43%, 33/77) was significantly higher ($p<0.001$) than in systematic biopsy cores (21%, 138/648). Clinically significant prostate cancer was found in 35% (27/77) of targeted biopsy cores and in only 13% (87/648) of systematic biopsy cores ($p<0.001$). The largest proportion of targeted biopsy cores (32 cores [42%, 32/77]) were targeted based on the findings present on T2wi+DCE-MRI+DWI, of which 13 (41%, 13/32) cores contained clinically significant prostate cancer (Table 11). The targeted cores based on the findings on T2wi+DWI contained most of the prostate cancer (85%, 28/33) and clinically significant prostate cancer (93%, 25/27) diagnosed by means of targeted cores (Table 10).

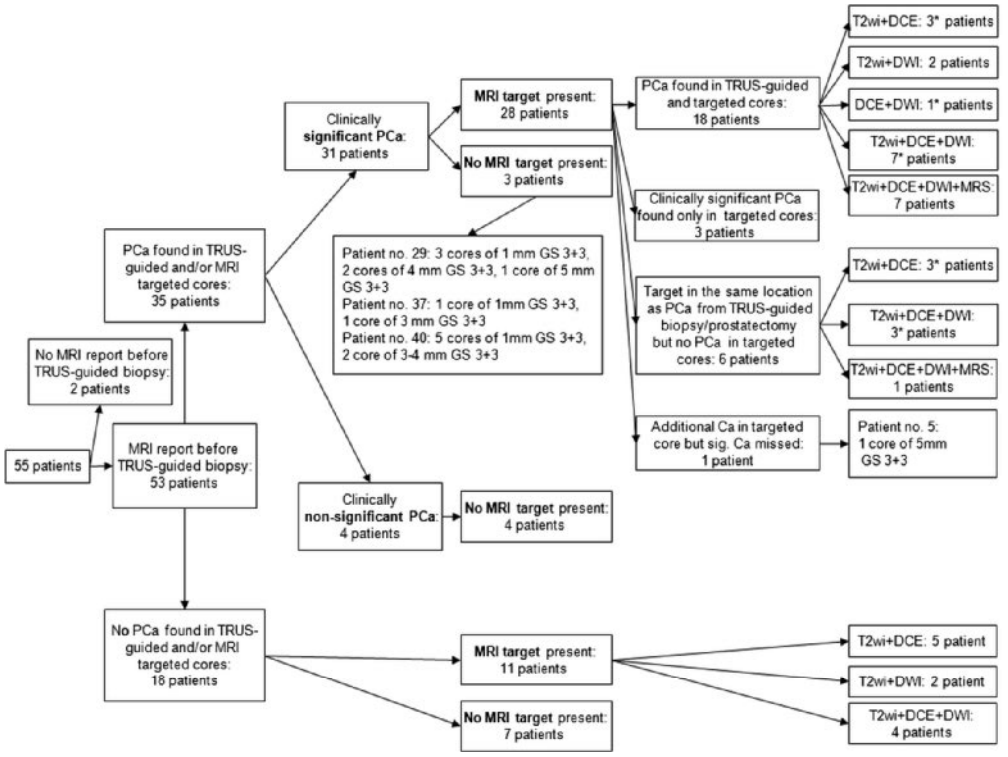

Figure 21. Patient flowchart. Clinically significant prostate cancer was defined as 3 mm or greater core prostate cancer length of Gleason score 3+3, or any Gleason grade 4/5. GS = Gleason score, PCa = prostate cancer, *three men had MRI targets based on different combinations of sequences. Copyright ® JMRI, reproduced with permission.

Table 11. Summary of biopsy results per core for systematic biopsy, MRI-targeted biopsy and TRUS-lesion guided biopsy

Biopsy type	No PCa	Clinically significant PCa
Systematic	510 (79%)	87 (13%)
MRI targeted	44 (57%)	27 (35%)
T2w+DCE	18 (78%)	2 (9%)
T2w+DWI	2 (50%)	1 (25%)
DCE+DWI	2 (100%)	0
T2w+DCE+DWI	17 (53%)	13 (41%)
T2w+DCE+DWI+MRS	5 (31%)	11 (69%)
TRUS targeted	22 (50%)	19 (43%)

T2w = T2-weighted imaging, DCE = dynamic contrast enhanced MRI, DWI = diffusion-weighted imaging, MRS = proton magnetic resonance spectroscopy, § = in all patients TRUS lesion-based biopsy was performed as a part of systematic biopsy except for two men who had one additional core.

5.4. DWI modeling (study III)

5.4.1. Parameter values and model preference

Statistically significant differences ($p<0.05$) were found between PZ vs central gland median values (DWI data of healthy volunteers) and normal prostate vs prostate cancer of ADC_m, ADC_s, ADC_k. Differences in K values reached statistical significance between normal prostate and prostate cancer tissue types. Median, skewness, kurtosis and 5–95 percentile values are summarized in Tables 12 and 13.

Table 12. Median [skewness, kurtosis] (5%–95% percentile) of fitted parameters in the PZ and central gland of healthy volunteers

	Healthy volunteers	
	Peripheral zone	**Central gland**
ADC_m (μm^2/ms)	1.77 [0.34, -0.76] (1.44–2.23)*	1.52 [0.10, 0.39] (1.28–1.72)*
ADC_s (μm^2/ms)	1.83 [0.25, -0.77] (1.47–2.29)*	1.56 [0.07, 0.42] (1.29–1.78)*
α	0.83 [0.27, 0.16] (0.75–0.92)	0.79 [0.05, 0.20] (0.75–0.85)
ADC_k (μm^2/ms)	2.19 [0.11, -0.54] (1.80–2.55)*	1.91 [0.09, 0.72] (1.66–2.17)*
K	0.59 [-0.54, -0.12] (0.39–0.71)	0.68 [0.78, 0.94] (0.60–0.82)
f	0.76 [-1.02, 1.61] (0.41–0.95)*	0.65 [-0.21, -0.24], (0.37–0.87)*
D_f (μm^2/ms)	2.64 [8.01, 66.61] (2.14–4.45)	2.78 [1.99, 5.43] (1.98–4.48)
D_s (μm^2/ms)	0.55 [0.62, 0.85] (0.04–1.12)	0.63 [-0.57, 0.60] (0.16–0.92)

* denotes significant differences in the median values of the PZ and central gland.

Table 13. Median [skewness, kurtosis] (5%-95% percentile) of fitted parameters in the PZ and central gland of prostate cancer patients

	Prostate cancer patients	
	Normal	**PCa**
ADC_m (μm^2/ms)	1.39 [0.16,-0.58] (1.08–1.72)¶	0.89 [0.73, -0.26] (0.70–1.38)¶
ADC_s (μm^2/ms)	1.45 [-0.10, -0.60] (1.11–1.82)¶	0.88 [0.75, -0.18] (0.66–1.47)¶
α	0.76 [-0.16, 1.40] (0.71–0.81)	0.74 [-0.39,0.05] (0.65–0.81)
ADC_k (μm^2/ms)	1.81 [-0.07, -0.43] (1.39–2.17)¶	1.25 [0.84, 0.19] (0.95–1.89)¶
K	0.73 [-0.09, 0.09] (0.62–0.85)¶	0.99 [0.17, -1.20] (0.79–1.27)¶
f	0.58 [-0.06, -0.01] (0.36–0.84)	0.43 [0.53, -0.28] (0.22–0.75)
D_f (μm^2/ms)	2.96 [1.34, 3.58] (2.11–4.39)	2.84 [1.19, 1.52] (1.78–5.32)
D_s (μm^2/ms)	0.62 [-1.36, 2.70] (0.19–0.83)	0.47 [-0.44, 0.93] (0.19–0.71)

¶ - marks significant differences in the median values of prostate cancer and normal tissue (Normal)

Biexponential, kurtosis and stretched exponential models were preferred based on ΔAIC, ΔAICc and the F ratio compared with the monoexponential model in all tissue types. In general, the kurtosis model was preferred over the stretched exponential model.

5.4.2. Reliability and repeatability of DWI derived parameters

Parameters of monoexponential, kurtosis, and stretched exponential (except for the α parameter) models had higher ICC(3,1) values than the parameters of the biexponential model, suggesting better reliability and repeatability of these parameters (Figure 22).

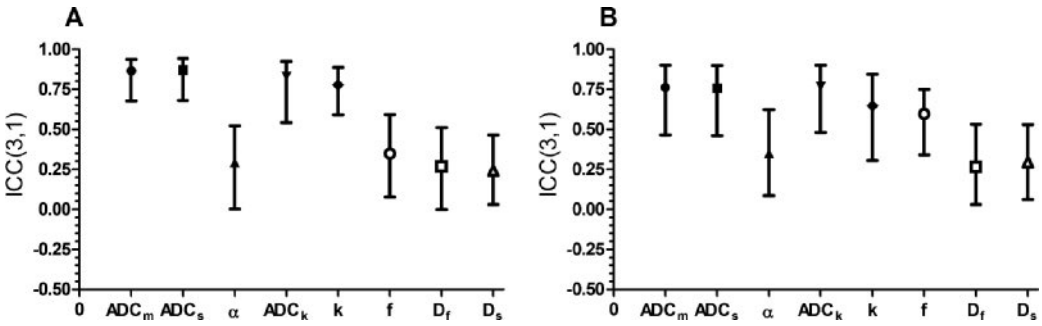

Figure 22. Intraclass correlation coefficient values, ICC(3,1), for all fitted parameters of prostate cancer (A) and normal tissue (B) of prostate cancer patients. The parameters of the biexponential model and α parameter of the stretched exponential model had lower ICC(3,1) values than the other parameters. The ICC(3,1) values are displayed with 95% confidence intervals shown as error bars. Copyright ® MRM, reproduced with permission.

5.4.3. Simulation studies

In simulation studies, the parameters of the biexponential model (f, D_f, D_s) were the least robust parameters against increasing noise due to large variation with increasing noise standard deviation (Figure 23).

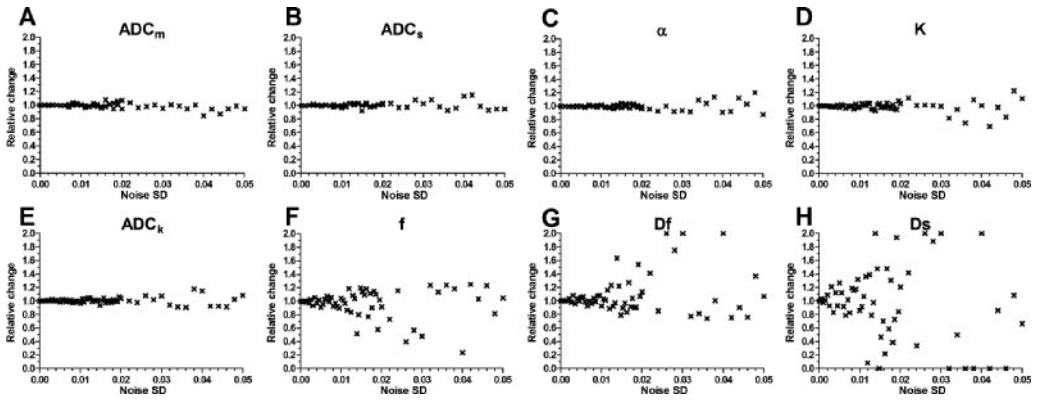

Figure 23. Relative changes of the fitted parameters (y-axis) as a function of the noise standard deviation (x-axis) of one simulated signal intensity curve. Each fitted parameter was divided by the parameter calculated without the presence of noise. The parameters of the biexponential model (F- f, G- D_f, H- D_s) had larger variation with increasing noise than did the monoexponential, stretched exponential and kurtosis models. The monoexponential model had the smallest variation with increasing noise SD. The relative changes in D_f and D_s parameters were constrained to 0.0–2.0 for visualization purposes. Copyright ® MRM, reproduced with permission.

The coefficients of variation were largest for the D_s parameter. The biexponential model was the preferred model based on AIC_c only at low noise levels, while the differences in AIC_c values became negligible with increasing noise standard deviation (Figure 24).

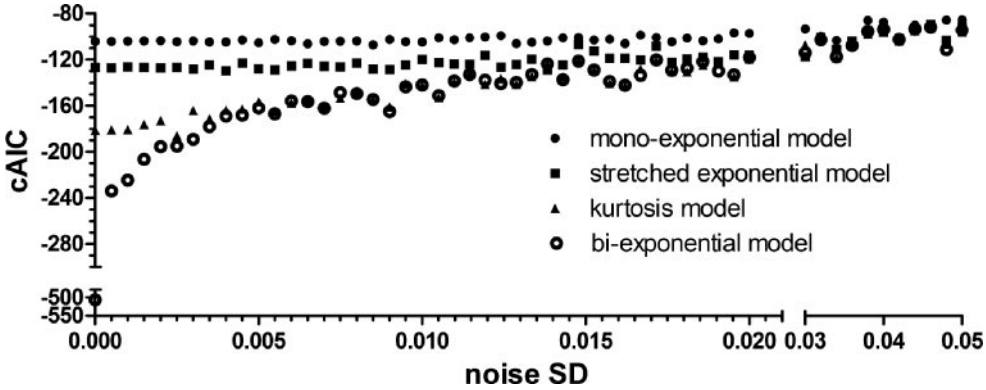

Figure 24. Corrected Akaike information criteria (cAIC) of one simulated curve (y-axis) as a function of increasing noise SD (x-axis). The biexponential model had the smallest cAIC values at low noise levels, while the differences compared with the other models started to be negligible at higher noise SD. This indicates that the biexponential model is the preferred model at low noise SD, but at higher noise SD the differences in cAIC are negligible. Copyright ® MRM, reproduced with permission.

Increasing noise of data fitted using a monoexponential function leads to a decrease of a fitted exponent. Adding infinite noise would lead to the median fitted value of an exponent approaching zero. Specifically, increasing noise leads to a smaller median ADC_m value of the monoexponential function. Simulations using noise standard deviation up to 0.5 are shown in Figure 21. As the figure shows, the median ADC_m (100 fits) value of the monoexponential function decreases with increasing noise.

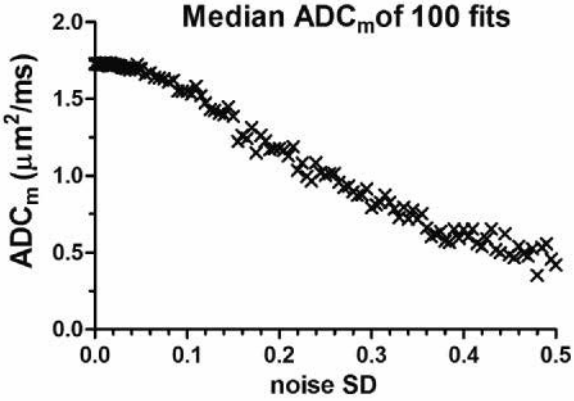

Figure 25. Median of 100 fitted curves as a function of noise standard deviation (SD).

5.5. Spin locking and DWI of prostate cancer (Study IV, V)

5.5.1. Repeatability of spin-locking methods and DWI

In study IV, both spin-locking related parameters T_{RAFF} and $T_{1\rho cw}$ demonstrated high repeatability with coefficients of repeatability as a percentage of the median value in the range 7.8–22.1% and with ICC(3,1) in the range 0.72–0.93.

In study V, T_{RAFF}, high b value DWI-derived parameters (ADC_{mh}, K, ADC_k), and T_2 (T_2) data sets demonstrated high repeatability with ICC(3,1) and CR as a percentage of the median value in the ranges 0.65–0.92% and 3.6–6.8%, respectively. In contrast, f and D_p parameters had substantially lower ICC(3,1) and high CR values. Specifically, ICC(3,1) and CR as a percentage of the median value were in the range −0.36–0.57% and 20.4–162.7% for f and D_p parameters, respectively. ADC_{ml} and D_f parameters, which are derived from low b set, had ICC(3,1) and CR as a percentage of the median value in the ranges 0.49–0.91% and 4.2–12.2%, respectively.

5.5.1. Prostate cancer detection and characterization of spin-locking methods and DWI

Similarly to study IV, in study V statistically significant differences ($p<0.001$) were present between T_{RAFF}, ADC_{ml}, D_f, ADC_{mh}, K, ADC_k, and T_2 values of PCa and PZ (Figure 26). Following Bonferroni correction (0.05/9), statistically significant differences between PCa and the central gland (CG) were present for T_{RAFF}, ADC_{ml}, D_f, ADC_{mh}, K, and ADC_k parameters (Figure 26). The differences between PZ and CG reached statistical significance ($p<0.05/9$) only for T_{RAFF} and T_2 parameters (Figure 27).

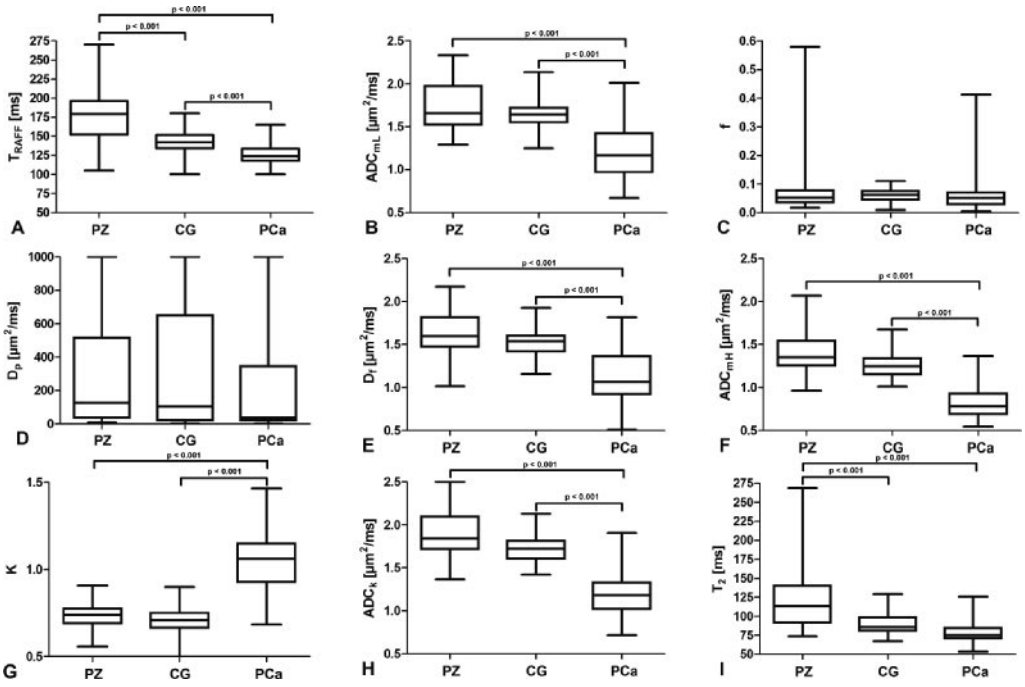

Figure 26. Box plots showing T_{RAFF} (A), ADC_{ml} (B), f (C), D_p (D), D_f (E), ADC_{mh} (F), K (G), ADC_k (H), and T_2 (I) relaxation time values of the PZ, CG, and PCa. The box extends from the 25th to the 75th percentiles, the error bars extend from minimal to maximal values, and the line in each box is the median value.

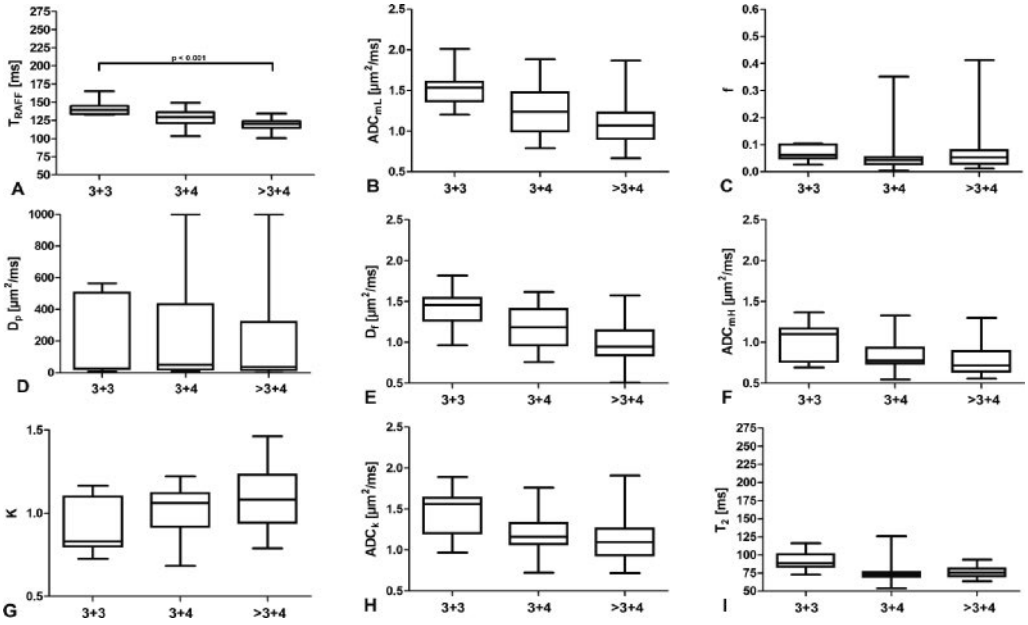

Figure 27. Box plots showing T_{RAFF} (A), ADC_{ml} (B), f (C), D_p (D), D_f (E), ADC_{mh} (F), K (G), ADC_k (H), and T_2 (I) relaxation time values of low (3+3, intermediate (3+4), and high (>3+4) Gleason score group tumors. *The box extends from the 25th to the 75th percentiles, the error bars extend from minimal to maximal values, and the line in each box is the median value.* Copyright ® MRM, reproduced with permission.

In studies IV and V, differences between tumors with Gleason score 3+3 vs >3+4 were statistically significant ($p<0.01$) only for T_{RAFF}, [in study V following Bonferroni correction ($p < 0.05/9$)]. Furthermore, the RAFF method outperformed DWI derived parameters and T_2 mapping in tumor classification based on AUC values (Table 14). The strongest correlations between the parameter values and Gleason score groups (n=3) were found for T_{RAFF}, ADC_{mL}, and D_f with the Spearman correlation coefficient (95% confidence interval) values of −0.65 (−0.79, −0.44), −0.47 (−0.66, −0.22), and −0.48 (−0.67, −0.22), respectively (Table 14).

Table 14. AUC values for Gleason score classification of prostate cancer tumors and Spearman correlation coefficient values.

	3+3 vs >3+3	Spearman
Parameter	**AUC (95% CI)**	**ρ**
T_{RAFF}	0.92 (0.82,0.98)	−0.65 (−0.79, −0.44)***
ADC_{ml}	0.85 (0.72,0.95)	−0.47 (−0.68, −0.21)***
ADC_{mlEx}	0.80 (0.62,0.95)	−0.48 (−0.69, −0.22)***
f	0.65 (0.51, 0.84)	0.01 (−0.26, 0.28)
D_p	0.53 (0.50, 0.78)	-0.02 (−0.31, 0.25)
D_f	0.80 (0.62, 0.95)	-0.48 (−0.69, −0.22)***
ADC_{mh}	0.76 (0.54, 0.96)	-0.36 (−0.61, −0.08)**
ADC_{mhEx}	0.75 (0.54, 0.96)	-0.36 (−0.62, −0.04)**
K	0.74 (0.52, 0.96)	0.32 (0.03, 0.57)*
ADC_k	0.75 (0.53, 0.95)	−0.33 (−0.57, −0.04)*
T_2	0.85 (0.67, 0.98)	−0.21 (−0.46, 0.10)

*p<0.05; ** p<0.01; *** p<0.001

5.5. bpMRI in men with a clinical suspicion of prostate cancer (study VI)

5.5.1. Imaging findings

Likert scores of 3–5 were assigned to 123/161 (76%) patients, of whom 92 had one lesion, 29 had two lesions, and two had three lesions detected at bpMRI. The DWI score (probability of a dominant Gleason grade 4) of the dominant lesion was non-probable in 44, probable in 31 and highly probable in 42 patients. In six patients the DWI score could not be assigned because of susceptibility artifacts. There was a good correlation between the Likert score and the DWI score (Spearman correlation coefficient 0.78, $p<0.001$). Free access to all data sets, including follow-up data sets, and the results of data analyses are available at the study server (http://petiv.utu.fi/improd).

5.5.2. Diagnostic accuracy

Incorporation of bpMRI findings into the diagnostic model significantly improved the prediction accuracy for prostate cancer and clinically significant prostate cancer, according to all three definitions, over clinical models without bpMRI findings.

The number of men with Likert scores of 1, 2, 3, 4 and 5 was 30 (19%), eight (5%), 24 (15%), 21 (13%) and 78 (48%), respectively (Table 15). Comparison of the Likert scores of 1–2 versus 3–5 for predicting the presence of prostate cancer gives an overall sensitivity of 93% and specificity of 55% for detecting prostate cancer. The sensitivity for detecting clinically significant prostate cancer according to definitions 1, 2 and 3 was 95%, 97% and 100% with a specificity of 44%, 40% and 30%, respectively. Depending on the definition of clinically significant prostate cancer, only zero to four men with clinically significant prostate cancer had a Likert score of 1–2 (Tables 4 and 5). By contrast, 78, 69, and 37 out of 99 men with a Likert score of 4–5 presented with clinically significant prostate cancer according to definition Nos. 1, 2, and 3, respectively, while 91 men had prostate cancer of any type. In 24 men with a Likert score of 3, only one clinically significant prostate cancer was found according to any of the three definitions.

Based on these results, reductions of 24% (38/161) and 39% (62/161) in the number of men undergoing biopsy would be achieved, and only 0–4 (0–2%) and 1–5 (0-3%) men with clinically significant prostate cancer would be missed when performing biopsy (targeted and systematic combined) only in men with Likert scores of 3–5 and 4–5, respectively.

Table 15. Prevalence of prostate cancer and clinically significant prostate cancer in different Likert score groups based on a cohort of 161 men. Significant prostate cancer.

	Likert score					
	1	**2**	**3**	**4**	**5**	**Total**
No Cancer	24 (15%)	6 (4%)	17 (11%)	4 (2%)	4 (2%)	55 (34%)
Gleason 3+3	4 (2%)	0 (0%)	6 (4%)	6 (4%)	7 (4%)	23 (14%)
Gleason 3+4	2 (1%)	2 (1%)	0 (0%)	7 (4%)	34 (21%)	45 (28%)
Gleason >3+4	0 (0%)	0 (0%)	1 (1%)	4 (2%)	33 (20%)	38 (24%)
Total	30 (19%)	8 (5%)	24 (15%)	21 (13%)	78 (48%)	161 (100%)

5.5.3. Comparison of targeted biopsy with systematic biopsy

According to all three definitions of clinically significant prostate cancer, significantly ($p<0.05$) more men were upgraded to an intermediate or high risk category based on targeted biopsy compared with systematic biopsy. Moreover, significantly ($p<0.05$) more men were diagnosed with low-risk prostate cancer according to all three definitions based on systematic biopsy compared with targeted biopsy.

In a sub-cohort of 123 men with a Likert score of 3–5, the addition of systematic biopsy to targeted biopsy resulted in an upgrade to the intermediate or high risk category in 8–12 (7-10%) men, while 8–10 (7-8%) men were diagnosed with clinically non-significant prostate cancer (depending on the definition of clinically significant prostate cancer). In this sub-cohort, significantly ($p<0.05$) more men were upgraded to the intermediate or high risk category based on targeted biopsy (25, 19, 16 men) than were upgraded based on systematic biopsy (five, 12 and four, respectively).

5.6. ^{18}F-FACBC PET/CT, PET/MRI and mpMRI in primary prostate cancer (study VII)

5.6.1. Diagnostic accuracy

^{18}F-FACBC PET/CT and PET/MRI identified lymph node metastasis in one patient which was histologically confirmed, but lymph node metastases were not detected preoperatively in five patients. The size of lymph node metastases not correctly identified on preoperative ^{18}F-FACBC PET/CT and PET/MRI was less than 7 mm.

In the region-based analysis, 164 (53%, 164/312) regions contained prostate cancer. ^{18}F-FACBC PET/CT demonstrated the highest sensitivity of 87% and lowest specificity of 56%. ^{18}F-FACBC PET/MRI had a significantly ($p<0.001$) higher specificity of 96% (Table 16). Both ^{18}F-FACBC PET/MRI and mpMRI significantly ($p<0.01$) outperformed ^{18}F-FACBC PET/CT in terms of AUC values, while no significant differences were present between ^{18}F-FACBC PET/MRI and mpMRI.

Table 16. Diagnostic accuracy at ROI level.

	Sensitivity	Specificity	Accuracy	AUC (95% CI)
PET/CT	87 (*)	56 (p<0.001)	72	0.72 (0.65–0.80) (p<0.001)
PET/MRI	84 (p=0.32)	96 (p=0.10)	90	0.90 (0.86–0.94) (*)
mpMRI	77 (p<0.01)	99 (*)	88	0.88 (0.83–0.93) (p=0.47)

5.6.1. Gleason score prediction

The predicative power (as evaluated by AUC and ρ values) of PET/CT was similar for SUV_{max} values measured on frames between 12 and 22 minutes, and substantially lower for SUV_{max} on PET/MRI (Table 17). Distribution volume values (calculated using Logan plots) had a significant positive correlation ($p<0.01$) with the Gleason

score. However, neither V_T values nor SUV_{max} demonstrated higher AUC or absolute ρ values than DWI-derived parameters. All DWI-derived parameter values had significant correlation ($p<0.05$ or $p<0.01$) with the Gleason score, except for f and D_p. In addition to DWI-derived parameters, T_{RAFF} values also demonstrated significant correlation with the Gleason score. By contrast, T_2, K^{trans} and Cho+Cr/Cit had low AUC values and non-significant ρ values.

Table 17. AUC values for Gleason score classification of prostate cancer tumors and Spearman correlation coefficient values. To differentiate between parameters estimated using different data sets, each parameter is assigned a b value range and number of b values, e.g. $ADC_{m\_0\_2000\_12b}$ – ADC_m of DWI data collected using 12 b values in the range 0–2000 s/mm^2.

	AUC (95% CI) 3+3 vs >3+3	**AUC(95% CI) 3+3, 3-4 vs >3+4**	**ρ (95% CI)**
DVR	0.76 (0.54 0.94)	0.76 (0.58 0.91)	0.48 (0.17 0.70)**
$SUV_{PET/CT}$	0.63 (0.38 0.86)	0.72 (0.54 0.88)	0.43 (0.11 0.67)*
$SUV_{PET/MRI}$	0.56 (0.32 0.78)	0.51 (0.32 0.71)	0.06 (−0.28 0.39)
$ADC_{m\_0\_2000\_12b}$	0.84 (0.59 0.99)	0.76 (0.58 0.90)	−0.53 (−0.74 −0.23)**
$ADC_{k\_0\_2000\_12b}$	0.77 (0.52 0.95)	0.67 (0.48 0.85)	−0.38 (−0.63 −0.04)*
$K_{\_0\_2000\_12b}$	0.92 (0.81 1.00)	0.84 (0.70 0.95)	0.68 (0.45 0.83) **
$ADC_{m\_0\_500\_14b}$	0.83 (0.58 1.00)	0.82 (0.67 0.94)	−0.60 (−0.78 −0.33)**
$f_{\_0\_500\_14b}$	0.51 (0.28 0.74)	0.55 (0.35 0.74)	−0.07 (-0.40 0.28)
$D_{p\_0\_500\_14b}$	0.57 (0.30 0.82)	0.53 (0.34 0.73)	0.08 (−0.26 0.41)
$D_{f\_0\_500\_14b}$	0.82 (0.57 0.99)	0.74 (0.56 0.90)	−0.50 (−0.72 −0.19)**
T_{RAFF}	0.82 (0.60 0.98)	0.73 (0.55 0.89)	−0.49 (−0.71 −0.18)**
T_2	0.67 (0.37 0.93)	0.61 (0.41 0.79)	−0.24 (−0.53 0.11)
$ADC_{m\_0\_500\_5b}$	0.89 (0.70 1.00)	0.75 (0.57 0.90)	−0.55 (−0.75 −0.26)**
$ADC_{m\_0\_2000\_16b}$	0.85 (0.61 1.00)	0.73 (0.54 0.89)	−0.50 (−0.72 −0.20)**
$ADC_{k\_0\_2000\_16b}$	0.87 (0.62 1.00)	0.76 (0.58 0.90)	−0.55 (−0.75 −0.26)**
$K_{\_0\_2000\_16b}$	0.80 (0.60 0.97)	0.60 (0.41 0.79)	0.32 (−0.02 0.59)*
$ADC_{m\_0\_1500\_2b}$	0.85 (0.64 1.00)	0.73 (0.54 0.89)	−0.50 (−0.72 −0.20)**
$ADC_{m\_0\_2000\_2b}$	0.86 (0.63 1.00)	0.76 (0.58 0.90)	−0.54 (−0.74 −0.25)**
K^{trans}	0.63 (0.39 0.86)	0.50 (0.30 0.70)	0.09 (−0.26 0.41)
Cho+Cr/Cit	0.51 (0.27 0.74)	0.69 (0.50 0.86)	0.24 (−0.11 0.53)

*p<0.05; ** p<0.01; *** p<0.001

6. DISCUSSION

6.1. BAY86-7548 PET/CT (study I)

In study I, a ^{68}Ga-labeled bombesin antagonist (BAY86-7548) demonstrated encouraging results for detection of primary prostate with an accuracy of 83%. Moreover, BAY86-7548 had statistically significantly higher SUV in cancerous foci than in BPH. Due to the low expression of GRPr in benign prostatic tissue, BAY86-7548 was shown to be highly cancer specific. In all 11 patients with primary prostate cancer, only one dominant prostate cancer lesion was not identified. Lack of expression of GRPr in this particular lesion could be a reason for the false negative finding. Two other explanations could be hypothesized. First, small and perhaps diffusely growing metastatic deposits can be missed, especially in lesions with a low tumor-specific uptake and low receptor density. Second, ^{68}Ga has an average positron range of 2–3 mm and this physical characteristic makes it less ideal than other radionuclides such as ^{18}F (Kemerink et al. 2011). Although BAY86-7548 PET/CT demonstrated accuracy of 83% for detection of intra-prostatic cancer, a sensitivity of only 67% per patient was found for the detection of lymph node metastases.

This new tracer could be more accurate in the detection of primary prostate cancer than previously used PET tracers. However, the applicability of BAY86-7548 to imaging metastatic disease appears to be less encouraging.

6.2. mpMRI in men with a clinical suspicion of prostate cancer (study II)

Diffusion-weighted imaging demonstrated high accuracy (84%, 88%) and AUC (0.78, 0.81) values for the detection of prostate cancer and clinically significant prostate cancer in men with elevated PSA, normal DRE and no previous biopsy who underwent 3T MRI before their first TRUS-guided biopsy. The use of DWI or DCE-MRI in addition to T2wi significantly ($p<0.001$) improved sensitivity and accuracy values for prostate cancer detection. However, differences between the combination of T2w+DWI and T2wi+DWI+DCE-MRI were rather subtle, implying that T2w+DWI is sufficient for the initial risk estimation of patients with a clinical suspicion of prostate cancer. This is likely to increase clinical application and patient comfort, since the acquisition time can be reduced to under 15 minutes.

6.3. DWI modeling of normal prostate and prostate cancer (study III)

Four different mathematical models for DWI of normal prostate and prostate cancer were evaluated using b values of up to 2000 s/mm^2 in terms of fitting quality and repeatability. A biexponential model provided the highest information content based on ΔAIC, ΔAIC_c and the F-test. However, the parameters of monoexponential, kurtosis and stretched exponential models (except for the α parameter) had higher reliability and repeatability of the fitted parameters compared with the biexponential model. Furthermore, differences between parameters of the biexponential model for normal tissue and prostate did not reach statistical significance. Considering fitting

quality and repeatability of the fitted parameters, the kurtosis model appears to be the preferred model for characterization of normal prostate and prostate cancer using b values up to 2000 s/mm^2, diffusion gradient timing (Δ) 24.5 ms, diffusion gradient duration (δ) 12.6 ms, and the resulting diffusion time of 20.3 ms.

6.4. Continuous wave and RAFF imaging of prostate cancer (study IV)

We demonstrated that T_{RAFF} and $T_{1\rho cw}$ are repeatable and can be applied in routine clinical practice. T_{RAFF}, $T_{1\rho cw}$ and T_2 relaxation times of prostate cancer differed significantly ($p<0.001$) from the corresponding values of normal PZ. Relaxation values obtained using the RAFF method were the only parameter providing power to differentiate tumors with a Gleason score of 3+3 from those with a higher Gleason score. Our findings suggest that RAFF imaging could provide valuable information for prostate cancer detection and characterization.

6.5. DWI and RAFF imaging of prostate cancer (study V)

In this study, we showed that T_{RAFF}, D_f, ADC_{mL}, ADC_{mH}, ADC_k, and K parameter values of prostate cancer were significantly associated with the Gleason score. Similarly to study IV, the RAFF method was highly repeatable and demonstrated the repeatability of ROI analysis comparable with D_f, ADC_{mL}, and ADC_{mH}, parameters. The RAFF method outperformed DWI-derived parameters and T_2 relaxation time values in the Gleason score classification of prostate tumors. Our findings suggest that the RAFF method can provide valuable information for prostate cancer characterization.

6.6. bpMRI in men with a clinical suspicion of prostate cancer (study VI)

The rapid bpMRI prostate imaging protocol applied in study IV was based on the results of study II and demonstrated a high negative predictive value (90–100%) in the detection of prostate cancer and, more importantly, clinically significant prostate cancer. This is an important step forward in the ongoing efforts to improve prostate cancer diagnosis using simpler MRI imaging protocols without needing intravenous contrast, special imaging sequences or endorectal coils. Implementation of these results can improve prostate cancer risk stratification by reducing the number of prostate biopsies while simultaneously increasing the detection of clinically significant prostate cancer.

6.7. ^{18}F-FACBC PET/CT, PET/MRI and mpMRI in the detection and characterization of primary prostate cancer (study VII)

Similar diagnostic accuracy was achieved with ^{18}F-FACBC PET/MRI and mpMRI, both methods outperforming ^{18}F-FACBC PET/CT. ^{18}F-FACBC PET/CT demonstrated especially low specificity values. ^{18}F-FACBC PET and DWI failed to detect lymph node metastases smaller than 7 mm. Although ^{18}F-FACBC PET/CT, SUV_{max} and V_T

values had a statistically significant correlation with the Gleason score of prostate cancer lesions and demonstrated the potential to differentiate tumors with low and high Gleason scores (3+3 vs >3+3, 3+4 and 3+4 vs >3+4), these quantitative parameters (SUV_{max}, V_T) did not outperform DWI and RAFF derived parameters. Dynamic contrast-enhanced MRI (K^{trans}), T_2 mapping and ^{1}H-MRS (Cho+Cr/Cit) had only a limited role in the differentiation of tumors with different Gleason scores, as indicated by low AUC values and non-significant ρ values. It is important to note that DWI and RAFF can be performed without the use of an intravenous contrast agent, are not associated with the radiation dose, take around 4–8 minutes to acquire, and can be acquired with most clinical MR scanners. In the context of these findings, the role of ^{18}F-FACBC PET as a non-invasive surrogate marker of the Gleason score appears to be limited.

6.8. Methodological consideration

When two or more imaging sequences (raters) are applied to detect a cancer, each individual rater classifies a lesion as cancer present or benign. Several methods for calculating diagnostic accuracy for cancer were proposed. However, there is no consensus in the literature. The most commonly applied methods in the prostate MRI literature are: addition of the ratings of each individual imaging sequence in the calculation of AUC (Delongchamps et al. 2011); use of generalized estimation equations with logistic regression modeling (Turkbey et al. 2010); and use of a "decision matrix" where ratings of different imaging sequences are combined to produce only one rating for each individual combination of imaging sequences (Kitajima et al. 2010; Siddiqui et al. 2015). In study II, AUC values were calculated for added ratings (ADC_{added}), and $ADC_{combined}$ were calculated for ratings indicative of prostate cancer when two different imaging sequences were positive for the presence of prostate cancer. In contrast to the use of added ratings and a generalized estimation equation, using a "decision matrix" and the methods applied in studies II and V could easily provide guidance in clinical practice as to whether a patient has a suspicion of prostate cancer.

7. CONCLUSIONS

On the basis of this study the following conclusions were drawn:

1. Histopathological and autoradiography analyses indicate that the ^{68}Ga-labeled bombesin antagonist BAY86-7548 has high prostate binding specificity. BAY86-7548 demonstrated significantly higher uptake in the prostate compared to benign prostatic hyperplasia and normal prostate tissue. It was well tolerated by all patients.

2. The use of anatomical T2-weighted imaging and DWI appears to be accurate and sufficient for initial decision management and targeted biopsy in patients with elevated PSA. Considering the duration and cost of MRI examinations, the additional use of DCE-MRI and ^{1}H-MRS (using current clinical scanners without endorectal coils, ^{1}H-MRS sequences and post-processing) provides limited additional benefit in this patient population.

3. Considering the model fit and repeatability, the kurtosis model seems to be the preferred model for characterization of normal prostate and prostate cancer DWI data obtained using b values of up to 2000 s/mm^2 and a diffusion time of 20 ms. The Kurtosis model for DWI of normal prostate and prostate cancer demonstrated higher information content (fitting quality), similar repeatability, and similar robustness against noise than the most commonly used mono-exponential model.

4. In quantitative ROI-based analysis, relaxation parameters obtained using RAFF outperformed $T_{1\rho cw}$ and T_2 in prostate cancer detection and prediction of the Gleason score.

5. In quantitative ROI-based analysis, relaxation parameters obtained using RAFF outperformed DWI (“low” and “high” b values) and T_2 mapping in prediction of the Gleason score.

6. The newly developed biparametric MRI imaging protocol was shown to improve the selection of men for biopsy, and in combination with targeted biopsy was also significantly more accurate than systematic biopsy alone.

7. ^{18}F-FACBC uptake was significantly higher in tumors with Gleason score >3+4 than in tumors with Gleason score 3+3. However, the ^{18}F-FACBC PET prediction power for the Gleason score was similar or inferior to those of DWI and RAFF derived parameters. Our results indicate that ^{18}F-FACBC PET/CT or PET/MRI brings limited added value to mpMRI (performed using high b values) in the detection and characterization of primary prostate cancer.

8. ACKNOWLEDGEMENTS

This work was carried out at the Medical Imaging Center of Southwest Finland, Turku University Hospital, Department of Radiology, University of Turku and Turku PET center during 2009–2017. The project was financially supported by grants from the following sources: the Instrumentarium Research Foundation, the Sigrid Jusélius Foundation, the Turku University Hospital EVO Funding, the TYKS-VSKK EVO Funding, the TYKS-SAPA Research Fund, the Finnish Cancer Foundation, and the Finnish Cultural Foundation.

I would like to thank my supervisor, Professor Hannu Aronen, Chair of the Department of Radiology, University of Turku, for his support and always believing in me. His broad knowledge of the medical imaging helped to promote this thesis and secured funding for the early phases of this thesis work.

I extend my sincere gratitude to my supervising Professor, Heikki Minn, Chair of the Department of Oncology and Radiotherapy, University of Turku. His vast knowledge of the field of medical oncology and practical approach were invaluable and made this thesis work to progress. His role in establishing the prostate PET studies was essential.

I wish to thank Professor Roberto Blanco, Chair of the Medical Imaging Center of Southwest Finland, for helping me to conduct research at the Center. I also wish to thank Professor Juhani Knuuti, Director of the Turku PET center, for providing me the opportunity to be involved in high quality PET research.

My special thanks to Professor Peter B Dean. His positive attitude and support always brightened my day and gave me further motivation to overcome all the practical hurdles. Professor Dean was a real role model for me of commitment to provide the best patient care.

I am grateful to adjunct professor Pekka Taimen for his willingness to spend long hours reviewing histopathological material used in this thesis. His work was essential and without high quality histopathology analyses this thesis work would not be possible.

I wish to thank to adjunct professor Peter Boström, chair of the Department of Urology, Turku University Hospital, who made a major contribution to patient enrolment and study design. He and his team made it possible to expand my projects from small studies to large registered multi-institutional trials.

Many thanks to physicist Marko Pesola, whose help was essential in the development and validation of novel MRI protocols. Without his expertise in pulse programming, I would still be struggling with some implementations.

I would like to thank Harri Merisaari, a programmer who made a major contribution to this thesis work. I have learned a lot about programming while working with him, and I thank him for helping me with post-processing tasks.

I am grateful to Dr. Kirsti Dean (deceased) for her help in establishing the prostate MRI studies. She was my first teacher in body MR imaging, and such a wonderful person that I was always looking forward to meeting with her.

I also wish to physicist Jani Saunavaara. He is the one with whom, back in 2010, I started to do phantom scans and began learning MRI physics. He always tried to overcome practical hurdles and supported my research.

I am indebted to Anitta Entonen. Her help was instrumental to this thesis project, and without her willingness to contact patients, arrange scanning times, and assist me with MRI scans, this thesis project would never have been completed. She is a very kind person who was always ready to help.

I wish to thank all my excellent co-authors: Dr. Markku Kallajoki for work on reviewing histopathological material used in this thesis; Dr. Kari Syvänen, Dr. Esa Kähkönen and Dr. Otto Ettala for their contribution to patient enrolment and data collection; Dr. Aida Kiviniemi for being so instrumental in setting up new studies; Ileana Montoya Perez for her work on the server used in the IMPROD and FLUCIPRO studies; and Dr. Jukka Kempainen for his help with the PET analyses: he was the one who introduced me to the "PET world" and I am very grateful for your nuts-&-bolts lessons in using a GE workstation.

I thank Dr. Andrew Stephens for assistace with bombesin/RM2 studies and his guidance related to projects involving new PET tracers.

I would like to thank the former or present researchers at the Turku PET center for their support and interest in my studies: Prince Danson, Perti Elo, Han Chunlei, adjunct professor Marko Seppänen whose passion for nuclear medicine was truly inspiring, Dr. Gaber Komar, and Dr. Virva Saunavaara. I wish to thank Tommi Kauko and Jaakko Matomäki for their outstanding work on statistical analyses in the IMPROD trial.

I was fortunate to have the following co-workers at the Turku Center: Dr. Mika Teräs, Dr. Hannu Sipilä, Tuula Tolvanen and Jarmo Teuho. Rami Mikkola and Marko Tättäläinen are greatly acknowledged for their help with IT matters. I wish to thank Timo Laitinen and Sauli Piirola for their great work on Carimas and so much support related to the its use and customization. I would like to thank Jaana Keihäs for being so efficient and helpful with all practical issues of running research projects at the Medical Imaging Center of Southwest Finland.

I wish to thank all patients and healthy volunteers who chose to participate in the studies. Their participation has made this work possible.

I am very grateful for the support and friendship of all my friends in Finland: Mika Uppa, Ville Haarala, Kaarle Kurki, and Tanja Huttunen. Thank you for always being there to remind me that there is something else than just "research". I specially thank Maryann Paul for supporting me in the final stage of this thesis work and ensuring its completion.

Above all, I wish to thank my family, especially my mother, Daniela Jamborová Sr, and my sister, Daniela Jamborová Jr, for giving me so much love, support and always believing in me. I also want to thank them for dealing so well with all the stress related to my work dedication and being absent from home. Needless to say, without them I would not be where I am now. Finally, I wish to thank my father, Ivan Jambor Sr., (deceased). He will always be with me in my heart, and all the sacrifice will never be forgotten.

Ivan Jambor
Turku, Finland August 2017

9. REFERENCES

Ahmed, H.U. et al., 2017. Diagnostic accuracy of multi-parametric MRI and TRUS biopsy in prostate cancer (PROMIS): a paired validating confirmatory study. *Lancet,* 10071(389), pp. 815–822.

Ambrosini, V. et al., 2010. 68Ga-DOTANOC PET/CT clinical impact in patients with neuroendocrine tumors. *J Nucl Med,* 5(51), pp. 669–673.

Andriole, G.L. et al., 2012. Prostate cancer screening in the randomized Prostate, Lung, Colorectal, and Ovarian Cancer Screening Trial: mortality results after 13 years of follow-up. *Journal of the National Cancer Institute.*

Ankerst, D.P. et al., 2014. Evaluating the Prostate Cancer Prevention Trial High Grade Prostate Cancer Risk Calculator in 10 international biopsy cohorts: results from the Prostate Biopsy Collaborative Group. *World J Urol,* 1(32), pp. 185–191.

Aronen, H.J. et al., 1999. 3D spin-lock imaging of human gliomas. *Magn Reson Imaging,* 7(17), pp. 1001–1010.

Arsov, C. et al., 2015. Prospective randomized trial comparing magnetic resonance imaging (MRI)-guided in-bore biopsy to MRI-ultrasound fusion and transrectal ultrasound-guided prostate biopsy in patients with prior negative biopsies. *European Urology,* 4(68), pp. 713–720.

Bammer, R., 2003. Basic principles of diffusion-weighted imaging. *Eur J Radiol,* 3(45), pp. 169–184.

Bennett, K.M. et al., 2003. Characterization of continuously distributed cortical water diffusion rates with a stretched-exponential model. *Magn Reson Med,* 4(50), pp. 727–734.

Bill-Axelson, A. et al., 2008. Radical prostatectomy versus watchful waiting in localized prostate cancer: The Scandinavian prostate cancer group-4 randomized trial. *J Natl Cancer Inst,* 16(100), pp. 1144–1154.

Borthakur, A. et al., 2006. Sodium and T1rho MRI for molecular and diagnostic imaging of articular cartilage. *NMR Biomed,* 7(19), pp. 781–821.

Bourne, R.M. et al., 2012. Biexponential diffusion decay in formalin-fixed prostate tissue: preliminary findings. *Magn Reson Med,* 3(68), pp. 954–959.

Bourne, R.M. et al., 2014. Information theoretic ranking of four models of diffusion attenuation in fresh and fixed prostate tissue ex vivo. *Magn Reson Med,* 5(72), pp. 1418–1426.

Breeuwsma, A.J. et al., 2005. In vivo uptake of [11C]choline does not correlate with cell proliferation in human prostate cancer. *Eur J Nucl Med Mol Imaging,* 6(32), pp. 668–673.

Buzzoni, C. et al., 2015. Metastatic prostate cancer incidence and prostate-specific antigen testing: new insights from the European Randomized Study of Screening for Prostate Cancer. *European Urology,* 5(68), pp. 885–890.

Carroll, P.R. et al., 2015. Prostate Cancer Early Detection, Version 2.2015. *Journal of the National Comprehensive Cancer Network,* 12(13), pp. 1534–1561.

Catalona, W.J. et al., 2012. What the US Preventive Services Task Force missed in its prostate cancer screening recommendation. *Annals of internal medicine,* 2(157), pp. 137–138.

Cescato, R. et al., 2008. Bombesin receptor antagonists may be preferable to agonists for tumor targeting. *J Nucl Med,* 2(49), pp. 318–326.

Chatterjee, A. et al., 2015. Changes in Epithelium, Stroma, and Lumen Space Correlate More Strongly with Gleason Pattern and Are Stronger Predictors of Prostate ADC Changes than Cellularity Metrics. *Radiology,* 3(277), pp. 751–762.

Cheng, L. et al., 2005. Anatomic distribution and pathologic characterization of small-volume prostate cancer (<0.5 ml) in whole-mount prostatectomy specimens. *Mod Pathol,* 8(18), pp. 1022–1026.

Costello, L.C. et al., 2005. Mitochondrial function, zinc, and intermediary metabolism relationships in normal prostate and prostate cancer. *Mitochondrion,* 3(5), pp. 143–153.

D'Amico, A.V. et al., 1998. The combination of preoperative prostate specific antigen and postoperative pathological findings to predict prostate specific antigen outcome in clinically localized prostate cancer. *J Urol,* 6 Pt 1(160), pp. 2096–2101.

D'Amico, A.V. & Roehrborn, C.G., 2007. Effect of 1 mg/day finasteride on concentrations of serum prostate-specific antigen in men with androgenic alopecia: a randomised controlled trial. *The Lancet Oncology,* 1(8), pp. 21–25.

Dal Pra, A. & Souhami, L., 2016. Prostate cancer radiation therapy: A physician's perspective. *Physica Medica*.

Dall'Era, M.A. et al., 2008. Active surveillance for early-stage prostate cancer: review of the current literature. *Cancer,* 8(112), pp. 1650–1659.

De Angelis, R. et al., 2014. Cancer survival in Europe 1999-2007 by country and age: results of EUROCARE-5 population-based study. *The Lancet Oncology,* 1(15), pp. 23–34.

de Jong, I.J. et al., 2002. Visualization of prostate cancer with 11C-choline positron emission tomography. *Eur Urol,* 1(42), pp. 18–23.

Delongchamps, N.B. et al., 2011. Multiparametric magnetic resonance imaging for the detection and localization of prostate cancer: combination of T2-weighted, dynamic contrast-enhanced and diffusion-weighted imaging. *BJU Int,* 9(107), pp. 1411–1418.

Djulbegovic, M. et al., 2010. Screening for prostate cancer: systematic review and meta-analysis of randomised controlled trials. *BMJ,* (341), pp. c4543.

Eichelberger, L.E. & Cheng, L., 2004. Does pT2b prostate carcinoma exist? Critical appraisal of the 2002 TNM classification of prostate carcinoma. *Cancer,* 12(100), pp. 2573–2576.

Epstein, J.I., 2010. An update of the Gleason grading system. *J Urol,* 2(183), pp. 433–440.

Epstein, J.I. et al., 2005. The 2005 International Society of Urological Pathology (ISUP) Consensus Conference on Gleason Grading of Prostatic Carcinoma. *Am J Surg Pathol,* 9(29), pp. 1228–1242.

Fascelli, M. et al., 2015. Combined Biparametric Prostate MRI and Prostate Specific Antigen in the Detection of Prostate Cancer: a A Validation Study in a Biopsy Naïve Patient Population. *Urology*.

Fedorov, A. et al., 2014. A comparison of two methods for estimating DCE-MRI parameters via individual and cohort based AIFs in prostate cancer: a step towards practical implementation. *Magn Reson Imaging,* 4(32), pp. 321–329.

Filson, C.P. et al., 2016. Prostate cancer detection with magnetic resonance-ultrasound fusion biopsy: The role of systematic and targeted biopsies. *Cancer*.

Gilani, I.A. & Sepponen, R., 2016. Quantitative rotating frame relaxometry methods in MRI. *NMR Biomed,* 6(29), pp. 841–861.

Gleason, D.F., 1966. Classification of prostatic carcinomas. *Cancer chemotherapy reports Part 1,* 3(50), pp. 125–128.

Graefen, M. et al., 2001. A validated strategy for side specific prediction of organ confined prostate cancer: a tool to select for nerve sparing radical prostatectomy. *J Urol,* 3(165), pp. 857–863.

Griswold, M.A. et al., 2002. Generalized autocalibrating partially parallel acquisitions (GRAPPA). *Magn Reson Med,* 6(47), pp. 1202–1210.

Hakumaki, J.M. et al., 2002. Early gene therapy-induced apoptotic response in BT4C gliomas by magnetic resonance relaxation contrast T1 in the rotating frame. *Cancer Gene Ther,* 4(9), pp. 338–345.

Hall, M.G. & Barrick, T.R., 2008. From diffusion-weighted MRI to anomalous diffusion imaging. *Magn Reson Med,* 3(59), pp. 447–455.

Hambrock, T. et al., 2010. Magnetic resonance imaging guided prostate biopsy in men with repeat negative biopsies and increased prostate specific antigen. *J Urol,* 2(183), pp. 520–527.

Hamdy, F.C. et al., 2016. 10-Year Outcomes after Monitoring, Surgery, or Radiotherapy for Localized Prostate Cancer. *N Engl J Med,* 15(375), pp. 1415–1424.

Hanley, J.A. & McNeil, B.J., 1983. A method of comparing the areas under receiver operating characteristic curves derived from the same cases. *Radiology,* 3(148), pp. 839–843.

Hattangadi, J.A. et al., 2012. Early detection of high grade prostate cancer using digital rectal examination (DRE) in men with a prostate specific antigen level of< 2.5 ng/mL and the risk of death. *BJU international,* 11(110), pp. 1636–1641.

Heidenreich, A. et al., 2014. EAU guidelines on prostate cancer. part 1: screening, diagnosis, and local treatment with curative intent-update 2013. *Eur Urol,* 1(65), pp. 124–137.

Henkelman, R.M., 1990. Does IVIM measure classical perfusion? *Magn Reson Med,* 3(16), pp. 470–475.

Hricak, H. et al., 1994. Carcinoma of the prostate gland: MR imaging with pelvic phased-array coils versus integrated endorectal--pelvic phased-array coils. *Radiology,* 3(193), pp. 703–709.

Huang, C. & McConathy, J., 2013. Radiolabeled amino acids for oncologic imaging. *Journal of Nuclear Medicine,* 7(54), pp. 1007–1010.

Hughes, C. et al., 2005. Molecular pathology of prostate cancer. *J Clin Pathol,* 7(58), pp. 673-684.

Hugosson, J. et al., 2010. Mortality results from the Gothenburg randomised population-based prostate-cancer screening trial. *The lancet oncology,* 8(11), pp. 725-732.

Jager, G.J. et al., 1997. Dynamic TurboFLASH subtraction technique for contrast-enhanced MR imaging of the prostate: correlation with histopathologic results. *Radiology,* 3(203), pp. 645-652.

Jambor, I. et al., 2010. Functional Imaging of Localized Prostate Cancer Aggressiveness Using 11C-Acetate PET/CT and 1H-MR Spectroscopy1. *J Nucl Med,* 11(51), pp. 1676-1683.

Jambor, I. et al., 2012. Improved detection of localized prostate cancer using co-registered MRI and (11)C-acetate PET/CT. *Eur J Radiol,* 11(81), pp. 2966-2972.

Jambor, I. et al., 2014. Optimization of b-value distribution for biexponential diffusion-weighted MR imaging of normal prostate. *J Magn Reson Imaging,* 5(39), pp. 1213-1222.

Jensen, J.H. et al., 2005. Diffusional kurtosis imaging: the quantification of non-gaussian water diffusion by means of magnetic resonance imaging. *Magn Reson Med,* 6(53), pp. 1432–1440.

Jensen, R.T. et al., 2008. International Union of Pharmacology. LXVIII. Mammalian bombesin receptors: nomenclature, distribution, pharmacology, signaling, and functions in normal and disease states. *Pharmacol Rev,* 1(60), pp. 1–42.

Johansson, J.E. et al., 1997. Fifteen-year survival in prostate cancer. A prospective, population-based study in Sweden. *JAMA,* 6(277), pp. 467–471.

Johnston, D.C. et al., 2005. Dynamics of magnetic defects in heavy fermion LiV2O4 from stretched exponential 7Li NMR relaxation. *Phys Rev Lett,* 17(95), pp. 176408.

Kemerink, G.J. et al., 2011. Effect of the positron range of 18F, 68Ga and 124I on PET/CT in lung-equivalent materials. *Eur J Nucl Med Mol Imaging,* 5(38), pp. 940–948.

Kettunen, M.I. et al., 2007. Low spin-lock field T1 relaxation in the rotating frame as a sensitive MR imaging marker for gene therapy treatment response in rat glioma. *Radiology,* 3(243), pp. 796–803.

Kim, S. et al., 2012. Interstitial fluid pressure correlates with intravoxel incoherent motion imaging metrics in a mouse mammary carcinoma model. *NMR Biomed,* 5(25), pp. 787–794.

Kitajima, K. et al., 2010. Prostate cancer detection with 3 T MRI: comparison of diffusion-weighted imaging and dynamic contrast-enhanced MRI in combination with T2-weighted imaging. *J Magn Reson Imaging,* 3(31), pp. 625–631.

Kranse, R. et al., 2008. A graphical device to represent the outcomes of a logistic regression analysis. *The Prostate,* 15(68), pp. 1674–1680.

Kumar, R. et al., 2011. Role of (68)Ga-DOTATOC PET-CT in the diagnosis and staging of pancreatic neuroendocrine tumours. *Eur Radiol,* 11(21), pp. 2408–2416.

Kuru, T.H. et al., 2013. Critical evaluation of magnetic resonance imaging targeted, transrectal ultrasound guided transperineal fusion biopsy for detection of prostate cancer. *The Journal of urology,* 4(190), pp. 1380–1386.

Larsson, H.B. et al., 1996. Myocardial perfusion modeling using MRI. *Magn Reson Med,* 5(35), pp. 716–726.

Le Bihan, D. et al., 1988. Separation of diffusion and perfusion in intravoxel incoherent motion MR imaging. *Radiology,* 2(168), pp. 497–505.

Le Bihan, D. & Turner, R., 1992. The capillary network: a link between IVIM and classical perfusion. *Magn Reson Med,* 1(27), pp. 171–178.

Liimatainen, T. et al., 2014. MRI contrasts in high rank rotating frames. *Magn Reson Med*.

Liimatainen, T. et al., 2012. Glioma cell density in a rat gene therapy model gauged by water relaxation rate along a fictitious magnetic field. *Magn Reson Med,* 1(67), pp. 269–277.

Liimatainen, T. et al., 2010. MRI contrast from relaxation along a fictitious field (RAFF). *Magn Reson Med,* 4(64), pp. 983–994.

Liu, I.J. et al., 2001. Fluorodeoxyglucose positron emission tomography studies in diagnosis and staging of clinically organ-confined prostate cancer. *Urology,* 1(57), pp. 108–111.

Logan, J., 2000. Graphical analysis of PET data applied to reversible and irreversible tracers. *Nuclear medicine and biology,* 7(27), pp. 661–670.

Luciani, A. et al., 2008. Liver cirrhosis: intravoxel incoherent motion MR imaging--pilot study. *Radiology,* 3(249), pp. 891–899.

Lundon, D.J. et al., 2015. Prostate cancer risk assessment tools in an unscreened population. *World journal of urology,* 6(33), pp. 827–832.

Mena, E. et al., 2012. ^{11}C-Acetate PET/CT in Localized Prostate Cancer: A Study with MRI and Histopathologic Correlation. *J Nucl Med*.

Merisaari, H. et al., 2016. Fitting methods for intravoxel incoherent motion imaging of prostate cancer on region of interest level: Repeatability and gleason score prediction. *Magn Reson Med*.

Michaeli, S. et al., 2007. Assessment of brain iron and neuronal integrity in patients with Parkinson's disease using novel MRI contrasts. *Mov Disord,* 3(22), pp. 334–340.

Mohler, J.L. et al., 2016. Prostate Cancer, Version 1.2016. *Journal of the National Comprehensive Cancer Network,* 1(14), pp. 19–30.

Moyer, V.A., 2012. Screening for prostate cancer: U.S. Preventive Services Task Force recommendation statement. *Ann Intern Med,* 2(157), pp. 120–134.

Mulkern, R.V. et al., 2005. Magnetization transfer studies of the fast and slow tissue water diffusion components in the human brain. *NMR Biomed,* 3(18), pp. 186–194.

Mullerad, M. et al., 2005. Comparison of endorectal magnetic resonance imaging, guided prostate biopsy and digital rectal examination in the preoperative anatomical localization of prostate cancer. *J Urol,* 6(174), pp. 2158–2163.

Oyama, N. et al., 2002. 11C-acetate PET imaging of prostate cancer. *J Nucl Med,* 2(43), pp. 181–186.

Parekh, D.J. et al., 2015. A multi-institutional prospective trial in the USA confirms that the 4Kscore accurately identifies men with high-grade prostate cancer. *European Urology,* 3(68), pp. 464–470.

Parker, G.J. et al., 2006. Experimentally-derived functional form for a population-averaged high-temporal-resolution arterial input function for dynamic contrast-enhanced MRI. *Magn Reson Med,* 5(56), pp. 993–1000.

Partin, A.W. et al., 1998. Prospective evaluation of percent free-PSA and complexed-PSA for early detection of prostate cancer. *Prostate Cancer & Prostatic Diseases,* 4(1), pp.

Partin, A.W. et al., 2001. Contemporary update of prostate cancer staging nomograms (Partin Tables) for the new millennium. *Urology,* 6(58), pp. 843–848.

Ploussard, G. et al., 2015. Can we expand active surveillance criteria to include biopsy Gleason 3+4 prostate cancer? A multi-institutional study of 2,323 patients. *Urol Oncol,* 2(33), pp. 71–79.

Pokorny, M.R. et al., 2014. Prospective study of diagnostic accuracy comparing prostate cancer detection by transrectal ultrasoundGÇôguided biopsy versus magnetic resonance (MR) imaging with subsequent MR-guided biopsy in men without previous prostate biopsies. *European Urology,* 1(66), pp. 22–29.

Presti, J.C., Jr. et al., 1996. Local staging of prostatic carcinoma: comparison of transrectal sonography and endorectal MR imaging. *AJR Am J Roentgenol,* 1(166), pp. 103–108.

Pruessmann, K.P. et al., 1999. SENSE: sensitivity encoding for fast MRI. *Magn Reson Med,* 5(42), pp. 952–962.

Puech, P. et al., 2013. Prostate Cancer Diagnosis: Multiparametric MR-targeted Biopsy with Cognitive and Transrectal US-MR Fusion Guidance versus Systematic Biopsy--Prospective Multicenter Study. *Radiology,* 2(268), pp. 461–469.

Puech, P. et al., 2009. Dynamic contrast-enhanced magnetic resonance imaging evaluation of intraprostatic prostate cancer: correlation with radical prostatectomy specimens. *Urology,* 5(74), pp. 1094–1099.

Radtke, J.P. et al., 2015. Improved detection of anterior fibromuscular stroma and transition zone prostate cancer using biparametric and multiparametric MRI with MRI-targeted biopsy and MRI-US fusion guidance. *Prostate cancer and prostatic diseases*.

Radwan, M.H. et al., 2007. Prostate-specific antigen density predicts adverse pathology and increased risk of biochemical failure. *Urology,* 6(69), pp. 1121–1127.

Rais-Bahrami, S. et al., 2015. Diagnostic value of biparametric magnetic resonance imaging (MRI) as an adjunct to prostate specific antigen (PSA) based detection of prostate cancer in men without prior biopsies. *BJU international,* 3(115), pp. 381–388.

Ramadan, U.A. et al., 1998. On- and off-resonance spin-lock MR imaging of normal human brain at 0.1 T: possibilities to modify image contrast. *Magn Reson Imaging,* 10(16), pp. 1191–1199.

Ramirez de, M.A. et al., 2002. Overexpression of choline kinase is a frequent feature in human tumor-derived cell lines and in lung, prostate, and colorectal human cancers. *Biochem Biophys Res Commun,* 3(296), pp. 580–583.

Reubi, J.C. et al., 2002. Bombesin receptor subtypes in human cancers: detection with the universal radioligand (125)I-[D-TYR(6), beta-ALA(11), PHE(13), NLE(14)] bombesin(6-14). *Clin Cancer Res,* 4(8), pp. 1139–1146.

Rofsky, N.M. et al., 1999. Abdominal MR imaging with a volumetric interpolated breath-hold examination. *Radiology,* 3(212), pp. 876–884.

Rosenkrantz, A.B. et al., 2015. Dynamic contrast-enhanced MRI of the prostate with high spatiotemporal resolution using compressed sensing, parallel imaging, and continuous golden-angle radial sampling: preliminary experience. *J Magn Reson Imaging,* 5(41), pp. 1365–1373.

Rosenkrantz, A.B. & Taneja, S.S., 2015. Prostate MRI Can Reduce Overdiagnosis and Overtreatment of Prostate Cancer. *Academic radiology,* 8(22), pp. 1000–1006.

Rutter, C.M., 2000. Bootstrap estimation of diagnostic accuracy with patient-clustered data. *Acad Radiol,* 6(7), pp. 413–419.

Salminen, E. et al., 2002. Investigations with FDG-PET scanning in prostate cancer show limited value for clinical practice. *Acta Oncol,* 5(41), pp. 425–429.

Scheenen, T.W. et al., 2005. Optimal timing for in vivo 1H-MR spectroscopic imaging of the human prostate at 3T. *Magn Reson Med,* 6(53), pp. 1268–1274.

Scheenen, T.W. et al., 2007. Three-dimensional proton MR spectroscopy of human prostate at 3 T without endorectal coil: feasibility. *Radiology,* 2(245), pp. 507–516.

Scheenen, T.W. et al., 2004. Fast acquisition-weighted three-dimensional proton MR spectroscopic imaging of the human prostate. *Magn Reson Med,* 1(52), pp. 80–88.

Schimmöller, L. et al., 2014. Predictive power of the ESUR scoring system for prostate cancer diagnosis verified with targeted MR-guided in-bore biopsy. *European journal of radiology,* 12(83), pp. 2103–2108.

Schröder, F. et al., 2012. Prostate-cancer mortality at 11 years of follow-up. *New England Journal of Medicine,* 11(366), pp. 981–990.

Schulz, V. et al., 2011. Automatic, three-segment, MR-based attenuation correction for whole-body PET/MR data. *European journal of nuclear medicine and molecular imaging,* 1(38), pp. 138–152.

Schuster, D.M. et al., 2013. Characterization of primary prostate carcinoma by anti-1-amino-2-[(18)F] -fluorocyclobutane-1-carboxylic acid (anti-3-[(18)F] FACBC) uptake. *Am J Nucl Med Mol Imaging,* 1(3), pp. 85–96.

Schuster, D.M. et al., 2007. Initial experience with the radiotracer anti-1-amino-3-18F-fluorocyclobutane-1-carboxylic acid with PET/CT in prostate carcinoma. *J Nucl Med,* 1(48), pp. 56–63.

Seppala, J. et al., 2009. Carbon-11 acetate PET/CT based dose escalated IMRT in prostate cancer1. *Radiother Oncol,* 2(93), pp. 234–240.

Shah, R.B. & Zhou, M., 2016. Recent advances in prostate cancer pathology: Gleason grading and beyond. *Pathology International*.

Shrout, P.E. & Fleiss, J.L., 1979. Intraclass correlations: uses in assessing rater reliability. *Psychol Bull,* 2(86), pp. 420–428.

Shukla-Dave, A. et al., 2007. Detection of prostate cancer with MR spectroscopic imaging: an expanded paradigm incorporating polyamines. *Radiology,* 2(245), pp. 499–506.

Siddiqui, M.M. et al., 2015. Comparison of MR/ultrasound fusion-guided biopsy with ultrasound-guided biopsy for the diagnosis of prostate cancer. *JAMA,* 4(313), pp. 390–397.

Siegel, R.L. et al., 2016. Cancer statistics, 2016. *CA Cancer J Clin,* 1(66), pp. 7–30.

Sonn, G.A. et al., 2014. Value of targeted prostate biopsy using magnetic resonance-ultrasound fusion in men with prior negative biopsy and elevated prostate-specific antigen. *European Urology,* 4(65), pp. 809–815.

St Lawrence, K.S. & Lee, T.Y., 1998. An adiabatic approximation to the tissue homogeneity model for water exchange in the brain: I. Theoretical derivation. *J Cereb Blood Flow Metab,* 12(18), pp. 1365–1377.

Star-Lack, J. et al., 1997. Improved water and lipid suppression for 3D PRESS CSI using RF band selective inversion with gradient dephasing (BASING). *Magn Reson Med,* 2(38), pp. 311–321.

Swanson, G.P. et al., 2006. Current status of lymph node-positive prostate cancer: Incidence and predictors of outcome. *Cancer,* 3(107), pp. 439–450.

Taneja, S.S., 2006. Prostate biopsy: targeting cancer for detection and therapy. *Rev Urol,* 4(8), pp. 173–182.

Thompson, I.M. et al., 2004. Prevalence of prostate cancer among men with a prostate-specific antigen level < or =4.0 ng per milliliter. *N Engl J Med,* 22(350), pp. 2239–2246.

Thompson, I.M. et al., 2006. Assessing prostate cancer risk: results from the Prostate Cancer Prevention Trial. *Journal of the National Cancer Institute,* 8(98), pp. 529–534.

Thompson, I.M. et al., 2005. Operating characteristics of prostate-specific antigen in men with an initial PSA level of 3.0 ng/ml or lower. *JAMA,* 1(294), pp. 66–70.

Tofts, P.S., 1997. Modeling tracer kinetics in dynamic Gd-DTPA MR imaging. *J Magn Reson Imaging,* 1(7), pp. 91–101.

Tofts, P.S. et al., 1999. Estimating kinetic parameters from dynamic contrast-enhanced T(1)-weighted MRI of a diffusable tracer: standardized quantities and symbols. *J Magn Reson Imaging,* 3(10), pp. 223–232.

Tofts, P.S. & Kermode, A.G., 1991. Measurement of the blood-brain barrier permeability and leakage space using dynamic MR imaging. 1. Fundamental concepts. *Magn Reson Med,* 2(17), pp. 357–367.

Toivonen, J. et al., 2015. Mathematical models for diffusion-weighted imaging of prostate cancer using b values up to 2000 s/mm(2): Correlation with Gleason score and repeatability of region of interest analysis. *Magn Reson Med,* 4(74), pp. 1116–1124.

Toth, G. et al., 2005. Detection of prostate cancer with 11C-methionine positron emission tomography. *J Urol,* 1(173), pp. 66–69.

Trajman, A. & Luiz, R.R., 2008. McNemar chi2 test revisited: comparing sensitivity and specificity of diagnostic examinations. *Scand J Clin Lab Invest,* 1(68), pp. 77–80.

Trottier, G. et al., 2011. Comparison of risk calculators from the Prostate Cancer Prevention Trial and the European Randomized Study of Screening for Prostate Cancer in a contemporary Canadian cohort. *BJU international,* 8b(108), pp. E237–E244.

Turkbey, B. et al., 2010. Prostate cancer: value of multiparametric MR imaging at 3 T for detection--histopathologic correlation. *Radiology,* 1(255), pp. 89–99.

Turkbey, B. et al., 2013. Localized prostate cancer detection with 18F FACBC PET/CT: comparison with MR imaging and histopathologic analysis. *Radiology,* 3(270), pp. 849–856.

Umbehr, M.H. et al., 2013. The role of 11C-choline and 18F-fluorocholine positron emission tomography (PET) and PET/CT in prostate cancer: a systematic review and meta-analysis. *Eur Urol,* 1(64), pp. 106–117.

Wang, H.Z. et al., 1987. Optimizing the precision in T1 relaxation estimation using limited flip angles. *Magn Reson Med,* 5(5), pp. 399–416.

Wilson, A.H., 2014. The Prostate Gland: A Review of its Anatomy, Pathology, and Treatment. *JAMA,* 5(312), p. 562.

Yankeelov, T.E. et al., 2005. Quantitative pharmacokinetic analysis of DCE-MRI data without an arterial input function: a reference region model. *Magn Reson Imaging,* 4(23), pp. 519–529.